IDEA League

Master of Science in Applied Geophysics

Research Thesis

Redatuming and Quantifying Attenuation from Reflection Data Using the Marchenko Equation

A Novel Approach to Quantify Q-factor and Seismic Upscaling

Yury Alkhimenkov

August 20, 2017

Redatuming and Quantifying Attenuation from Reflection Data Using the Marchenko Equation

A Novel Approach to Quantify Q-factor and Seismic Upscaling

Master of Science Thesis

for the degree of Master of Science in Applied Geophysics

by

Yury Alkhimenkov

August 20, 2017

Delft University of Technology

Delft University of Technology

Printed in The Netherlands

IDEA LEAGUE
JOINT MASTER'S IN APPLIED GEOPHYSICS

Delft University of Technology, The Netherlands
ETH Zürich, Switzerland
RWTH Aachen, Germany

Dated: *August 20, 2017*

Supervisor(s):

Prof. Dr. Ir. C.P.A. Wapenaar

J. Brackenhoff

Committee Members:

Prof. Dr. Ir. C.P.A. Wapenaar

J. Brackenhoff

Prof. Dr. F. Wellmann

The question therefore naturally arises as to whether it is possible to reconstruct the potential from a knowledge of the asymptotic form of the wave functions at infinity, and if this is possible, to give a method for carrying out the construction. Such is the inverse problem of scattering theory. Of even more interest than the actual construction of the potential are the various relationships that can be established between it and the asymptotic form of the wave functions.

...The mathematical techniques developed in the solution of the problem may also be applied to related questions.

Preface from

Agranovich, Z. S., Marchenko, V. A. (1964)

The Inverse Problem of Scattering Theory

Abstract

Marchenko Imaging is a new technology in geophysics which enables to retrieve Green's functions at any point in the subsurface having only reflection data. This method is based on the extension of the 1D Gelfand-Levitan-Marchenko equation to a 3D medium. One of the assumptions of the Marchenko method is that the medium is lossless. If the lossy reflection response is used in the Marchenko scheme, some artefacts in the Green's functions as well as in the seismic image are present. One way to circumvent this assumption is to find a compensation parameter for the lossy reflection series so that the lossless Marchenko scheme can be applied. The main tasks of this thesis are to: [1] use the Marchenko equation to estimate the attenuation in the subsurface, [2] find a compensation parameter for the lossy reflection series so that the lossless Marchenko scheme can be applied, and [3] to create an upscaling method for wave propagation. The Artefact Removal Method was created which makes it possible to calculate an effective temporal Q-factor of the medium between a virtual source in the subsurface and receivers at the surface. This method is based on the minimization of the artefacts produced by the lossless Marchenko scheme. The minimization was performed in three ways: [1] in the space-time domain, [2] in the frequency domain and [3] to the scales of the wavelet transform applied to the artefacts. This method can also be used to find the layers with high attenuation. The upscaling method which can be used to construct macro-scale homogenized viscoelastic properties of the medium from the micro-scale properties of a heterogeneous medium was developed. This is done through linking the macro- and micro-scale Lippmann-Schwinger equations which describe the wave field and the strain field scattering in an inhomogeneous medium, respectively. In this thesis, the macro-scale homogenized viscoelastic properties were calculated by using the T-matrix Approach and the Generalized Dvorkin-Mavko Attenuation Model. All theoretical results are supported by synthetic 1D modeling. The theoretical part of the thesis and the general work flow can be used for a very complex medium.

Acknowledgements

First of all, I would like to thank my supervisors Dr. Kees Wapenaar and Joeri Brackenhoff without whom this project wouldn't exist. You were very helpful during this project and always inspired me to produce new results and gave me a lot of freedom and latitude during this project, along with infinitely constructive comments. Because of that, I implemented some ideas which I didn't expect to accomplish during this work. It would be remiss not to mention Dr. Evert Slob, who shared his ideas regarding the implementation of the Marchenko scheme for lossy medium, and gave me the confidence to create new results in geophysics. I want to thank Lele Zhang for useful discussions regarding the Marchenko scheme. I would like to thank Dr. Morten Jakobsen for fruitful discussions regarding the Dvorkin-Mavko Attenuation Model. I am also grateful to my first supervisor, Dr. Irina Bayuk, for constructive criticism regarding my rock physics modeling part. Additional thanks to Deyan Draganov, Jack Dvorkin, Serge Shapiro, Kirill Epov and Gennady Goloshubin, for their prompt replies to my emails and providing necessary literature to help me in this endeavor. Last but not least, special thanks to Susan Fritz and SchoolOf2.us for providing me online Skype English lessons for the past two and a half years.

Delft University of Technology
August 20, 2017

Yury Alkhimenkov

Table of Contents

List of Figures

List of Tables

Acronyms

DUT Delft University of Technology

ETH Swiss Federal Institute of Technology

RWTH Aachen University

August 20, 2017

Chapter 1

Introduction

Seismic imaging is a key method for studying the subsurface structures of the earth. At the same time, seismic imaging is one of the most challenging tasks in geophysics. This method has a long history and many applications, but its main function is to create an image of the subsurface by using only the reflection data measured at the surface. There are many imaging methods but this thesis is focused on Marchenko imaging. Wave propagation is governed by the hyperbolic partial differential equation. It is well known that the 1D inverse problem in quantum mechanics can be solved by the Gelfand-Levitan-Marchenko equation. Therefore, it might be possible to extend this equation to a 3D case and apply the method to wave propagation. The key idea is to use Green's functions — the medium's response due to the impulsive point source. Once we know the Green's functions inside the medium, the image can be constructed. According to Green's Theorem, we can correctly retrieve the Green's functions of the medium if the data is available from all sides of the medium. Seismic interferometry (Wapenaar and Fokkema, 2006) is an example of this idea. However, under several assumptions, it is possible to retrieve the Green's function by using only the reflection data. The 3D extension of the Marchenko equation for one-way wave fields as well as practical applications of this method are given in Wapenaar et al. (2014b). By applying this method to the reflection data, the Marchenko imaging can be performed and Marchenko redatuming can be done at any depth level. For redatuming, only an estimate of the first-arrival travel-time from the virtual receiver to the acquisition surface is needed (Wapenaar et al., 2014b; van der Neut et al., 2015). This can be achieved, for example, from a smooth velocity model of the subsurface. For imaging a smooth velocity model is required. One of the assumptions of the Marchenko method is that the medium is lossless. This assumption is one of the problems preventing the practical applications of this method to real data; So circumventing this assumption is a worthwhile endeavor and paramount to this body of work. If the lossy reflection response is used in Marchenko imaging, some artefacts in the Green's functions as well as in the seismic image are present.

The main tasks of this thesis are to: [1] use the Marchenko equation to estimate the attenuation in the subsurface, [2] find a compensation parameter for the lossy reflection series so

that the lossless Marchenko scheme can be applied, and [3] to create an upscaling method for wave propagation.

The Artefact Removal Method was created, which makes it possible to calculate an effective temporal Q-factor of the subsurface. This was achieved through minimization of the artefacts, which were produced by the lossless Marchenko scheme. The estimated attenuation of the medium can further be used to compensate for the attenuation in the lossy reflection series. This can then be applied back to the lossless Marchenko scheme.

In order to address scale effects, an upscaling approach was created. Wave propagation at micro- scale (scale of a rock sample) and macro-scale (scale of several dozens of meters) are governed by the same partial differential equation. The upscaling method is a forward problem, but the downscaling method is an inverse problem — one of the key issues in geophysics. One way to bridge the gap between micro-scale and macro-scale is to use some properties of the medium. It can be approximated as a viscoelastic solid. In this thesis, seismic imaging was linked to rock physics, using the viscoelasticity of the rocks (see Figure 1-1). As a forward problem, the macroscopic properties of the medium were calculated by using the micro-scale properties of a heterogeneous medium. Theoretically, the general idea of up-down- scaling is shown through linking the macro- and micro- scale Lippmann-Schwinger equations which describe the wave field and the strain field scattering in an inhomogeneous medium, respectively. By using the T-matrix method and the Generalized Dvorkin-Mavko Attenuation Model, the homogenized viscoelastic properties of the medium can be obtained. Thus, all the changes in the rock's microstructure can be observed in seismic imaging. For example, a reservoir filled with fluid has a very strong attenuation, which can be observed in seismic imaging (seen as very low amplitudes of the reflections). This upscaling approach is supported by a synthetic simulation in 1D.

1-1 Thesis Overview

In chapter 2, the general theory of Sturm-Liouville Operators, Green's Functions and Fundamental Solutions is briefly outlined. In chapter 3, the theory behind Marchenko Imaging is shown as well as the practical applications of the method to seismic imaging. In chapter 4, the general theory of viscoelasticity and seismic attenuation is given. In chapter 5, the theory of wave propagation in heterogeneous pocks and rock physics modeling is shown. In chapters 6 and 7, different theoretical and practical results are shown. They include: the Artefact Removal Method to quantify attenuation in the subsurface, Marchenko redatuming for lossy medium, the connection between the different types of Lippmann-Schwinger equations and rock physics modeling, which provides the upscaling of seismic properties. The general conclusion to the whole thesis is given in chapter 8.

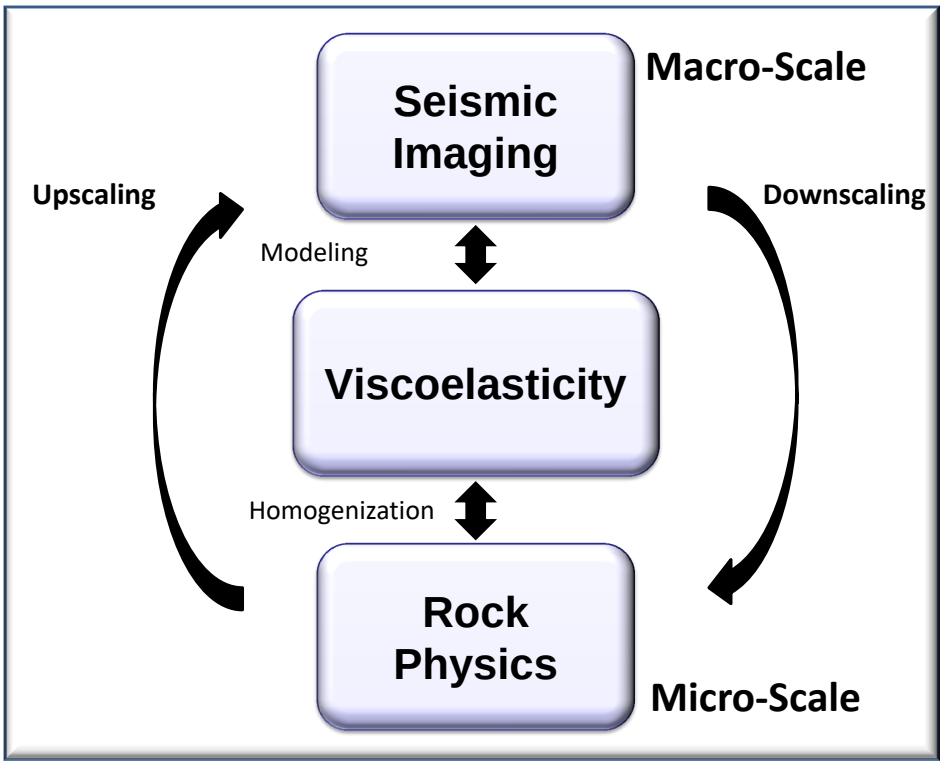

Figure 1-1: The schematic overview of the thesis. Seismic imaging and rock physics are linked through viscoelasticity of the medium. Black arrows represent the connections between different scales. The upscaling problem comes from: [1] a rock sample scale up to an averaged viscoelastic property scale, through homogenization, and [2] from an averaged viscoelastic property scale up to a seismic imaging scale, through modeling. The downscaling problem is an inverse problem.

Chapter 2

Sturm-Liouville Operators, Green's Functions and Fundamental Solutions

Sturm-Liouville Operators, Green's Functions and Fundamental Solutions are heavily referenced throughout the rest of this thesis. They are briefly outlined below. This allowed me to remove all complicated math theory, as is customary for geophysical papers. In this chapter all equations are written in operator form.

Consider this partial differential equation where L is a differential operator and $x \in \Omega$, $\Omega \subset \mathbb{R}^n$:

$$Lu(x) = f(x) \tag{2-1}$$

Operator L can have any form. It might be a Sturm-Liouville operator $L = (\mathrm{d}^2/\mathrm{d}x^2) + q(x)$, where $q(x)$ is the potential (chapter 2-2), or D'Alembert operator for a 3D wave equation (or more sophisticated form in case of an inhomogeneous wave equation), or an operator $L = \nabla_j C_{ijkl} \nabla_l$ for the equilibrium equation, where C_{ijkl} is the stiffness tensor (chapter 5), etc.

The Green's function G is defined as a solution of the following equation:

$$LG(x, \xi) = \delta(\xi - x). \tag{2-2}$$

The solution $G(x, \xi)$ of Eq. (2-2) is called the Green's function of L (Egorov and Shubin, 1988). The Green's function can be defined as $G(x, t)$ for (x, t) in $\mathbb{R}^4$. The definition (2-2) will be used in this chapter but it can be extended to include the time variable:

$$Lu(x, t) = f(x, t) \tag{2-3}$$

and

$$LG(x,t;\xi,t') = \delta(\xi - x)\delta(t - t') \tag{2-4}$$

The term *fundamental solution* is a generalization of Green's function theory. More precisely, the fundamental solution of the operator L is not unique. It can be defined as a set of solutions with constant coefficients that have corresponding boundary conditions (Vladimirov et al., 1971). This fundamental solution will be applied in chapter 3-2. The solution of Eq. (2-1) can be written as:

$$u(x) = G * f = \int G(x,\xi)f(\xi)\mathrm{d}\xi, \tag{2-5}$$

where $*$ denotes a convolution operator. At the same time, I can define an inverse operator L^{-1} as an integral operator:

$$L^{-1}f(x) = \int G(x,\xi)f(\xi)\mathrm{d}\xi \tag{2-6}$$

Indeed, it can be easily shown, that:

$$\int LG(x,\xi)f(\xi)\mathrm{d}\xi = \int \delta(x - \xi)f(\xi)\mathrm{d}x = f(x) \tag{2-7}$$

Here, I used a fundamental property of the Dirac's δ function which is defined as:

$$\langle \delta(x - \xi), \varphi(x) \rangle = \varphi(\xi), \tag{2-8}$$

where $\varphi(x)$ is a test function. For simplicity, Eq. (2-8) is usually written as:

$$\int \delta(x - \xi)\varphi(x)\mathrm{d}\xi = \varphi(\xi), \tag{2-9}$$

Therefore, the solution of the partial differential equation Eq. (2-1) is:

$$Lu(x) = \int LG(x,\xi)f(\xi)\mathrm{d}\xi \tag{2-10}$$

Eq. (2-10) proves the solution given in Eq. (2-5). On the other hand, the classical Sturm-Liouville theory is based on the eigenvalues and corresponding eigenvectors which form an orthonormal basis. From that point of view, the Green's function is a special combination of the eigenvalues and eigenvectors which form the solution of the partial differential equation. For example, in case of a hyperbolic equation (for example, wave equation), all eigenvalues

are real and the Green's function has a very nice representation in terms of eigenvalues and eigenvectors. By saying that, I mean that we can consider an operator G in $L^2(\Omega)$ with its kernel $G(x,\xi)$:

$$Gf(x) = \int_{\Omega} G(x,\xi) f(\xi) \mathrm{d}\xi \tag{2-11}$$

In Eq. (2-11) operator G is symmetric and Ω is the domain. According to the Hilbert-Schmidt theorem (similar to the Spectral theorem) operator G has a complete orthogonal system of eigenfunctions with corresponding real eigenvalues (Reed and Simon, 1980). This property is widely used in seismic wave propagation, usually for self-adjoint operators; For example: in Wapenaar and Douma (2012) as a Hermitian matrix. Note that, in the mathematical literature, all problem formulations and corresponding solutions of partial differential equations are considered in particular functional spaces. In mathematical physics such spaces are Sobolev spaces $\mathcal{W}^{(k)}(\Omega)$, Hilbert spaces or $L^{(k)}(\Omega)$ spaces, etc. In particular, the most popular functional space in geophysics is the $L^2(\Omega)$ space. This is mainly because of L^2-norm which naturally arises in the ill-posed problems. $L^2(\Omega)$ is a classical example of a Hilbert space. At the same time the $L^2(\Omega)$ Hilbert space is, in fact, a Sobolev space $\mathcal{W}^0(\Omega)$, i.e. $L^2(\Omega) = \mathcal{W}^0(\Omega)$. The space is important because the solution of the partial differential equation might not exist in one space, but it does exist in another space.

In geophysics we use the theories developed in different areas of math and physics, i.e. numerical analysis, functional analysis, quantum mechanics, quantum scattering theory and others. They all have their own conventions, notation etc. In geophysics we focus on applying these theories to solve geophysical problems. Therefore, I simplified math where it was possible but also provided necessary references where you can get the original theories and equations.

Chapter 3

Marchenko Imaging

Marchenko Imaging has many practical applications when it comes to seismic imaging. The Marchenko equation was developed to solve the inverse quantum scattering problems (Marchenko, 1955). My work is focused on applying the Marchenko equation to wave propagation problems. The original Marchenko Imaging theory was developed for lossless media (Wapenaar et al., 2014b); But this work is focused on studying lossy media — [A] quantifying attenuation from reflection data, [B] Marchenko Redatuming in viscoelastic media with intrinsic attenuation and, [C] possibly, Marchenko Imaging in viscoelastic media. This is a new approach to quantifying attenuation using the Marchenko equation. Some of these problems can be solved using the existing method. In this case, the solution is shown. Where it is not possible to reach the goal, it is shown why. It is a new technology, therefore, it is essential to show how attenuation affects Marchenko Imaging and how the Marchenko equation can be used for quantifying attenuation using only single-sided data. That's why the starting point in this work is the basic laws of solid mechanics and wave propagation. Only such an analysis can provide a complete overview of the problem and yield a solution.

In this chapter, the theory behind Marchenko Imaging will be shown as well as the practical applications of the method to seismic imaging. It includes: [1] an overview of the development of the Marchenko Equation, [2] the theory behind Marchenko Imaging (1D Gelfand-Levitan and 1D Marchenko Integral equations (Burridge, 1980)), [3] the idea behind the single-sided autofocusing and a brief review of the different scattering equations (Broggini and Snieder, 2012), and [4] Marchenko Equations for Wave Propagation (Wapenaar et al., 2014a,b; van der Neut et al., 2015).

3-1 An Overview of the Development of the Marchenko Equation

Inverse scattering problems are of high importance in geophysics. First of all, these problems arise in quantum mechanics. The inverse problem in quantum mechanics consists of reconstructing the potential function of the Schrödinger operator by its spectrum and some (so-called) norming constants. This problem is also known as the inverse Sturm-Liouville problem.

It was first formulated by Ambarzumian (1929) in 1929. Nowadays, the one-dimensional inverse scattering problem can be solved by the Gelfand-Levitan-Marchenko equation (Gelfand and Levitan, 1951; Marchenko, 1955; Agranovich and Marchenko, 1964). The theorems which prove the uniqueness of the determination of the quantum scattering potential $V(x)$ on the half-line for Schrödinger operators were originally developed by Marchenko (1952, 1955) and Borg (1952) in the 1950s. The reconstruction procedures for the potential were shown by Gelfand and Levitan (1951), Levitan (1987), Levitan and Sargsian (1975) and Marchenko (1955, 2011). A survey and a short history of the problem you can find in Faddeyev and Seckler (1963). Other authors that contributed include: Norman Levinson, Mark Krein and Ludvig Faddeev.

Later, it was shown that the methods developed in quantum mechanics could be applied to solve the inverse problems of wave propagation. Burridge (1980) showed that the steady-state Schrödinger equation is related to the wave equation via a temporal Fourier transformation. It means that the theory developed by Gelfand and Levitan (1951) and Agranovich and Marchenko (1964) can be used to solve the inverse scattering problem for the wave equation. Furthermore, Burridge (1980) showed that this theory has a very nice formulation in the time-space domain. The next important contribution was done by Rose (Rose, 2001, 2002). Rose showed the possibility to focus the wave field in the 1D medium using the Marchenko equation if only the single-sided data are given.

Nowadays, this theory can be applied to imaging, particular, to seismic imaging methods. Broggini and Snieder (2012) showed the connection between different scattering principles — inverse scattering, Green's function reconstruction, Optical theorem and imaging. The paper by Wapenaar et al. (2014b) generalizes the theory and provides the 3D extension of the Marchenko equations as well as the iterative scheme to its solution.

3-2 The 1D Gelfand-Levitan and the 1D Marchenko Integral Equations

3-2-1 The solution of the Inverse Problem

The one-dimensional wave equation can be written in the following notation:

$$\left[\left(K+\frac{4}{3}\mu\right)u_z\right]_z-\rho u_{tt}=0 \tag{3-1}$$

or

$$\left(\rho v^2 u_z\right)_z-\rho u_{tt}=0. \tag{3-2}$$

Here, t is time and z is the space coordinate; u is the elastic displacement; $K=K(z)$ is the bulk modulus; $\mu=\mu(z)$ is the shear modulus. The function $\rho=\rho(z)$ is the density and $v=v(z)$ is the velocity of the wave. Equation Eq. (3-2) can be rewritten in the following form (Burridge, 1980) via simple change of variables:

$$U_{tt} - U_{xx} + q(x)U = 0. \tag{3-3}$$

$$q(x) = \frac{\eta_{xx}}{\eta}, \tag{3-4}$$

where $\eta = [v(z)\rho(z)]^{1/2}$ and $U = \eta^{-1}u$. Obviously, η^2 is the impedance. (Nota Bene: In Eq. (3-3), ∂^2_{xx} is written instead of ∂^2_{zz}. This was done to separate different quantities in Eq. (3-2) and Eq. (3-3). In fact, z is the same as x but only x will be used further. This convention is used in Burridge (1980)). The boundary conditions for Eq. (3-3) on the half line $x > 0$ are:

$$-\left(\rho v^2\right) u_z = -\eta^2 u_x, \ at \ z = 0 \tag{3-5}$$

In order to get the physical meaning of the boundary conditions in Eq. (3-5) let's write one more equation. Hook's Law (in tensor form) can be further described as:

$$\boldsymbol{\sigma} = (K - \frac{2}{3}\mu)\mathbf{tr}\left(\frac{1}{2}\left((\nabla\mathbf{u}) + (\nabla\mathbf{u})^T\right)\right)\mathbf{I}_2 + 2\mu\left(\frac{1}{2}\left((\nabla\mathbf{u}) + (\nabla\mathbf{u})^T\right)\right) \tag{3-6}$$

where $\boldsymbol{\sigma}$ is the stress tensor, $\mathbf{I}_2$ is the second order identity tensor and $\mathbf{tr}$ is the trace of the 3×3 matrix. Since P-wave modulus is $(K + \frac{4}{3}\mu) = \rho v^2$, equation (3-6) shows the connection between the stress and the elastic displacement which is used in the boundary conditions (3-5). Therefore, the boundary conditions in Eq. (3-5) mean that the stress (L.H.S Eq. (3-5)) is given at $z = 0$. The boundary conditions (3-5) can be rewritten as:

$$-U_x(0,t) + \frac{\eta_x(0)}{\eta(0)}U(0,t) = 0 \tag{3-7}$$

Now, following Gelfand and Levitan (1951), I introduce the two Green's functions $\tilde{G}_1$ and $\tilde{G}$ which are causal and non-causal, respectively. $\tilde{G}_1$ satisfies (3-3) under the boundary conditions $-U_x(0,t) + (\eta_x(0)/\eta(0))U(0,t) = \delta'(t)$ (similar to (3-7)). The initial condition is $\tilde{G}_1(x,t) = 0$ for $t < 0$. The non-causal Green's function $\tilde{G}$ satisfies (3-3) under the boundary conditions (3-7) and the initial condition is $\tilde{G}(0,t) = 2\delta(t)$. Green's functions can be written as:

$$\tilde{G}(x,t) = \delta(x-t) + \delta(x+t) + \tilde{K}(x,t) \tag{3-8}$$

and

$$\tilde{G}_1(x,t) = \delta(x-t) - \tilde{K}_1(x,t) \tag{3-9}$$

$\tilde{K}$ and $\tilde{K}_1$ can be found in Gelfand and Levitan (1951) . Functions $\tilde{K}$ and $\tilde{K}_1$ represent the coda of the impulse response solutions but it will be explained in further detail in section 3-2-2. The solution for the potential is also given in Gelfand and Levitan (1951):

$$q(x) = 2\frac{\mathrm{d}}{\mathrm{d}x}\tilde{K}(x, \pm x) = 2\frac{\mathrm{d}}{\mathrm{d}x}\tilde{K}_1(x, x) \tag{3-10}$$

Therefore, once $\tilde{K}$ and $\tilde{K}_1$ are known, the solution of (3-3) can be derived from (3-10).

At the same time, the temporal Fourier transform of Eq. (3-3) is the steady-state Schrödinger equation:

$$-\omega^2 U - U_{xx} + q(x)U = 0, \tag{3-11}$$

where $-\omega^2$ represents $\partial^2/\partial t^2$ in the frequency domain. The Gelfand-Levitan-Marchenko theory was mainly developed for the steady-state Schrödinger equation (3-11) but it can be applied in the time-space domain for the 1D wave equation.

The most important idea in this theory (Lamb Jr, 1980; Burridge, 1980) is that the fundamental solution is divided into two parts: the delta pulse and the functions $\tilde{K}$ or $\tilde{K}_1$. This idea plays a key role in future developments by Rose (2002, 2001) (1D problem) and by Wapenaar et al. (2014b) (3D problem).

3-2-2 The 1D Marchenko Integral Equations

Let us consider the problem (3-3) with $q(x) = 0$ in $x < 0$. In the domain $x < 0$ we have the solution in the form (Burridge, 1980):

$$u(x, t) = f(t - x) + g(t + x) \tag{3-12}$$

The f is zero if we consider only left-going solutions in the domain $x < 0$ and $U_x = U_t = g'(t + x)$. For example, we can write:

$$U_x(0, t) = U_t(0, t) \tag{3-13}$$

Equation (3-13) will play a very important role later. The basic solution with only right-going wave in the domain $x < 0$ is:

$$G(x, t) = \delta(t - x) + K(x, t). \tag{3-14}$$

K is bounded by $\delta(t - x)$ and by a set of points $(x, t) \in (t + x)$, i.e. $supp(K) := |t| \leq x$. The support of K, denoted by $supp(K)$, is the smallest closed set outside of which K vanishes (Folland, 1999). In our case, K vanishes outside the cone (see Figure 3-1) and the boundary defined by $\delta(t - x)$ (solid line in Figure 3-1) and by a set of points $(x, t) \in (t + x)$ (dashed line in Figure 3-1).

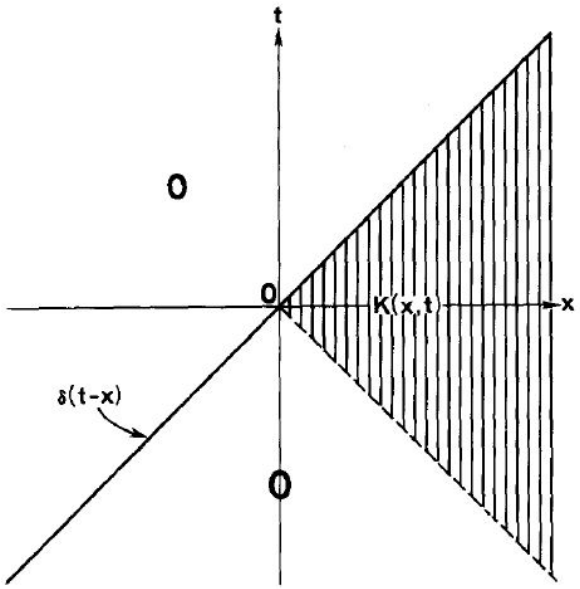

Figure 3-1: The non-causal Green's function $G(x,t) = \delta(x,t) + K(x,t)$ is shown. K vanishes outside the cone and the boundaries defined by $\delta(t-x)$ (solid line) and a set of points $(x,t) \in (t+x)$ (dashed line). [Modified after Burridge (1980)]

A left-going wave in the solution in domain $x < 0$ is the time-reversed Eq. (3-14) (using the fact that δ is an even distribution, i.e. $\delta(-t-x) = \delta(t+x)$):

$$\bar{G}(x,t) = G(x,-t) = \delta(t+x) + K(x,-t). \tag{3-15}$$

Thus, the solution can be written as (see the basic theory in chapter 2, particularly, Eq. (2-5)):

$$\begin{aligned} U(x,t) = \int \bar{G}(x,\tau)U(0,t-\tau)\mathrm{d}\tau = \\ U(0,t+x) + \int_{-x}^{x} K(x,-\tau)U(0,t-\tau)\mathrm{d}\tau = \\ U(0,t+x) + \int_{-x}^{x} K(x,\tau)U(0,t+\tau)\mathrm{d}\tau \end{aligned} \tag{3-16}$$

Next, we define the causal Green's function G_1:

$$G_1(x,t) = \delta(t-x) + K_1(x,t), \tag{3-17}$$

where K_1 is bounded (analogous to K but in the upper half-space), $supp(K_1) := |x| \leq t$ (see Figure 3-2).

After subtracting Eq. (3-14)) from Eq. (3-17)) we have:

$$\tilde{G}(x,t) = -K(x,t) + K_1(x,t), \tag{3-18}$$

where $\tilde{G}(x,t) = G_1(x,t) - G(x,t)$. By replacing $U = \tilde{G}$ in Eq. (3-16) we can write:

$$\tilde{G}(x,t) = \tilde{G}(0,t+x) + \int_{-x}^{x} K(x,\tau)\tilde{\mathrm{G}}(0,t+\tau)\mathrm{d}\tau \tag{3-19}$$

At the same time, it is obvious that

$$K(x,t) = -\tilde{G}(x,t), \ \ for\ x > |t|, \tag{3-20}$$

$$K_1(0,t) = R(t) = \tilde{G}(0,t). \tag{3-21}$$

Thus, using (3-19), Eq. (3-20) and (3-21) we can write the Marchenko integral equation for $t < x$ as:

$$R(t+x) + K(x,t) = -\int_{-t}^{x} K(x,\tau)R(t+\tau)d\tau \tag{3-22}$$

The geometrical interpretation of the Marchenko equation is shown in Figure 3-3. Indeed, K and K_1 can be represented as a coda events — everything instead of the delta pulse. The goal of this chapter is to demonstrate this visual interpretation. In fact, the application of the integral equation (3-16) to the Green's function $\tilde{G}$ (3-18)) is shown in Figure 3-3, where the region of integration $0 < t - \tau < t + x$ (pink line). The Marchenko equation has a very strong connection with the Gelfand-Levitan equation which is shown in Burridge (1980). While the Marchenko equation was derived to recover the potential, this new impulse-response interpretation has a very important contribution to the inverse problem solution for hyperbolic equations, i.e. the wave equation. Originally, equation (3-22) is solved for K, then the potential can be found, as it is shown in the previous section. At the same time a similar solution can be found in Lamb Jr (1980). The interpretation of Eq. (3-22) in terms of seismic applications is shown in the next section.

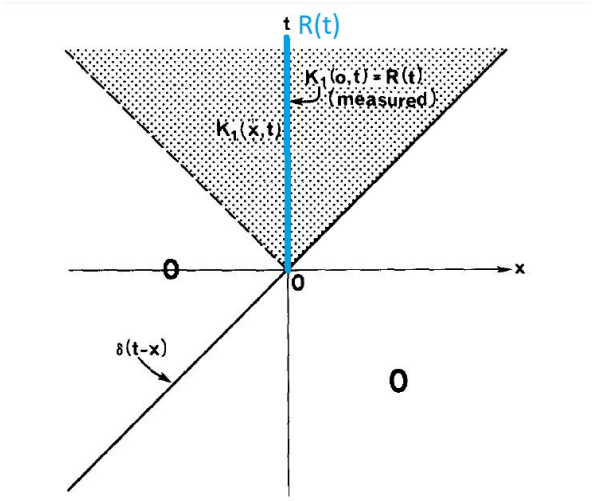

Figure 3-2: The causal Green's function $G_1(x,t) = \delta(x,t) + K_1(x,t)$ is shown. The blue line is the reflected data (i.e. recorded data). [Modified after Burridge (1980)]

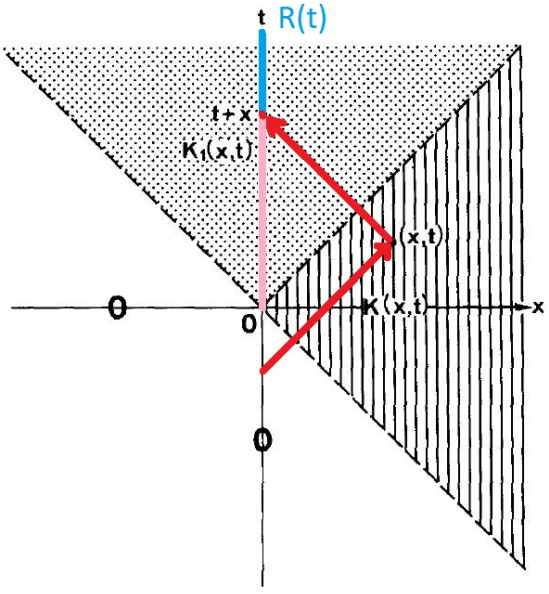

Figure 3-3: The causal Green's function and the focusing solution. Red arrows shows the relation between the focusing function and the recorded data. Pink line is the region of integration $0 < t + \tau < t + x$. [Modified after Burridge (1980)]

3-3 Single-sided Autofocusing

The importance of the 1D inverse problem solution being an exact solution plays an essential role in seismic imaging. Rose (2002) showed that the Marchenko equation might be used to focus the wave field in the 1D medium. The question stated in Rose (2002) is, "Given single-sided access, how does one focus sound to a point inside a one-dimensional layered medium at a specified time-given that the velocity profile is unknown?" From a modern perspective in 1D, the wave field can be focused inside the medium if the focal point is defined in scaled depth. In order to translate from scaled depth to real depth, a smooth velocity model is needed. The most important contribution of Rose to Marchenko Imaging is that he linked autofocusing and inverse scattering (Broggini and Snieder, 2012; Wapenaar et al., 2014a). This important contribution made it possible to use the Marchenko equation in seismic imaging and seismic interferometry. This means that instead of having a physical source in the subsurface, we can focus the wave field in the subsurface, using physical sources and receivers at the surface only. Then, we can apply a well-developed seismic interferometry theory. Broggini and Snieder (2012) showed the connections between different inverse scattering techniques in different areas, i.e. seismology, quantum mechanics, optics and others. The last equation in the section 3-2 is the 1D version of the Marchenko equation (3-22). For wave propagation it can be rewritten as (Broggini and Snieder, 2012):

$$R(t+t_f) + \tilde{u}(t,t_f) = -\int_{-\infty}^{t_f} \tilde{u}(\tau,t_f) R(t+\tau) d\tau, \tag{3-23}$$

where $R(t)$ is the reflected scattering amplitude to the incident wave field $\tilde{u}(t,t_f)$ and t_f is a parameter that controls the focusing location. In terms of the wave propagation problem, the solution of Eq. (3-23) focuses the wave field inside the medium. A detailed study of similar equations will be given in the next few chapters.

Another important equation which arises in the wave propagation and scattering problems is the Lippmann-Schwinger equation:

$$u^{\pm}(n,\mathbf{x}) = u_0(n,\mathbf{x}) + \int G_0^{\pm}(\mathbf{x},\mathbf{x}') L'(\mathbf{x}') u^{\pm}(n,\mathbf{x}') d\mathbf{x}', \tag{3-24}$$

Here, $u^{\pm}(n,\mathbf{x})$ is the total wave field, $u_0(n,\mathbf{x})$ is the incident (unperturbed) wave field, n is the direction of the wave field propagation. The superscripts $+$ and $-$ in the Green's function correspond to the causal and anti-causal Greens function with outgoing or ingoing boundary conditions, respectively (Broggini and Snieder, 2012). At the same time, the superscripts $+$ and $-$ in the wave field illustrate the forward and backward propagation, respectively (meaning, the wave fields are time-reversed in the space-time domain). The integral represents the scattered wave field caused by perturbations $L'(\mathbf{x}') \equiv L(\mathbf{x}) - L_0(\mathbf{x})$. This equation can be used to derive the Newton-Marchenko equation and a generalized optical theorem. The Newton-Marchenko is the same as the Marchenko equation, but it requires reflection and transmission data — meaning, it's a two-sided problem. Since, all scattering principles are connected with each other, Eq. (3-24) plays an essential role in the wave scattering problems. The Lippmann-Schwinger equation describes wave propagation and scattering in inhomogeneous media. The connection between the different types of Lippmann-Schwinger equations, describing micro (5-10) and macro scale (3-24) wave propagation will be shown later.

3-4 3D Marchenko Equations for Wave Propagation

According to Broggini and Snieder (2012), there are three wave scattering problems. The 1D inverse scattering problem which can be solved via the Gelfand-Levitan-Marchenko equation. The second problem is focusing, i.e. focusing the wave field inside the medium via an incident wave field. The third problem is Green's function retrieval. In general, inverse scattering methods estimate perturbations in medium properties from recorded scattered wave fields. This is an exact integral equation which relates the scattered field measured on one side of the medium to its interior inhomogeneities. Therefore, all of these problems are connected.

According to Green's Theorem, we can correctly retrieve the Green's functions of the medium if the data are available from all sides of the medium. Unfortunately, in seismic imaging we usually deal with single-sided data. The term "single-sided" means that the data are available only from one side of the medium. In seismic exploration it can be the reflection data. Green's functions retrieval becomes an extremely ill-posed problem if only single-sided data are available. Fortunately, using several assumptions, this problem can be solved by using the 3D Marchenko equation (Wapenaar et al., 2014b). The main assumptions are: [1] the medium is lossless; [2] the total Green's function can be represented as a superposition of the up- and down-going components; [3] the reflection response is properly sampled in space and time; [4] an estimate of the first-arrival travel-time from the focusing point to the acquisition surface is given; and [5] for imaging a velocity model is required. The 3D Marchenko Equation's solution's main feature is the focusing function. It represents the injected wave field from one side of the medium which focuses inside the medium at a focal point. Furthermore, the focusing function is defined in such a way that it doesn't generate multiples at the focal point. They are removed via the inverse-polarity wave field in the focusing function at a specific time, in such a way, that the multiples are cancelled. From a mathematical point of view, the focusing function is, in fact, a fundamental solution of the Marchenko equation with specific boundary conditions, as shown in chapter 3-1. These specific boundary conditions are defined in the truncated medium, which is identical to the physical medium between the injection and focal points but reflection free below the focusing level. Therefore, by using the 3D Marchenko equation, we can retrieve the Green's function from a virtual receiver in the medium. However, we must have a single-sided data (i.e. the reflection response) and an estimate of the first-arrival travel-time from the virtual receiver to the acquisition surface.

In this work, it is assumed that surface-related (i.e. free-surface) multiples have been removed. Examples on how to achieve this can be found in Verschuur and Berkhout (1997) and Amundsen (2001). Alternatively, the methodology of Singh et al. (2015) can be used to modify the focusing algorithm provided by Wapenaar et al. (2013) in such a way that the free-surface multiples are incorporated.

3-4-1 Green's Functions

In this work, t denotes time, $\mathbf{x} = (\mathbf{x}_H, z)$ is the spatial coordinate vector. Here, $\mathbf{x}_H = (x, y)$ refers to the horizontal coordinates of the space. The positive z-axis is pointing downward. If a location is fixed in depth, the spatial coordinates are noted as $\mathbf{x}_0 = (\mathbf{x}_H, z_0)$. The exact location of the source is defined as $\mathbf{x}'_0 = (x'_0, y'_0, z'_0)$. I defined the Green's function G as the

causal solution of the Eq. (2-4) with the operator L and modified right hand-side:

$$LG = -\rho\delta(\mathbf{x} - \mathbf{x}_0')\frac{\partial\delta(t)}{\partial t} \tag{3-25a}$$

$$L = \rho\nabla\cdot\left(\frac{1}{\rho}\nabla\right)[\cdot] + \frac{1}{V^2}\frac{\partial^2}{\partial t^2}[\cdot] \tag{3-25b}$$

where $V = V(\mathbf{x})$ is the propagation velocity. Note, that in the section 1 of chapter 3 , I defined the propagation velocity as $v = v(z)$ because of 1D nature of the problem. $\rho = \rho(\mathbf{x})$ is the density of the inhomogeneous medium. The Eq. (3-25a) states that the Green's function $G(\mathbf{x}, \mathbf{x}_0', t)$ is the response at location $\mathbf{x}$ to the impulsive point source at location $\mathbf{x}_0'$ of the lossless inhomogeneous medium. The Green's function $G(\mathbf{x}, \mathbf{x}_0', t)$ can be decomposed to the downgoing part $G^{+,+}(\mathbf{x}, \mathbf{x}_0', t)$ and upgoing part $G^{-,+}(\mathbf{x}, \mathbf{x}_0', t)$. The first superscript in $G^{\pm,+}(\mathbf{x}, \mathbf{x}_0', t)$ denotes the up- or down-going part, i.e. minus denotes the upgoing part; the second superscript denotes the response due to up- or down-going source, i.e. plus means the down-going source. The relations between $G(\mathbf{x}, \mathbf{x}_0', t)$, $G^{+,+}(\mathbf{x}, \mathbf{x}_0', t)$ and $G^{-,+}(\mathbf{x}, \mathbf{x}_0', t)$ for flux- and pressure- normalized wave fields can be found in Wapenaar and Grimbergen (1996). For flux-normalized wave field, the relationship is more complicated than for the pressure-normalized wave fields, where the up- and down-going wavefields can be simply superposed.

3-4-2 Reciprocity Theorems

The temporal Fourier transform is defined as

$$p(\mathbf{x}, \omega) = \int_{-\infty}^{+\infty} p(\mathbf{x}, t) exp(-j\omega t) dt \tag{3-26a}$$

$$p(\mathbf{x}, t) = \frac{1}{2\pi}\int_{-\infty}^{+\infty} p(\mathbf{x}, \omega) exp(j\omega t) d\omega, \tag{3-26b}$$

where j is the imaginary number, ω is the angular frequency. For simplicity, I will use the same symbol for time- and frequency domain function p.

In this work the derivations are given in terms of flux-normalized one-way wave fields. The derivation of the 3D Marchenko equations is possible using the flux-normalization and pressure-normalized wave fields; but for practical applications pressure-normalized wave fields are preferable. On the other hand, by using the flux-normalized wave field, the derivation of the 3D Marchenko equations becomes simple (i.e. formulas are slightly simpler) than for pressure-normalized wave fields. That is why in this thesis equations are given in terms of flux-normalized one-way wave fields. The acoustic pressure and particle velocity identify the acoustic wave field in the space-time domain. In the space-frequency domain, the relations between two-way and one-way wave fields are given by (Wapenaar et al., 2014a):

$$\begin{pmatrix} p \\ v_z \end{pmatrix} = \begin{pmatrix} \mathcal{L}_1 & \mathcal{L}_1 \\ \mathcal{L}_2 & -\mathcal{L}_2 \end{pmatrix} \begin{pmatrix} p^+ \\ p^- \end{pmatrix} \tag{3-27}$$

$$\begin{pmatrix} p^+ \\ p^- \end{pmatrix} = \begin{pmatrix} \mathcal{L}_2^t & \mathcal{L}_1^t \\ \mathcal{L}_2^t & -\mathcal{L}_1^t \end{pmatrix} \begin{pmatrix} p \\ v_z \end{pmatrix} \tag{3-28}$$

In Eq. (3-27), Eq. (3-28) $\mathcal{L}_1$ and $\mathcal{L}_2$ are pseudo-differential operators and superscript t denotes operator transposition. Eq. (3-28) is valid for the one-way fields which are normalized with respect to acoustic power flux. According to Eq. (3-27) the relation between acoustic pressure and one-way wave fields is:

$$p = \mathcal{L}_1 \left(p^+ + p^- \right) \tag{3-29}$$

A very detailed representation of operator $\mathcal{L}_1$ as well as relations between flux- and pressure-normalized wave fields can be found in Wapenaar and Grimbergen (1996) and in Wapenaar (1998).

Reciprocity theorems form the essential basis for 3D Marchenko Imaging. Wave fields are defined in two states — A and B (indicated by subscripts A and B) in the space-frequency domain. The theorems formulate general relations between two independent states (Wapenaar et al., 2014a) — A and B. It is assumed that the medium parameters between $\partial\mathbb{D}_0$ and $\partial\mathbb{D}_i$ are the same in states A and B. The visual illustration is shown a little later in this chapter in Figure 3-4. For flux-normalized one-way wave fields the theorems can be written as:

$$\int_{\partial\mathbb{D}_0} (p_A^+ p_B^- - p_A^- p_B^+) d^2\mathbf{x} = \int_{\partial\mathbb{D}_i} (p_A^+ p_B^- - p_A^- p_B^+) d^2\mathbf{x} \tag{3-30a}$$

$$\int_{\partial\mathbb{D}_0} (p_A^+ p_B^{+*} - p_A^- p_B^{-*}) d^2\mathbf{x} = \int_{\partial\mathbb{D}_i} (p_A^+ p_B^{+*} - p_A^- p_B^{-*}) d^2\mathbf{x} \tag{3-30b}$$

where the asterisk $(*)$ denotes complex conjugation. Eq. (3-30a) represents the reciprocity theorem of the convolution type and Eq. (3-30b) represents the reciprocity theorem of the correlation type. It is assumed that there are no sources between two boundaries $\partial\mathbb{D}_0$ and $\partial\mathbb{D}_i$ in Eq. (3-30a)-(3-30b) and the media is lossless between $\partial\mathbb{D}_0$ and $\partial\mathbb{D}_i$.

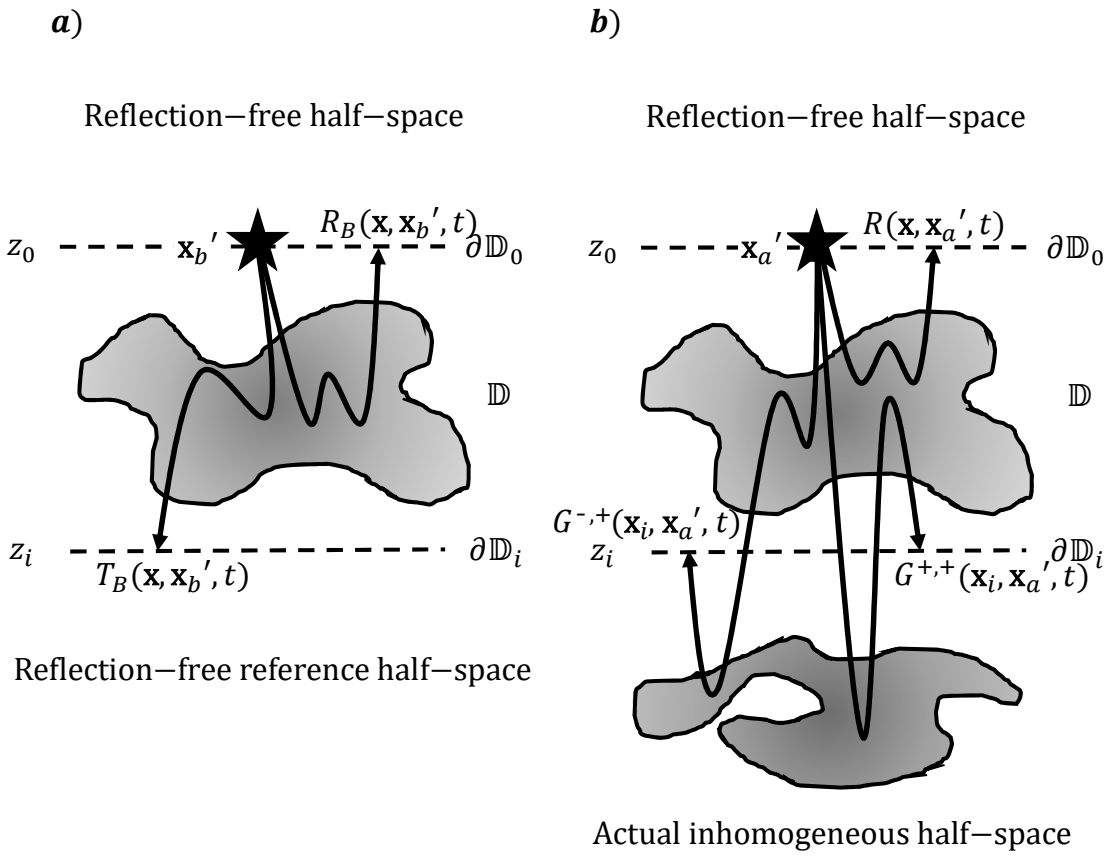

Figure 3-4: Two states that are used in the the reciprocity theorems (a) State A: the medium properties are identical to the physical medium between $\partial\mathbb{D}_0$ and $\partial\mathbb{D}_i$ but reflection free below $\partial\mathbb{D}_i$. (b) State B: the medium properties are identical to the physical medium between $\partial\mathbb{D}_0$ and $\partial\mathbb{D}_i$. Also, the medium properties are identical to the physical medium below $\partial\mathbb{D}_i$. [Modified after (van der Neut et al., 2015)].

3-4-3 Focusing Functions

It was shown in chapter 2-1 that the Marchenko equation can be used to solve the one-dimensional (1D) inverse scattering problem. In other words, the Marchenko equation links the single-sided data (i.e. the reflection response) to the field inside the medium. The concept of fundamental solutions is used to solve the steady-state Schrödinger equation in 1D (Lamb Jr, 1980; Burridge, 1980). This approach was extended to 3D case (Wapenaar et al., 2013). In this derivation, focusing functions are, in fact, fundamental solutions of the 3D Marchenko equation. The focusing function (or the fundamental solution) of the first type $f_1(\mathbf{x}, \mathbf{x}'_i, t)$ is defined such as it focuses at $\mathbf{x}_\mathrm{H} = \mathbf{x}'_{\mathrm{H,i}}$ at depth level $\mathbb{D}_i$ and continues as a downgoing wave field $f_1^+(\mathbf{x}, \mathbf{x}'_i, t)$ (Wapenaar et al., 2014b). The formal focusing condition is:

$$f_1(\mathbf{x}_\mathrm{H}, x_3 = x_{3,i}, \mathbf{x}'_i, t) = \delta(\mathbf{x}_\mathrm{H} - \mathbf{x}'_{\mathrm{H,i}})\delta(t) \tag{3-31}$$

The focusing function $f_1(\mathbf{x}, \mathbf{x}'_i, t)$ can be decomposed as:

$$f_1(\mathbf{x}, \mathbf{x}'_i, t) = f_1^+(\mathbf{x}, \mathbf{x}'_i, t) + f_1^-(\mathbf{x}, \mathbf{x}'_i, t) \tag{3-32}$$

Note, that evanescent field of $f_1(\mathbf{x}, \mathbf{x}'_i, t)$ is excluded at the focusing depth level (i.e. at depth level $\mathbb{D}_i$). This is done to avoid instabilities in $f_1(\mathbf{x}_\mathrm{H}, x_3 = x_{3,i}, \mathbf{x}'_i, t)$. It means that the delta function becomes a spatially band limited delta function (it affects the resolution of the image). The focusing function (or the fundamental solution) of the second type $f_2(\mathbf{x}, \mathbf{x}'_0, t)$ is similar to the focusing function $f_1(\mathbf{x}, \mathbf{x}'_i, t)$, but $f_2(\mathbf{x}, \mathbf{x}'_0, t)$ focuses at at depth level $\mathbb{D}_0$ (i.e. $f_2(\mathbf{x}, \mathbf{x}'_0, t)$ focuses to the focal point from below (Brackenhoff, 2016)).

$$f_2(\mathbf{x}_\mathrm{H}, x_3 = x_{3,0}, \mathbf{x}'_0, t) = \delta(\mathbf{x}_\mathrm{H} - \mathbf{x}'_{\mathrm{H},0})\delta(t) \tag{3-33}$$

The decomposition is similar:

$$f_2(\mathbf{x}, \mathbf{x}'_0, t) = f_2^+(\mathbf{x}, \mathbf{x}'_0, t) + f_2^-(\mathbf{x}, \mathbf{x}'_0, t) \tag{3-34}$$

Similarly, evanescent field of $f_2(\mathbf{x}, \mathbf{x}'_0, t)$ is excluded at the focusing depth level (i.e. at depth level $\mathbb{D}_0$). The visual interpretation of the two types of the focusing functions is shown in Figure 3-5.

3-4-4 Green's Functions Retrieval

Reciprocity theorems are used to obtain the Green's function representations. Again, all wave fields are flux-normalized. As it was introduced before, wave fields are defined in two states A and B (indicated by subscripts A and B). The truncated medium identified as a medium A in state A, therefore, the subscript A will be used. The downgoing field of the source (observed just below the source) in state A is $p_A^+(\mathbf{x}_0, \omega) = \delta(\mathbf{x}_{H,0} - \mathbf{x}'_{H,a})$. Here, $\mathbf{x}'_a$ is the horizontal

position of the source. The source which generates $p_A^+(\mathbf{x}_0,\omega)$ is placed just above depth level z_0. Here, the 2D Dirac delta function represents the source at horizontal location $\mathbf{x}'_a$ in state A. At the same time, the upgoing component at depth level z_0 is $p_A^-(\mathbf{x}_0,\omega) = R_A(\mathbf{x}_0,\mathbf{x}'_a;\omega) = R_A(\mathbf{x}_{\rm H},z_0;\mathbf{x}'_a,z_0;\omega)$. The function $R_A(\mathbf{x}_{\rm H},z_0;\mathbf{x}'_a,z_0;\omega)$ is the reflection response at depth level z_0 of the truncated medium. At depth level z_i the downgoing part is $p_A^+(\mathbf{x}_i,\omega) = T_A(\mathbf{x}_i,\mathbf{x}'_a;\omega) = T_A(\mathbf{x}_{\rm H},z_i;\mathbf{x}'_a,z_0;\omega)$. The function $T_A(\mathbf{x}_{\rm H},z_i;\mathbf{x}'_a,z_0;\omega)$ is the transmission response of the truncated medium.

The state B is defined as the actual inhomogeneous media. Similarly, the point source which generates the downgoing wave field is $p_B^+(\mathbf{x}_0,\omega) = \delta(\mathbf{x}_{H,0}-\mathbf{x}'_{H,b})$. The upgoing component at depth level z_0 is the reflection response of the inhomogeneous media: $p_B^-(\mathbf{x}_0,\omega) = R(\mathbf{x}_0,\mathbf{x}'_b;\omega) = R(\mathbf{x}_{\rm H},z_0;\mathbf{x}'_b,z_0;\omega)$. At depth level z_i (i.e. focusing level) the downgoing part is $p_B^+(\mathbf{x}_i,\omega) = G^{\pm,+}(\mathbf{x}_i,\mathbf{x}'_b;\omega) = G^{\pm,+}(\mathbf{x}_{\rm H},z_i;,\mathbf{x}'_b,z_0;\omega)$, i.e. the impulse response due to the wave filed generated by $\delta(\mathbf{x}_{H,0}-\mathbf{x}'_{H,b})$ source.

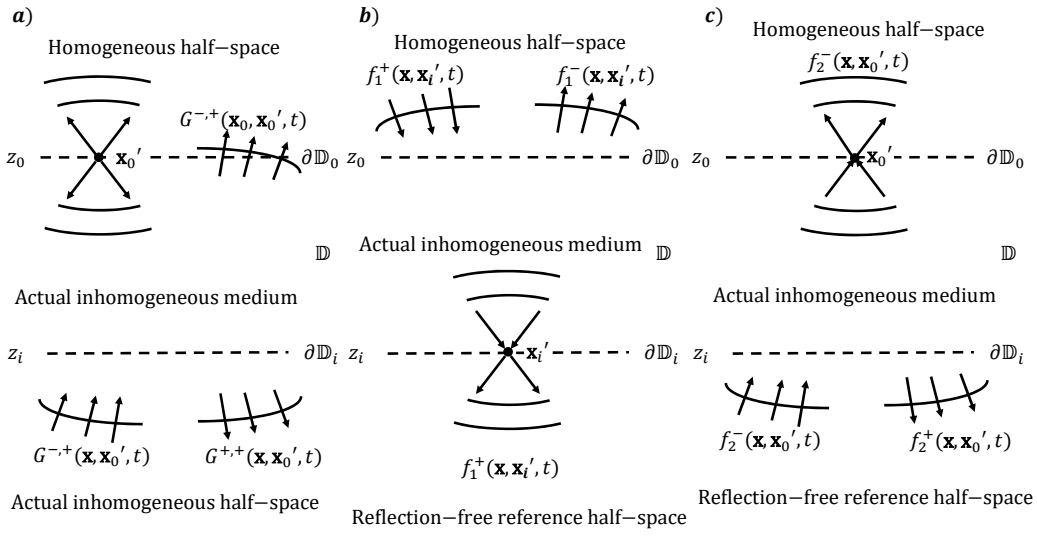

Figure 3-5: Green's function and two types of focusing functions. (a) Green's function $G(\mathbf{x},\mathbf{x}'_0;t)$ of the 3D inhomogeneous equation due to a source $\mathbf{x}'_0$ and upgoing and downgoing components of the Green's function. (b) Focusing function of the first type $f_1(\mathbf{x},\mathbf{x}'_i,t)$ which focuses to the focal point $\mathbf{x}'_i$. (c) Focusing function of the second type $f_2(\mathbf{x},\mathbf{x}'_0,t)$ which focuses to the focal point $\mathbf{x}'_0$. [Modified after (Wapenaar et al., 2014b)]

Now, we can write the following equations substituting the above expressions for states A and B to the reciprocity theorems Eq. (3-30a)-(3-30b):

$$R(\mathbf{x}'_a, z_0; \mathbf{x}'_b, z_0; \omega) - R_A(\mathbf{x}'_b, z_0; \mathbf{x}'_a, z_0; \omega) = \int_{\partial\mathbb{D}_i} T_A(\mathbf{x}_\mathrm{H}, z_i; \mathbf{x}'_a, z_0; \omega) G^{-,+}(\mathbf{x}_\mathrm{H}, z_i; \mathbf{x}'_b, z_0; \omega) d^2\mathbf{x}_\mathrm{H} \quad (3\text{-}35)$$

$$\int_{\partial\mathbb{D}_0} R_A(\mathbf{x}_\mathrm{H}, z_0; \mathbf{x}'_a, z_0; \omega) R^*(\mathbf{x}_\mathrm{H}, z_0; \mathbf{x}'_b, z_0; \omega) d^2\mathbf{x}_\mathrm{H} - \delta(\mathbf{x}'_b - \mathbf{x}'_a) = - \int_{\partial\mathbb{D}_i} T_A(\mathbf{x}_\mathrm{H}, z_i; \mathbf{x}'_a, z_0; \omega) G^{+,+*}(\mathbf{x}_\mathrm{H}, z_i; \mathbf{x}'_b, z_0; \omega) d^2\mathbf{x}_\mathrm{H} \quad (3\text{-}36)$$

The downgoing part of the focusing function is defined as:

$$\delta(\mathbf{x}_\mathrm{H} - \mathbf{x}'_F) = \int_{\partial\mathbb{D}_0} T_A(\mathbf{x}_\mathrm{H}, z_F; \mathbf{x}'_a, z_0; \omega) f_1^+(\mathbf{x}'_a, z_0; \mathbf{x}'_F, z_i; \omega) d^2\mathbf{x}'_a, \quad (3\text{-}37)$$

where we defined f^+ as the inverse of T_A, $\mathbf{x}'_F$ is the horizontal coordinate of the focal point. The response of the truncated medium to f^+ is:

$$f_1^-(\mathbf{x}_\mathrm{H}, z_0; \mathbf{x}'_F, z_F; \omega) = \int_{\partial\mathbb{D}_0} R_A(\mathbf{x}_\mathrm{H}, z_0; \mathbf{x}'_a, z_0; \omega) f_1^+(\mathbf{x}'_a, z_0; \mathbf{x}'_F, z_i; \omega) d^2\mathbf{x}'_a \quad (3\text{-}38)$$

Substituting Eq. (3-37) and Eq. (3-38) into the Eq. (3-35) and Eq. (3-36) we get:

$$G^{-,+}(\mathbf{x}'_F, z_i; \mathbf{x}'_b, z_0; \omega) + f_1^-(\mathbf{x}'_b, z_a; \mathbf{x}'_F, z_i; \omega) = \int_{\partial\mathbb{D}_0} R(\mathbf{x}, z_0; \mathbf{x}'_b, z_0; \omega) f_1^+(\mathbf{x}, z_0; \mathbf{x}'_F, z_i; \omega) d^2\mathbf{x} \quad (3\text{-}39)$$

$$G^{+,+*}(\mathbf{x}'_F, z_i; \mathbf{x}'_b, z_0; \omega) - f_1^+(\mathbf{x}'_b, z_a; \mathbf{x}'_F, z_i; \omega) = - \int_{\partial\mathbb{D}_0} R^*(\mathbf{x}, z_0; \mathbf{x}'_b, z_a; \omega) f_1^+(\mathbf{x}, z_0; \mathbf{x}'_F, z_i; \omega) d^2\mathbf{x} \quad (3\text{-}40)$$

Equations (3-39)-(3-40) will be used later to retrieve the Green's functions. Later, in discrete notation, it will be shown that in order to obtain $G^{-,+}$ and $G^{+,+*}$ only the direct arrival and the single-sided reflection response are needed.

3-4-5 Discrete Marchenko Equations

In this section, equations (3-39)-(3-40) will be rewritten in a discrete notation and the coupled Marchenko equations will be derived. Next, the iterative approach will be introduced to solve the coupled Marchenko equations. Equations (3-39) and (3-40) can be written in space-time domain:

$$G^{-,+}(\mathbf{x}_F, z_i; \mathbf{x}'_b, z_0; t) + f^{-}(\mathbf{x}'_b, z_a; \mathbf{x}'_F, z_i; t) = \int_{-\infty}^{\infty}\int_{\partial\mathbb{D}_0} R(\mathbf{x}, z_0; \mathbf{x}'_b, z_0; t-\tau) f^{+}(\mathbf{x}, z_0; \mathbf{x}'_F, z_i; t) d\tau \quad (3\text{-}41)$$

and

$$G^{+,+*}(\mathbf{x}_F, z_i; \mathbf{x}'_b, z_0; t) - f_1^{+}(\mathbf{x}'_b, z_a; \mathbf{x}'_F, z_i; t) = -\int_{-\infty}^{\infty}\int_{\partial\mathbb{D}_0} R(\mathbf{x}, z_0; \mathbf{x}'_b, z_a; t-\tau) f^{+}(\mathbf{x}, z_0; \mathbf{x}'_F, z_i; t) d\tau \quad (3\text{-}42)$$

In discrete form, equations (3-41) and (3-42) are

$$\mathbf{f}_1^{-} + \mathbf{g}^{-,+} = \mathbf{R}\mathbf{f}_1^{+} \quad (3\text{-}43)$$

and

$$\mathbf{f}_1^{+} - \mathbf{g}^{+,+*} = \mathbf{R}^{*}\mathbf{f}_1^{-}, \quad (3\text{-}44)$$

where vector $\mathbf{f}_1^{\pm}$ is the focusing function, vector $\mathbf{g}^{\pm,+}$ is the Green's function. Matrix $\mathbf{R}$ represents a complicated operation: the forward Fourier transformation, convolution with the reflection response and inverse Fourier transform which acts on the focusing function (see Eq. (3-41)). Matrix $\mathbf{R}^{*}$ is defined in a similar manner and determines cross-correlation with the reflection series which then acts on the upgoing focusing function. According to (van der Neut et al., 2015), I introduce a matrix window $\mathbf{\Theta}$ that removes the direct wave and the coda:

$$\mathbf{\Theta}\mathbf{g}^{-,+} = 0 \quad (3\text{-}45)$$

and

$$\mathbf{\Theta}\mathbf{g}^{+,+*} = 0 \quad (3\text{-}46)$$

The focusing function can be represented as the direct wave and the coda:

$$\mathbf{f}_1^+ = \mathbf{f}_{1d}^+ + \mathbf{f}_{1m}^+ \tag{3-47}$$

Applying $\mathbf{\Theta}$ to equation (3-47) gives:

$$\mathbf{\Theta}\mathbf{f}_1^+ = \mathbf{\Theta}(\mathbf{f}_{1d}^+ + \mathbf{f}_{1m}^+) = \mathbf{f}_{1m}^+ \tag{3-48}$$

and

$$\mathbf{\Theta}\mathbf{f}_1^- = \mathbf{f}_1^- \tag{3-49}$$

From (3-43) with help of (3-45), (3-47) and (3-49) we obtain:

$$\mathbf{f}_1^- = \mathbf{\Theta}\mathbf{R}\mathbf{f}_{1d}^+ + \mathbf{\Theta}\mathbf{R}\mathbf{f}_{1m}^+ \tag{3-50}$$

At the same time, from (3-44), (3-46), (3-47) and (3-48) we get:

$$\mathbf{f}_{1m}^+ = \mathbf{\Theta}\mathbf{R}^*\mathbf{f}_1^- \tag{3-51}$$

We can also retrieve the focusing function differently. By using (3-50) and (3-51) we obtain the equation which can be solved for $\mathbf{f}_{1m}^+$:

$$[\mathbf{I} - \mathbf{\Theta}\mathbf{R}^*\mathbf{\Theta}\mathbf{R}]\mathbf{f}_{1m}^+ = \mathbf{\Theta}\mathbf{R}^*\mathbf{\Theta}\mathbf{R}\mathbf{f}_{1d}^+ \tag{3-52}$$

Here, $\mathbf{I}$ is an identity matrix. Now, we observe that (3-52) is the Fredholm equation of the second kind. The solution of such type of equation is known and yields the Kth order estimate of $\mathbf{f}_1^+$:

$$\mathbf{f}_1^{+(K)} = \sum_{k=0}^{K} (\mathbf{\Theta}\mathbf{R}^*\mathbf{\Theta}\mathbf{R})^k \, \mathbf{f}_{1d}^+, \tag{3-53}$$

The solution for $\mathbf{f}_1^-$ can be found by inserting (3-50) into (3-52):

$$\mathbf{f}_1^{-(K)} = \mathbf{\Theta}\mathbf{R} \sum_{k=0}^{K} (\mathbf{\Theta}\mathbf{R}^*\mathbf{\Theta}\mathbf{R})^k \mathbf{f}_{1d}^+ \tag{3-54}$$

The convergence of Eq. (3-53) and is verified by van der Neut et al. (2015) under the condition that $\| (\mathbf{\Theta}\mathbf{R}^*\mathbf{\Theta}\mathbf{R})^k \, \mathbf{f}_{1d}^+ \|_2 \rightarrow 0$ as $k \rightarrow \infty$. $\| \cdot \|_2$ denotes the L^2-norm. The solutions for the upgoiung Green's functions is:

$$\mathbf{g}^{-,+(K)} = \mathbf{\Psi R} \sum_{k=1}^{K} (\mathbf{\Theta R}^{*} \mathbf{\Theta R})^{k} \mathbf{f}_{1d}^{+} \tag{3-55}$$

and

$$\mathbf{g}^{-,+(0)} = \mathbf{\Psi R} \mathbf{f}_{1d}^{+} \tag{3-56}$$

This result means that, first, we define $\mathbf{g}^{-,+(0)}$ using Eq. (3-56), and then, estimate the Green's function via Eq. (3-55). The solutions for the downgoing Green's functions is:

$$\mathbf{g}^{+,+*(K)} = [\mathbf{I} - \mathbf{\Psi R}^{*} \mathbf{\Theta R} \sum_{k=1}^{K-1} (\mathbf{\Theta R}^{*} \mathbf{\Theta R})^{k}] \mathbf{f}_{1d}^{+} \tag{3-57}$$

and

$$\mathbf{g}^{+,+*(0)} = \mathbf{f}_{1d}^{+} \tag{3-58}$$

Similarly, first, we define $\mathbf{g}^{+,+(0)}$ using Eq. (3-58), and then, estimate the Green's function via Eq. (3-57). Thus, equations (3-53)-(3-57) can be used to retrieve the Green's function $\mathbf{g}^{\pm,+(0)}$ and the focusing function $\mathbf{f}_{1}^{\pm}$.

3-4-6 Marchenko Redatuming

Marchenko equations can be used to redatum the receivers and the sources to any depth level $\mathbb{D}_i$. The upgoing and downgoing Green's functions are related via (Wapenaar et al., 2014b):

$$G^{-,+}(\mathbf{x}_i, \mathbf{x}', t) = \int_{\partial \mathbb{D}_i} d\mathbf{x} \int_{-\infty}^{\infty} R(\mathbf{x}_i, \mathbf{x}, \tau) G^{+,+}(\mathbf{x}, \mathbf{x}', t - \tau) d\tau \tag{3-59}$$

Here, $R(\mathbf{x}_i, \mathbf{x}, \tau)$ is the reflection response of the medium below depth level $\mathbb{D}_i$. This reflection response is defined in a medium which is identical to the actual medium below $\mathbb{D}_i$ and reflection-free above this depth level. (3-59) states that the downgoing Green's function at the new datum $\mathbb{D}_i$, convolved with the reflection response $R(\mathbf{x}_i, \mathbf{x}, \tau)$ gives the upgoing Green's function. The first integral means that $G^{+,+}(\mathbf{x}, \mathbf{x}', t - \tau)$ convolved with $R(\mathbf{x}_i, \mathbf{x}, \tau)$ and then integrated along all source positions of this reflection response at $\mathbb{D}_i$. Therefore, (3-59) can be solved via multidimensional deconvolution and image can be obtained (Broggini et al., 2014). In the 1D case, the solution of (3-59) becomes simple — deconvolution results in the redatumed reflection response at depth level $\mathbb{D}_i$.

On the other hand, we also can apply other imaging methods once the redatumed reflection response is obtained. It might be, for example, Reverse Time Migration or RTM (Amundsen and Robertsson, 2014). Also, we can the extract zero-time component of the redatumed

reflection response and repeat that for many depth levels $\mathbb{D}_i$. It is called Marchenko Imaging (Wapenaar et al., 2014b). Also, we can apply Full-Waveform Inversion (FWI) once we have obtained the redatumed reflection response. As you can see, there are many ways on how to get the image. In my opinion, Marchenko Redatuming is the most important issue.

3-5 Conclusion

In this chapter, the 3D Marchenko (Wapenaar et al., 2014b) equations were derived from the basic solution of the inverse scattering problem given by the Gelfand-Levitan-Marchenko equation (Marchenko, 1955; Gelfand and Levitan, 1951). The starting point has been done by Marchenko who has proved the theorems on the uniqueness of the 1D inverse scattering problem and provided a method to reconstruct the potential. Nowadays, it is known as the inverse Sturm-Liouville problem. The second step has been done by Burridge (1980) who showed that the Marchenko equation can be applied to solve the 1D inverse problems of wave propagation. Indeed, the most important idea was that the fundamental solution considered as the delta pulse and the function K (Burridge, 1980; Lamb Jr, 1980). The third step has been done by Rose (2001, 2002) who connected the inverse scattering problem and autofocusing. The fourth step has been done by Broggini and Snieder (2012), who connected the work of Rose to seismic interferometry. Finally, the fifth step has been done by Wapenaar et al. (2014b). In the latter paper the 3D extension of the Marchenko equation is given as well as the iterative scheme to its solution. It is assumed that the total Green's function can be represented as a superposition of the up- and down-going Green's functions. Furthermore, it is assumed that the media is lossless. It is clear that it is impossible to include seismic attenuation into the current iterative scheme without its modification. Furthermore, while the visual explanation of the focusing function is very straightforward (i.e. it is an incident wave field which focuses inside the medium and all corresponding multiples are removed via a complicated inverse-phase incident wave field) the Marchenko equations acts differently. In fact, the Marchenko equation creates the focusing function using the full reflection series, i.e. time doesn't play a role because the reconstruction of the focusing function proceeds simultaneously for all times. Therefore, it means that in order to include intrinsic attenuation into the scheme we should know the attenuation of the medium in advance! But that is an unknown parameter. Therefore, only an adaptive approach is possible. There are several methods which would work. According to the Marchenko equation, in order to account for Q-factor, we can either modify the reflection series or the focusing function. This thesis is focused on modifying the reflection series, using different compensation parameters. Alternatively, we could work with the focusing function — calculate the focusing function using different lossy reflection series that are compensated with different Q-factors — to produce the optimal solution, which corresponds to correct focusing.

Chapter 4

Viscoelasticity and Seismic Attenuation

Seismic attenuation plays an important role in seismic wave propagation. Over the past fifty years, a lot of work has been done in this area. Many models were developed to describe attenuation effects. Generally speaking, all forward-modeling approaches are split into two categories (Zhu and Harris, 2014). The first category implements attenuation in the frequency domain. In this case the wave propagation velocity becomes complex. The second approach uses different viscoelastic models to introduce the Q-factor, as a combination of springs and dashpots.

There are several attenuation mechanisms (Anderson, 1989; Arora et al., 2011): intrinsic attenuation, scattering and geometrical spreading. Geometric spreading is the energy density decrease caused by wavefront expansion. Therefore, the compensation for the geometrical spreading is straightforward. Intrinsic attenuation is the energy loss due to various physical processes such as defects, dislocations and grain boundaries (Anderson, 1989). Scattering attenuation is the transferring and scattering of elastic energy due to inhomogeneities in the media. It also includes seismic wave reflection and refraction. Therefore, scattering attenuation is not an energy loss to heat but rather a conversion of elastic energy and production of scattering waves.

In partially saturated rocks, many other sophisticated attenuation mechanisms exists — including different types of wave-induced fluid flow at microscopic and mesoscopic scales. Indeed, it was shown that wave-induced fluid flow is the major cause of intrinsic seismic attenuation at different frequency ranges: from seismic to sonic (Müller et al., 2010; Rubino and Holliger, 2013). Some of these effects can be taken into account by using Biots theory of dynamic poroelasticity (Biot, 1956a,b, 1962). Dynamic-equivalent-medium models can be used to describe interlayer flow between poroelastic layers: for a periodically stratified medium (White et al., 1975) and for randomly fluctuated layer properties (Gurevich and Lopatnikov, 1995). Some important results can be found in (Carcione et al., 2003; Qi et al., 2014). A very comprehensive review can be found in Müller et al. (2010).

In seismic imaging, reducing computational costs is an essential task. Therefore, very complicated frequency-dependent attenuation or quality factor parameters are not desirable in such problems. Kjartansson (1979) proposed a constant Q-factor model in the time domain which produces very accurate results within the seismic bandwidth. Also, constant or near-constant Q-factor models can be created via an approximation of the generalized Zener model (Carcione, 2014).

In this work, the forward modelling of the lossy reflection series was done using a constant attenuation factor for a simple model and using a generalized Maxwell model which will be explored in detail in section 4-5. The compensation for the attenuation was performed using a constant attenuation factor which is convenient in seismic imaging. There were three models studied as part of this project: [1] amplitude damping model, [2] a generalized Maxwell model with two independent parameters, [3] a generalized Maxwell model with one independent parameter. In order to compensate for the losses, three models were applied: [A] a constant Q-factor model, [B] an effective Q-factor model and [C] a time-dependent Q-factor model.

4-1 Stress-Strain Relationships

The basic theory of linear viscoelasticity can be found in various literature, for example in Christensen (1982) and Carcione (2014). The modulus M in the viscoelastic solid becomes complex. Attenuation can be added in the frequency domain by complex valued elastic moduli and/or density. In the time domain, attenuation can be introduced by the relaxation tensor ψ_{ijkl}. Following Carcione (2014), the stress-strain relationship in viscoelastic media is (using index or Einstein notation):

$$\sigma_{ij}(\mathbf{x},t) = \psi_{ijkl}(\mathbf{x},t) * \partial_t \epsilon_{kl}(\mathbf{x},t) \tag{4-1}$$

where $*$ represents time convolution, ψ_{ijkl} are the components of the relaxation tensor, σ_{ij} and ϵ_{kl} are the components of the second order strain and stress tensors, respectively. Equation (4-1) can be written in tensor form:

$$\boldsymbol{\sigma} = \boldsymbol{\Psi} * \partial_t \boldsymbol{\epsilon} = \partial_t \boldsymbol{\Psi} * \boldsymbol{\epsilon} \tag{4-2}$$

Consider a n-dimensional Euclidean space with the basis being orthonormal, $\{a_i\}$, $i = \overline{1,...,n}$. Therefore, the stress tensor is $\boldsymbol{\sigma} = \sigma_{ij} a_i \otimes a_j$ and the basis is $a_i \otimes a_j$ (i.e. dyadic basis, see Appendix A). The strain tensor is $\boldsymbol{\epsilon} = \epsilon_{kl} a_k \otimes a_l$ and the basis is $a_k \otimes a_l$. The symbol $\otimes$ denotes the tensor product. Equation Eq. (4-2) accounts for the fact that the value of stress tensor depends on the history of the strain field which is shown by time derivatives.

In the short matrix or Voigt notation, Eq. (4-1) can be written as:

$$\bar{\boldsymbol{\sigma}}_v = \boldsymbol{\Psi}_v * \partial_t \bar{\boldsymbol{e}}_v, \tag{4-3}$$

where

$$\bar{\boldsymbol{\sigma}}_v = (\sigma_1, \sigma_2, \sigma_3, \sigma_4, \sigma_5, \sigma_6)^T = (\sigma_{11}, \sigma_{22}, \sigma_{33}, \sigma_{23}, \sigma_{13}, \sigma_{12})^T \tag{4-4}$$

and

$$\bar{\boldsymbol{e}_v} = (e_1, e_2, e_3, e_4, e_5, e_6)^T = (e_{11}, e_{22}, e_{33}, e_{23}, e_{13}, e_{12})^T = (\epsilon_{11}, \epsilon_{22}, \epsilon_{33}, 2\epsilon_{23}, 2\epsilon_{13}, 2\epsilon_{12})^T \tag{4-5}$$

In this case, the stress $\bar{\boldsymbol{\sigma}}_v$ and the strain $\bar{\boldsymbol{e}}_v$ are both 6×1 matrices. The relaxation tensor determines the viscoelastic behaviour of the solid. For example, stress and strain can be related through different models: Kelvin-Voigt solid, Standard Linear Solid (Zener), etc..

4-2 Wave Propagation in Viscoelastic Solid

Wave propagation of monochromatic plane waves in viscoelastic media can be written as (in terms of displacement):

$$u(x,t) = u_0\, e^{[j(\omega t - kx)]} \tag{4-6}$$

Thus, the medium is subjected to average sinusoidal strain $exp(j\omega t)$ (Hashin, 1970):

$$\boldsymbol{\sigma} = \boldsymbol{\sigma}_0 exp(j\omega t) \tag{4-7}$$

and

$$\boldsymbol{\epsilon} = \boldsymbol{\epsilon}_0 exp(j\omega t) \tag{4-8}$$

Furthermore, the Fourier transformation of Eq. (4-2) gives:

$$F\left[\boldsymbol{\sigma}(\boldsymbol{t})\right] = \mathbf{M}(\omega) F\left[\boldsymbol{\epsilon}(\boldsymbol{t})\right] \tag{4-9}$$

where $F[\cdot]$ denotes the Fourier transform operator (3-26a) and

$$\mathbf{M}(\omega) = F\left[\partial_t \boldsymbol{\Psi}(t)\right] = \int_{-\infty}^{+\infty} \partial_t \boldsymbol{\Psi}(t) exp(-j\omega t) \mathrm{d}t \tag{4-10}$$

The coefficient of proportionality between stress and strain is the complex elastic moduli $\mathbf{M}(\omega)$ (Hashin, 1970):

$$\mathbf{M}(\omega) = \mathbf{M}_R(\omega) + j\mathbf{M}_I(\omega) \tag{4-11}$$

In Eq. (4-11), $\mathbf{M}_R(\omega)$ represents a real part of the complex elastic moduli and $\mathbf{M}_I(\omega)$ represents an imaginary part of the complex elastic moduli. Furthermore, in terms of the relaxation tensor, $\mathbf{M}_R(\omega)$ and $\mathbf{M}_I(\omega)$ are (Carcione, 2014):

$$\mathbf{M}_R(\omega) = \omega \int_0^{+\infty} \mathbf{\Psi}(t) sin(\omega t) \mathrm{d}t \tag{4-12}$$

and

$$\mathbf{M}_I(\omega) = \omega \int_0^{+\infty} [\mathbf{\Psi}(t) - \mathbf{\Psi}(\infty)] \, cos(\omega t) \mathrm{d}t \tag{4-13}$$

I assumed that the medium is isotropic and replaced $\mathbf{M}(\omega)$ by $M(\omega)$ (in the lossless case M is the Lame constants, $M = \lambda + 2\mu$). Therefore, the complex velocity is:

$$V_c = \frac{\omega}{k} = \sqrt{\frac{M(\omega)}{\rho}} \tag{4-14}$$

In (4-14), the wavenumber is complex $k = \kappa - j\alpha$; ω is real; α is the attenuation factor. With a complex wavenumber, equation (4-6) can be rewritten as:

$$u(x,t) = u_0 \, e^{[-\alpha(\omega)x]} e^{[j(\omega t - \kappa x)]} \tag{4-15}$$

Equation (4-15) shows that the attenuation coefficient is defined as the exponential decay coefficient of a harmonic wave (Mavko et al., 2009). According to Eq. (4-14), the phase velocity is:

$$V_p = \frac{\omega}{\kappa} = \left[\mathfrak{Re} \left(\frac{1}{V_c} \right) \right]^{-1} \tag{4-16}$$

It is possible to rewrite Eq. (4-14) where the wavenumber is real but ω is complex. In this case, the group velocity is:

$$V_g = \frac{\partial \omega}{\partial \kappa} = \left[\mathfrak{Re} \left(\frac{\partial k}{\partial \omega} \right) \right]^{-1} \tag{4-17}$$

In the general case of a 3D anisotropic media, phase and group velocities are different. Furthermore, their propagation directions are different. Group velocity propagation is determined by the Umov-Poynting vector, whereas phase velocity propagation direction is determined by eigenvectors of the Christoffel equation. In 1D such an analysis is useless. Note, that in seismic imaging, equations are usually formulated in terms of particle velocity field v.

4-3 The Quality Factor Q

The quality factor Q is the measure of how dissipative material is Mavko et al. (2009). There are several definitions of Q-factor, but the most common definition is (O'connell and Budiansky, 1978):

$$\frac{1}{Q} = \frac{\mathfrak{Im}(M)}{\mathfrak{Re}(M)} \equiv \frac{M_I}{M_R} \tag{4-18}$$

The definition (4-18) will be used by default if another meaning is not considered. Eq. (4-18) means that the inverse Q-factor is determined by the ratio of imaginary and real parts of the complex elastic moduli. In terms of energy, Q is (O'connell and Budiansky, 1978):

$$\frac{1}{Q} = \frac{\Delta E}{4\pi E} \tag{4-19}$$

ΔE is the energy dissipated per cycle under a harmonic loading. E is the average stored energy. Note, that in terms of spatial attenuation factor and for low-loss media ($Q > 1$) we can write:

$$\alpha = \frac{\omega}{2Q_{sp}V_p} = \frac{\pi f}{Q_{sp}V_p} \tag{4-20}$$

$2\pi f = \omega$ and Q_{sp} defines the spatial quality factor. Therefore, we can rewrite Eq. (4-15) as:

$$u(x,t) = u_0 exp\left[-\frac{\pi f}{Q_{sp}V_p}x\right] exp[j(\omega t - kx)] \tag{4-21}$$

At the same time, we can define a temporal quality factor for larger times as the exponentially decaying amplitudes $u(t)$:

$$u(t) = u_0 exp\left[-\frac{\pi f_0}{Q_{tm}}t\right] \tag{4-22}$$

f_0 is the central frequency of the source wavelet, Q_{tm} is the temporal Q-factor. In other words, Eq. (4-22) determines the damping factor which acts on the wavefields. Therefore, for lossy wavefield compensation purposes in the time domain the temporal quality factor Q_{tm} plays an essential role.

4-4 The Kramers-Kronig Relationship

The Kramers-Kronig relationship describes the connection between modulus-frequency dispersion and Q-factor in the viscoelastic media. It was first derived by Kramers and Kronig (Kramers, 1927). The complete derivation of these relations for a general physical system

can be found in Landau and Lifshitz (1969). The essential properties of the $M(\omega)$ function (which are used in the proof) are: $M(\omega)$ is holomorphic and $M(\omega)$ is single-valued (or, briefly, $M(\omega)$ is a regular function). The derivation uses some theorems from complex analysis. The Kramers-Kronig relationship is also known as causality constraints (Landau and Lifshitz, 1969; ODonnell et al., 1981). Since Ψ is is real and $M(\omega)$ is Hermitian (Carcione, 2014):

$$F\left[\partial_t \Psi(t)\right] = M_R(\omega) - \left(\frac{j}{\pi\omega}\right) * M_R(\omega) \tag{4-23}$$

Therefore, the causality is:

$$M_I(\omega) = -\frac{1}{\pi} p.v. \int_{-\infty}^{+\infty} \frac{M_R(\omega')}{\omega' - \omega} \mathrm{d}\omega' \tag{4-24}$$

and

$$M_R(\omega) = \frac{1}{\pi} p.v. \int_{-\infty}^{+\infty} \frac{M_I(\omega')}{\omega' - \omega} \mathrm{d}\omega' \tag{4-25}$$

$p.v.$ denotes the Cauchy principal value. Therefore, the real and imaginary parts of elastic moduli are linked via Hilbert transform. Equations (4-24)-(4-25) can be rewritten as (Mavko et al., 2009):

$$M_R(\omega) = M_R(0) - \frac{\omega}{\pi} \int_{-\infty}^{+\infty} \frac{M_I(\omega')}{\omega'} \frac{\mathrm{d}\omega'}{\omega' - \omega} \tag{4-26}$$

and

$$M_I(\omega) = \frac{\omega}{\pi} \int_{-\infty}^{+\infty} \frac{M_R(\omega') - M_R(0)}{\omega'} \frac{\mathrm{d}\omega'}{\omega' - \omega} \tag{4-27}$$

In equations (4-26)-(4-27), $M_R(0)$ represents the real part of the modulus at zero frequency. In other words, $M_R(0)$ is an instantaneous elastic response from the viscoelastic solid (Mavko et al., 2009). In terms of the quality factor, (4-26)-(4-27) becomes:

$$Q^{-1}(\omega) = -\frac{|\omega|}{\pi M_R(\omega)} \int_{-\infty}^{+\infty} \frac{M_R(\omega') - M_R(0)}{\omega'} \frac{\mathrm{d}\omega'}{\omega' - \omega} \tag{4-28}$$

The inverse of Eq. (4-28) is:

$$M_R(\omega) - M_R(0) = -\frac{\omega}{\pi} \int_{-\infty}^{+\infty} \frac{Q^{-1}(\omega) M_R(\omega')}{\omega'} \frac{\mathrm{d}\omega'}{\omega' - \omega} \tag{4-29}$$

According to equations (4-26)-(4-27), a larger attenuation is associated with larger dispersion. In fact, there are many ways to model attenuation, but the Kramers-Kronig relations put

some constraints on the material's behaviour. Therefore, these constraints make it possible to link velocity dispersion and Q-factor in a linear viscoelastic solid (Mavko et al., 2009). The main problem with the practical application of the Kramers-Kronig relation is that usually we don't know all frequencies of $M_R(\omega)$. By using equations (4-2)-(4-5), we can apply the Kramers-Kronig relationship to the general case of viscoelastic media.

4-5 The Dissipative Scalar Wave Equation with Two Independent Parameters

Let us consider the general equation Eq. (2-1) as a wave equation — corresponding to the complex frequency-domain scalar Helmholtz equation with operator L (de Hoop, 2001):

$$L\hat{G} = -\delta(\mathbf{x}) \tag{4-30}$$

$$L = (\partial_m \partial_m + \hat{\gamma}^2) \tag{4-31}$$

where $\hat{\gamma}$ is the wave number. $\hat{\gamma} = (\alpha_H \beta_H - \omega^2/V^2 + j\omega(\alpha_H \cdot \rho + \beta_H \cdot \kappa))^{1/2}$. Here, α_H and β_H are two relaxation parameters which correspond to compressibility and bulk density dissipation, respectively. κ is the compressibility, or rather the inverse of bulk modulus. V is the wave speed. In other words, the dissipation is introduced as $\alpha_H + j\omega\kappa$ and $\beta_H + j\omega\rho$ in the frequency domain expression for the wave equation. The solution of (4-30)-(4-31) is the Green's function:

$$\hat{G} = exp(-\hat{\gamma}R)/(4\pi R) \tag{4-32}$$

R is the distance from a point source. Therefore, only for a special case of $\alpha_H = \beta_H$, we can write the solution of Eq. (4-30) as:

$$G = \frac{1}{4\pi R} exp\left(-\frac{\alpha_H \cdot t}{\kappa}\right)\delta(t - R/V) \tag{4-33}$$

While the solution for the lossless case is (for a homogeneous medium):

$$G = \frac{1}{4\pi R}\delta(t - R/V) \tag{4-34}$$

According to Eq. (4-33), the compensation in the form of $exp(\alpha t)$ can completely compensate attenuation in the lossy reflection series only in a special case. This model with two independent parameters will be used in the modelling of the lossy reflection series. As you can see, the definition of α_H and α (Eq. (4-33)) are different and we don't consider the exact formula between them.

4-6 Conclusion

The basic theory of linear viscoelasticity was shown on the basis of the relaxation tensor (Carcione, 2014). The definitions of the quality factor were given in terms of the energy dissipation; And, in terms of the ratio of the real and imaginary parts of the complex elastic moduli. Fortunately, the two definitions introduce the same quality factor (O'connell and Budiansky, 1978).

In general, the low frequency elastic modulus has lower attenuation than the high frequency elastic moduli within the desired bandwidth. This idea can be shown via a simple standard linear solid (or Zener) model (Carcione, 2014). Velocity dispersion and Q-factor frequency dependence are especially important in porous rock, filled with different fluids, but such a detailed research is outside the scope of this study. The constant Q-factor model as well as De Hoop's model (section 4-5) were used to model the lossy reflection response.

Chapter 5

Wave Propagation in Heterogeneous Rocks and Rock Physics Modeling

Wave Propagation in Heterogeneous Porous Rocks and Rock Physics are dramatically spreading research areas in geophysics nowadays. Amos Nur, one of the pioneers of Rock Physics and founder the Stanford Rock Physics Project, revolutionized how Rock Physics can be used in seismic exploration. Stanford Rock Physics Project research projects, nowadays, became very quantitative. The books (Mavko et al., 2009; Dvorkin et al., 2014; Avseth et al., 2010) can be used to create different rock physics constraints for seismic imaging, as well as, for the quantitative interpretation of seismic data.

Nowadays, lots of different rock physics models exist which describe rock properties at different scales and stress/strain regimes. There are three basic parameters which are essential in such a characterization of the rock: the moduli of the rock, density and attenuation. Unfortunately, nowadays, we are more likely using velocity or impedance to infer porosity, lithology and fluid, rather than using attenuation (Dvorkin and Mavko, 2006). That is because of: [A] only a few consistent and relevant field datasets and [B] the phenomenological complexity of available data. Thankfully, a lot of research has been done in the past few years on seismic attenuation. Now, Rock Physics can be used to improve seismic imaging which was shown by a few recent PhD dissertations at Stanford Exploration Project — for example: Shen (2016) and Li (2014). Also, important researches on seismic attenuation were done at TU Delft a few years ago by Zhubayev (2014) and Kudarova (2016).

This study is mostly focused on the Marchenko equation. Detailed research on different rock physics models for quantifying elastic properties and seismic attenuation is beyond the scope of this project. Instead, I focused on linking seismic imaging and rocks physics through rock's viscoelastisity and provide a method to model the Q-factor of the rock. The theoretical part of this work and a general work flow are very solid and can be used for a very complex medium. In this chapter you will find: [1] a general work flow of the Rock Physics Modelling, and [2] the T-matrix approach, which is used in this study.

5-1 The General Work Flow of Rock Physics Modelling

As was mentioned before, there are three basic parameters which describe rock: the modulus (or the stiffness tensor), density and attenuation of the rock. The modulus and attenuation are usually frequency dependent. Furthermore, these parameters are non-linearly dependent on applied stress and stress-strain relationship, in general, non-linear. Therefore, precisely speaking, rocks are not elastic or viscoelastic, etc. (Dvorkin et al., 2014). But according to our observations, rocks are more likely to have viscoelastic behaviour rather than elastic behaviour. Thus, viscoelasticity is a very good approximation of a rock's rheology. In practice, seismic waves propagate in the frequency range of approximately 10^1 (seismic) to 10^4 (sonic) Hz (Dvorkin and Mavko, 2006).

Rocks can be represented as a composite material — polycrystalline aggregate with pores and cracks. For non-reservoir rocks, we can use constant-Q models or slightly dispersive viscoelastic models. In fact, non-reservoir rocks produce some attenuation mainly because of the elastic heterogeneities in the rock, but that is not part of this study. The elastic moduli in a low-frequency regime can be calculated using different effective medium models — for example the T-matrix approach (Jakobsen et al., 2003). In such models, rocks are represented by a mixture of different minerals in a rock's matrix — for example, in carbonate rocks, the matrix consists of calcite. Of course, some calibrations with real data are needed. For reservoir rocks, the modelling becomes more difficult.

In fact, there are several rock physics models which can predict Q-factor from the rock's properties. In our frequency range of four orders of magnitude, pore-scale Biot and squirt flow attenuation mechanisms are not relevant. Within the seismic bandwidth, the theory provided by Shapiro and Müller (1999) can create the desired $1/Q$ versus frequency curves which can be used for a detailed simulation of fluid-saturated reservoir rocks. This is also important for seismic imaging and monitoring of such fluid-saturated rocks because of the strongly inelastic behaviour of those. This analysis might be very important for synthetic studies and for applications on real data.

The main idea is that the Q-factor is linked to the changes in the elastic modulus versus frequency (Dvorkin and Mavko, 2006). A linear viscoelastic solid represented by a Zener model is a very simple illustration of this link (Mavko et al., 2009; Dvorkin et al., 2014; Carcione and Picotti, 2006) . We only need the low frequency moduli (i.e. the low frequency limit) and high frequency moduli (i.e. the high frequency limit) to construct the Zener model. This model produces two main curves: [A] the velocity-frequency curve which defines the velocity dispersion, and [B] Q^{-1} versus frequency curve which shows that higher frequencies attenuate stronger than lower frequencies. Therefore, the task is reduced to calculation of the low and high frequency elastic moduli. Eq. (4-2) which determines the stress-strain relationship in viscoelastic solid:

$$\boldsymbol{\sigma} = \partial_t \boldsymbol{\Psi} * \boldsymbol{\epsilon} \tag{5-1}$$

In a lossless case, the stress-strain relationship can be written as:

$$\boldsymbol{\sigma} = \mathbf{C}\boldsymbol{\epsilon} \tag{5-2}$$

$\mathbf{C}$ is the elastic modulus. $\mathbf{\Psi}(t) = \mathbf{C}H(t)$, where $H(t)$ is Heaviside function. In this study, the lossless moduli $\mathbf{C}$ will be used to construct the viscoelastic solid in the next few chapters.

The first simple approach for reservoir rocks is given by Dvorkin and Mavko (2006). At low frequencies we assume that the loading is slow. Therefore, the oscillations of the pore pressure equilibrate. In this case, low frequency rock physics models can be applied for elastic moduli calculations — calculating the moduli using Gassmann's equation. In other words, the low-frequency compressional modulus is calculated by theoretically substituting the pore fluid into the spatially averaged rocks dry-frame modulus (Dvorkin and Mavko, 2006). High frequency moduli are calculated by the spatial average of the saturated-rock modulus.

The second approach is rather different. Instead of a very simple heuristic method we can use the dynamic T-matrix approach (Jakobsen, 2004). The dynamic T-matrix approach was also extended to a few types of fluid flow (Jakobsen and Chapman, 2009). This method is, in fact, a method from micromechanics but takes into account different types of fluid flow. In other words, at low frequencies, the dynamic T-matrix approach is Biot-Gassmann consistent while at higher frequencies it behaves like a viscoelastic solid. A quite similar result for seismic frequency band can be achieved using the static T-matrix approach (Jakobsen et al., 2003) and the Zener model simultaneously. In this case, I first calculated the dry moduli of a porous rock using the T-matrix method, and then used the Gassmann equation to fill the pores with different fluids. As a result I got the low-frequency rock's moduli. Secondly, I used the T-matrix method to calculate the moduli of the fluid-filled rock. In this case, pores were not sensitive with respect to fluid flow and, therefore, it produced the high-frequency elastic moduli. Thirdly, I used the low- and high- frequency elastic moduli as input parameters for the Zener model. For the lossy reflection response modelling, I used the low-frequency elastic moduli because the wave frequency is closer to the zero frequency limit and the Biot-Gassmann assumptions were fulfilled. But the Q-factor parameter was obtained through linear approximation of the Zener model. Therefore, the higher the difference between the low- and high- frequency elastic moduli, the higher the attenuation of the rock. This approach was used in this study. While in future research, more complicated models can be used to produce more sophisticated Q-factor behaviour as well as velocity dispersion.

5-2 The T-Matrix Approach

5-2-1 Some basic equations

In the local linear theory of elasticity, the local stress field linearly depends on the local strain field of the inhomogeneous medium. The idea is to provide a method which can be used to calculate the low- and high frequency elastic moduli and, then, use these moduli as input parameter for the Zener viscoelastic model. The T-matrix approach makes it possible to connect the microstructure of the rock with its effective properties. We can write a generalized Hooke's Law for the anisotropic elastic case (in tensor form) as:

$$\boldsymbol{\sigma}(\mathbf{x}) = \mathbf{C}(\mathbf{x}) : \boldsymbol{\epsilon}(\mathbf{x}), \tag{5-3}$$

or using index notation (Einstein):

$$\sigma_{ij}(\mathbf{x}) = C_{ijkl}(\mathbf{x})\epsilon_{kl}(\mathbf{x}) \tag{5-4}$$

where $\mathbf{C}(\mathbf{x})$ is the local stiffness tensor, and $\mathbf{x}$ is the spatial coordinates of the medium. The symbol ":" denotes the double dot product.

The effective stiffness tensor of the statistically homogeneous medium is determined as the coefficient of proportionality $\mathbf{C}^*$:

$$\langle\boldsymbol{\sigma}\rangle = \mathbf{C}^* : \langle\boldsymbol{\epsilon}\rangle \tag{5-5}$$

The stress and strain fields are averaged over the representative elementary volume (REV) of the inhomogeneous medium. We assume that the REV contains a sufficient number of inclusions such that the statistical averaging makes sense. The REV is much larger than the size of the heterogeneities in the medium. On the other hand, the volume's macroscopic physical properties coincide with the medium's macroscopic properties in terms of the spatial scale of interest being analyzed. The angular brackets $\langle\cdot\rangle$ denote volume averaging. Therefore, the averaging of the stress and strain fields over the representative elementary volume $\mathbf{V}$ can be written in the following form (for stress field):

$$\langle\boldsymbol{\sigma}\rangle = \frac{1}{\mathbf{V}}\int\limits_{\mathbf{V}} \boldsymbol{\sigma}(\mathbf{x})\mathrm{d}\mathbf{x} \tag{5-6}$$

The volume averaging for the strain field can be written similarly.

5-2-2 The T-Matrix

In this section all mathematical operations are written using operator or index notations. The stiffness tensor can be represented as:

$$\mathbf{C}(\mathbf{x}) = \mathbf{C}^{(L)} + \delta\mathbf{C}(\mathbf{x}) \tag{5-7}$$

where $\mathbf{C}^{(L)}$ is the elastic moduli of the matrix of the rock. At the same time, the quantity $\mathbf{C}^{(L)}$ can be chosen arbitrarily, i.e. there are some connections to the Biot-Willis parameter. The last term in the Eq. (5-7) can be expressed as the medium fluctuations: $\delta\mathbf{C}(\mathbf{x}) \equiv \mathbf{C}(\mathbf{x}) - \mathbf{C}^{(L)}$. Let us consider the general equation Eq. (2-2) with the operator L:

$$L_{ik}g^{(0)}_{km}(\mathbf{x}) = -\delta_{im}\delta(\mathbf{x}) \tag{5-8}$$

$$L_{ik} = \nabla_j C^{(L)}_{ijkl} \nabla_l \tag{5-9}$$

Equations (5-8)-(5-9) are called Navier equations. In general, the elastostatic problem is governed by three equations (Willis, 1981): the equilibrium equation $\nabla \cdot \boldsymbol{\sigma}(\mathbf{x}) = 0$, Hook's Law (5-3) and $\boldsymbol{\epsilon} = 1/2\left((\nabla \mathbf{u}) + (\nabla \mathbf{u})^T\right)$ (Landau and Lifshitz, 1986). The boundary conditions for the displacements are: $\mathbf{u} = \mathbf{u}^{\delta\Omega}(\mathbf{x})$, $\mathbf{x} \in \delta\Omega$, where $\delta\Omega$ is the external boundary of the solid.

The derivation of the full theory is beyond the scope of this work, therefore, only a few important aspects of the theory will be shown. A general integral equation for the strain field (5-10) is usually considered as a starting point (for the statistically homogeneous medium and homogeneous boundary conditions):

$$\boldsymbol{\epsilon}(\mathbf{x}) = \boldsymbol{\epsilon}^{(0)} + \int_{\Omega} \boldsymbol{\mathcal{G}}^{(\mathbf{0})}(\mathbf{x} - \mathbf{x}')\delta\mathbf{C}(\mathbf{x}')\boldsymbol{\epsilon}(\mathbf{x}')\mathrm{d}\mathbf{x}' \tag{5-10}$$

where the constant tensor $\boldsymbol{\epsilon}^{(0)}$ is the medium's strain field with the elastic moduli $\mathbf{C}^{(L)}$ under the action of the boundary conditions specified at infinity. In other words, Eq. (5-10) is the solution of Eq. (5-8)-Eq. (5-9). The tensor $\delta\mathbf{C}(\mathbf{x})$ is the difference between the inclusions' elastic moduli and the elastic moduli $\mathbf{C}^{(L)}$. The fourth rank tensor $\boldsymbol{\mathcal{G}}^{(\mathbf{0})}$ is the second derivative of the equilibrium equation (quasi-static version of the dynamic equations of motion in solid mechanics). The components of $\boldsymbol{\mathcal{G}}^{(\mathbf{0})}$ are (using index or Einstein notation):

$$\boldsymbol{\mathcal{G}}^{(\mathbf{0})} = \mathcal{G}^{(0)}_{ijkl} = -\frac{1}{4}\left(g^{(0)}_{ik,jl} + g^{(0)}_{jk,il} + g^{(0)}_{il,jk} + g^{(0)}_{jl,ik}\right) \tag{5-11}$$

The tensor $g^{(0)}$ is the Green's tensor of the equilibrium equation. The tensor component $g^{(0)}(\mathbf{x} - \mathbf{x}')$ determines the displacement component u_i emerging at point $\mathbf{x}$ of the elastic infinite homogeneous medium under the action of a unit force directed along the e_k-axis and applied at point $\mathbf{x}'$. Correspondingly, tensor $\mathcal{G}^{(0)}_{ijkl}$ determines the ij-th component of the strain tensor at the point $\mathbf{x}$ under the action of the kl-th pseudo-stress component at the point $\mathbf{x}'$ of the volume of the medium. The pseudostresses have the form $\delta\mathbf{C}(\mathbf{x}')\boldsymbol{\epsilon}(\mathbf{x}')$.

In the quantum scattering theory, equation (5-10) is the the Lippmann-Schwinger equation (Landau and Lifshitz, 1958). Note, that the Lippmann-Schwinger equation is equivalent to the steady state Schrödinger equation. Let us define the operator $\overline{\boldsymbol{\mathcal{G}}}$ in the following way:

$$\overline{\boldsymbol{\mathcal{G}}} = \int_{\Omega} \boldsymbol{\mathcal{G}}^{(\mathbf{0})}(\mathbf{x} - \mathbf{x}')\mathrm{d}\mathbf{x}' \tag{5-12}$$

From the standpoint of the quantum scattering theory, tensor $\boldsymbol{\mathcal{G}}^{(\mathbf{0})}$ is a propagator and $\delta\mathbf{C}$ are the scatters of the strain field in the direction from point $\mathbf{x}$ to point $\mathbf{x}'$ (Gubernatis and Krumhansl, 1975). We can write Eq. (5-10) in the form of the series:

$$\boldsymbol{\epsilon}(\mathbf{x}) = \boldsymbol{\epsilon}^{(0)} + \overline{\boldsymbol{\mathcal{G}}}\delta\mathbf{C}\boldsymbol{\epsilon}^{(0)} + \overline{\boldsymbol{\mathcal{G}}}\delta\mathbf{C}\overline{\boldsymbol{\mathcal{G}}}\delta\mathbf{C}\boldsymbol{\epsilon}^{(0)} + ..., \tag{5-13}$$

which is the Dyson series in the quantum scattering theory. The fourth rank tensor field $\mathbf{T}$ is:

$$\delta\mathbf{C}(\mathbf{x})\boldsymbol{\epsilon}(\mathbf{x}) = \mathbf{T}(\mathbf{x})\boldsymbol{\epsilon}^{(0)} \tag{5-14}$$

which connects the stress field in the medium with the boundary conditions. For simplicity, we will write the final equation for the effective elastic moduli as:

$$\mathbf{C}^* = \mathbf{C}^{(L)} + \langle\mathbf{T}\rangle\left(\mathbf{I}_4 + \langle\overline{\boldsymbol{\mathcal{G}}}\mathbf{T}\rangle\right)^{-1} \tag{5-15}$$

The derivation of this equation can be found in various literature, for example in Jakobsen et al. (2003), Gubernatis and Krumhansl (1975), and Zeller and Dederichs (1973). The equation (5-15) is exact but the tensors $\langle\mathbf{T}\rangle$ and $\langle\overline{\boldsymbol{\mathcal{G}}}\mathbf{T}\rangle$ can be calculated only approximately.

The medium consisting of the matrix and inclusions (ellipsoids) - are divided into families $\mathbf{r} = 1, 2, , ..., N$. Each family of inclusions has the elastic moduli $\mathbf{C}^{(r)}$, the volume concentration $\upsilon^{(r)}$, and aspect ratio $\alpha^{(r)}$. Subscript (α) corresponds to the volume $\boldsymbol{\Omega}^{(r)}_{(\alpha)}$ which occupies one family of inclusions. A detailed explanation can be found in Jakobsen et al. (2003). Tensor $\mathbf{t}^{(r)}$ is the T-matrix for one family of inclusions. The expression for $\mathbf{t}^{(r)}$ is similar to Eq. (5-14):

$$\delta\mathbf{C}^{(r)}_{(\alpha)}(\mathbf{x})\boldsymbol{\epsilon}^{(r)}_{(\alpha)}(\mathbf{x}) = \mathbf{t}^{(r)}_{(\alpha)}(\mathbf{x})\boldsymbol{\epsilon}^{(0)} \tag{5-16}$$

The T-matrix can be written as:

$$\mathbf{T} = \sum_r \mathbf{t}^{(r)}_{(\alpha)} + \sum_r\sum_{u\neq r}\mathbf{t}^{(r)}_{(\alpha)}\overline{\boldsymbol{\mathcal{G}}}^{(ru)}\mathbf{t}^{(u)}_{(\alpha)} + \sum_r\sum_{u\neq r}\sum_{v\neq u}\mathbf{t}^{(r)}_{(\alpha)}\overline{\boldsymbol{\mathcal{G}}}^{(ru)}\mathbf{t}^{(u)}_{(\alpha)}\overline{\boldsymbol{\mathcal{G}}}^{(uv)}\mathbf{t}^{(v)}_{(\alpha)} + ... \tag{5-17}$$

Equation (5-17) describes scattering in a typical many-body system. By selecting two-point, three-point, etc., correlation functions, each term in the right-hand side of Eq. (5-17) accounts for the interactions between the inclusions in the statistical case. The Dyson series (5-13) describes the interactions in the many-body system.

5-2-3 Generalized Optical Potential Approximation [1]

I introduce the *modified* Generalized Optical Potential Approximation (5-18)-(5-21). By the term *modified* I postulate a special choice of $\mathbf{C}^{(L)} = (1-\mathbf{f})\mathbf{C}^M + \mathbf{f}C^{FL}$ where parameter $\mathbf{f}$ is a function of the Biot-Willis parameter $\boldsymbol{\alpha}$; $\mathbf{C}^M$ is the elastic moduli of the matrix of the rock; $\mathbf{C}^{FL}$ is the elastic moduli of inclusions (Alkhimenkov and Bayuk, 2017). Physically, parameter $\mathbf{f}$ (or, in general sense, tensor) reflects the degree of connectivity between inclusions.

[1] In this section all operations are written using tensor notation.

The Generalized Optical Potential Approximation approach is given by Jakobsen et al. (2003).

The operator $\overline{\boldsymbol{\mathcal{G}}}^{(r)}$ was replaced by a constant tensor $\widehat{\overline{\boldsymbol{\mathcal{G}}}}^{(r)}$. Expressions (5-18)-(5-21) are presented in such a way that provides straightforward implementation in FORTRAN90, Matlab or any other software package:

$$\mathbf{C}^{*}_{OPA} = \mathbf{C}^{(L)} + \langle \mathbf{T} \rangle : \left(\mathbf{I}_4 + \langle \mathbf{T}^{-1} \rangle : \mathbf{B} \right)^{-1} \tag{5-18}$$

$$\langle \mathbf{T} \rangle = \sum_r \mathbf{t}^{(r)} \upsilon^{(r)} \tag{5-19}$$

$$\mathbf{B} = \sum_r \sum_s \upsilon^{(r)} \mathbf{t}^{(r)} : \widehat{\overline{\boldsymbol{\mathcal{G}}}}^{(rs)} : \mathbf{t}^{(s)} \upsilon^{(s)} \tag{5-20}$$

where $\upsilon^{(r)}$ is the volume concentration of inclusions of family $\mathbf{r}$. The constant tensor $\widehat{\overline{\boldsymbol{\mathcal{G}}}}^{(r)}$ is:

$$\widehat{\overline{\boldsymbol{\mathcal{G}}}}^{(r)} \approx \int g^{(s)}_{k)(i,j)(l}(\mathbf{x}) \mathrm{d}\mathbf{x} \tag{5-21}$$

Equation (5-18) means that the components of the tensor $\widehat{\overline{\boldsymbol{\mathcal{G}}}}^{(r)}$ are given by the integration of the singular component of the Green's tensor second derivative over the inclusion volume (Bayuk et al., 2007). Tensor $\widehat{\overline{\boldsymbol{\mathcal{G}}}}^{(rs)}$ can be calculated using the same formulas as tensor $\widehat{\overline{\boldsymbol{\mathcal{G}}}}^{(r)}$ but using the aspect ratio of the two-point correlation function, which defines the probability density for finding an **s**-type inclusion at point $\mathbf{x}'$, if there is an **r**-type inclusion at point $\mathbf{x}$ (Jakobsen and Johansen, 2005).

Likewise, tensor $\widehat{\overline{\boldsymbol{\mathcal{G}}}}^{(r)}$ can be defined as:

$$\widehat{\overline{\boldsymbol{\mathcal{G}}}}^{(r)} = -\mathbf{S}^{(r)} : \mathbf{S}^{(L)}, \tag{5-22}$$

where $\mathbf{S}^{(r)}$ is the Eshelby tensor (Eshelby, 1957), and $\mathbf{S}^{(L)}$ is the compliance tensor:

$$\mathbf{S}^{(L)} = \left(\mathbf{C}^{(L)} \right)^{-1} \tag{5-23}$$

Equations (5-18)-(5-23) fully describe the *modified* Generalized Optical Potential Approximation Method to calculate the low frequency elastic moduli of heterogeneous rocks. This approach can be considered as a long wavelength Biot-Gassman theory for porous rocks. Some practical aspects of this method are given in Alkhimenkov (2015). A comparison with other methods can be found in Jakobsen et al. (2003) and Alkhimenkov (2017).

5-3 Conclusion

In this chapter, a General Work Flow of the Rock Physics Modelling is given as well as the T-matrix approach to calculate the elastic moduli of rock. I linked seismic imaging to Rock Physics, using viscoelasticity. This theory is not restricted to 1D media, but can also be applied to 2D and 3D, as well. Because of the tensor nature of the theory, this modelling can be used for anisotropic viscoelastic media. Because more complex and realistic models are possible, this approach can be used universally to study how different rocks types (and how different fluids in reservoir rocks) affect seismic images. That is important for both exploring reservoirs and for monitoring subsurface flow reservoir rocks.

Chapter 6

Redatuming and Quantifying Attenuation from Reflection Data Using the Marchenko Equation

In this chapter, the theory and practical results of using the Marchenko Equation for Q-estimation and redatuming will be shown, which include: [6-1] the modeling results for lossy media, [6-2] the Artefacts Removal Method for Q-estimation and [6-3] Marchenko Redatuming in Viscoelastic media. In section [6-1], the lossy refection series behaviour for different models is illustrated. In section [6-2], the Artefact Removal Method for Q-estimation is shown. This method makes it possible to quantify attenuation using solely the Marchenko equation. This method was tested by several synthetic models. These models consist of several horizontal layers. The first model is the simplest one where each layer has the same velocity and attenuation. Other models have more complex velocity, density and attenuation profiles. In section [6-3] the Marchenko Redatuming in Viscoelastic media was performed using different models.

6-1 Modeling Results for Lossy Media: a Visual Tour

As it was shown in chapters 4 and 5, there are many attenuation mechanisms which describe intrinsic, transmission and scattering losses. Instead of studying one particular mechanism in seismic imaging, it is much more prominent to model attenuation through visloelasticity of the medium (Ursin and Toverud, 2002). In this case, attenuation in the viscoelastic solid is described as complex moduli. In the time domain, attenuation is described through the relaxation tensor which acts as the time convolution operator (Carcione, 2014). In this thesis, the forward modelling of the lossy reflection series was done using three methods: [1] amplitude damping model, [2] De Hoop's model with two independent parameters and [3] De Hoop's model with one independent parameter. These models were explained in detail in chapter 4.

The compensation for the attenuation was performed using [A] a constant Q-factor model, [B] an effective Q-factor model and [C] a time-dependent Q-factor model.

6-1-1 Constructing the Lossy Reflection Series

Assume, then the medium consists of N plane-parallel layers. Each layer has its own P-wave velocity Vp, density ρ and a Q-factor or attenuation which depends on the model. The lossless reflection response was modelled using the method proposed by Fokkema and Ziolkowski (1987). While this approach works for plane waves, I modeled the reflection response for 1D media. Following this approach, the incident wave field is the plane pressure wave:

$$P^{INC}(x,z,\omega) = A_0^+(\omega)\ exp(j\omega(p_0 x + q_0 z)) \tag{6-1}$$

A_0^+ is the spectrum of the wave field, p_0 is the horizontal slowness in the upper half-space and q_0 is the vertical slowness in the upper half-space. The reflection response is the wave field:

$$P^R(x,z,\omega) = A_0^-(\omega)\ exp(j\omega(p_0 x - q_0 z)) \tag{6-2}$$

In the case of 1D media, it is a wave field returning at normal angle. Therefore, the total wave field in the upper half-space is:

$$P^0(x,z,\omega) = exp(j\omega p_0 x)\ \left[\ A_0^+(\omega)\ exp\left(j\omega q_0 z\right) + A_0^-(\omega)\ exp(-j\omega q_0 z)\right] \tag{6-3}$$

I won't give all steps here but only mention a few important equations. The global reflection coefficient $R_n(\omega)$ for the n-th layer is defined as:

$$A_n^-(\omega) = R_n(\omega)\ A_n^+(\omega)\ exp(2j\omega q_n z_n) \tag{6-4}$$

where the subscript n corresponds to n-th layer. The global recursion formula for the global reflection coefficient is (Fokkema and Ziolkowski, 1987):

$$R_n(\omega) = \frac{\Gamma_n + R_{n+1}(\omega)\ exp(\ 2j\omega q_{n+1}(z_{n+1} - z_n)}{1 + \Gamma_n\ R_{n+1}(\omega)\ exp(\ 2j\omega q_{n+1}(z_{n+1} - z_n)} \tag{6-5}$$

where Γ_n is the local reflection coefficient. By inserting Eq. (6-5) into Eq. (6-4), I can rewrite Eq. (6-3) as:

$$P^0(x,z,\omega) = A_0^+(\omega)\ exp(j\omega px)\ \ [exp\left(j\omega q_0 z\right) + R_0(\omega)\ exp(j\omega q_0(2z_0 - z))] \tag{6-6}$$

In order to account for the losses, the elastic modulus and/or density must be complex numbers, so that they will provide a lossy reflection response.

6-1-2 Lossy Reflection Series Behaviour for Different Models

Amplitude Damping Model

In this modelling, the intrinsic loss was modelled as a constant-Q model. This is the most popular model used in seismic exploration. Indeed, within the seismic bandwidth, this assumption provides quite accurate results. The wavefields were multiplied with the damping factor $exp\left(-\frac{\pi f_0}{Q_{tm}}t\right)$ (Aki and Richards, 2002; Draganov et al., 2010). f_0 is the central frequency of the source wavelet. Q_{tm} is the temporal Q-factor. I frequently use parameter $\zeta_{damping}$ which is:

$$\zeta_{damping} = -\frac{\pi f_0}{Q_{tm}} \tag{6-7}$$

Therefore, I can rewrite the damping factor for amplitudes $u(t)$ as:

$$u(t) = u_0(t)\ exp\left(-\frac{\pi f_0}{Q_{tm}}t\right) = u_0(t)\ exp(-\zeta_{damping}\ t) \tag{6-8}$$

Thus, the compensation is:

$$u(t)_{compensated} = u(t)\ exp(+\zeta_{compensation}\ t) \tag{6-9}$$

The medium properties of the model that will be used to demonstrate this attenuation are shown in table C-1 on page 95. This is a simple constant-Q model. The central frequency of the source wavelet (Ricker wavelet) is $f_0 = 30$ Hz. $\zeta_{damping} = 0.8$ corresponds to $Q_{temporal} \approx 117.8$. The reflection series was calculated by convolving the reflection coefficients with the Ricker wavelet. Figure 6-1 shows the two reflection series. The first reflection series was calculated for lossless medium (black curve). The second reflection series was calculated for lossy medium. This model can be considered as an ideal model because by applying compensation (6-9), I will get the lossless reflection series. However, this is only the case if I know the true compensation parameter, i.e. $\zeta_{compensation} = \zeta_{damping}$. Even for this simple constant-Q model, if you don't know the true Q-factor of the model you won't be able to compensate for the losses.

When I used the lossy reflection series for Marchenko redatuming or Marchenko imaging, I got very poor results: many artefacts and multiples were present and the amplitudes of the primary reflections were wrong. To show these poor results, I focused below the second layer. The focal depth is 2000 meters. As was mentioned before, there are no multiples present in the first layer because there is no free surface. But there are multiples in the second layer. By focusing below the second layer, I could test how the lossless Marchenko scheme deals with lossy reflection response. In general, for the lossy model, the Green's functions and the focusing functions have very weak amplitudes for most cases. Also, there are some artefacts present. Figure 6-2 shows the upgoing Green's function $G^{-,+}$ for the lossless and lossy media. There is an artefact before the first arrival in $G^{-,+}$. Figure 6-3 is the same as Figure 6-2 but zoomed in to 1-2.5 seconds. This artefact is shown by an arrow. Figures D-1, D-2 and

D-3, show the downgoing Green's function, upgoing focusing function and downgoing focusing function, respectively. The first arrival in the lossy version of $G^{+,+}$ ('lossy version' meaning that the Green's/focusing functions were calculated using the lossy reflection response) has a stronger amplitude than the lossless $G^{+,+}$. But the coda events in the lossy version of $G^{+,+}$ have very low amplitudes (see Figure D-1). The lossy version of f_1^- has the same two events as the lossless version of f_1^-. The amplitudes of lossy f_1^- are much lower than in the lossless f_1^- (see Figure D-2). The lossy version of f_1^+ has two events as the lossless version of f_1^+. The amplitude of the first event of lossy f_1^- is slightly lower than the amplitude of the first event in the lossless f_1^-. But the second event in the lossy f_1^- has a very low amplitude compare to the lossless f_1^- (see Figure D-3). No additional artefact events are present in the lossy versions of $G^{+,+}$, f_1^+ and f_1^-. By applying compensation $\zeta_{compensation} = \zeta_{damping}$ to the lossy reflection series, we get the reflection response which is identical to the lossless one (Figure D-4). As you can see on Figure D-4, the black curve and the red curve coincide.

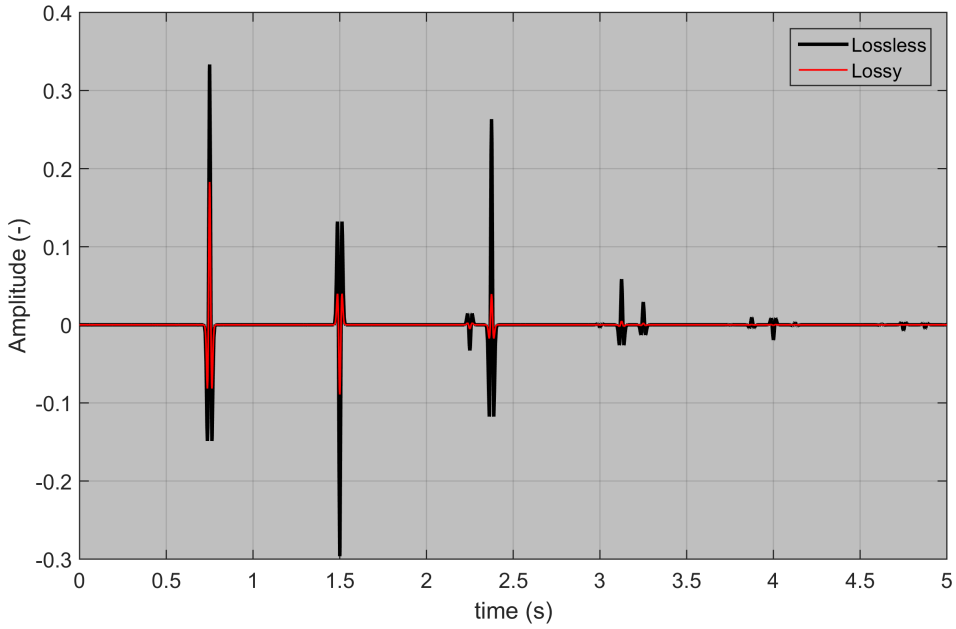

Figure 6-1: Lossless (black curve) and lossy (red curve) reflection series for Model 1. The x-axis represents time in seconds, the y-axis represents the amplitude. The intrinsic loss was modelled as an amplitude damping (Model 1) $\zeta_{damping} = 0.8$.

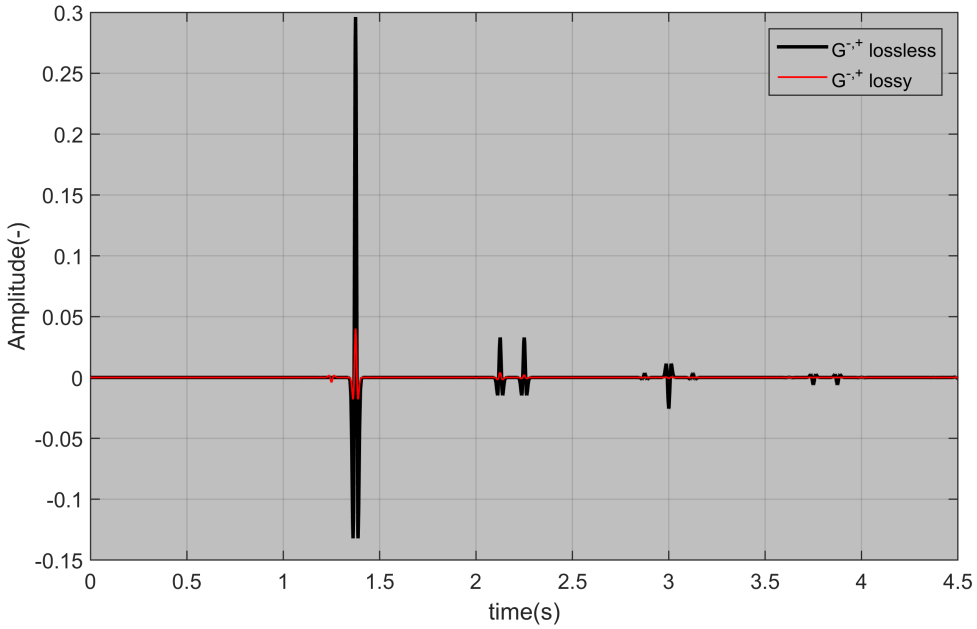

Figure 6-2: Upgoing Green's function $G^{-,+}$. The black curve is the lossless $G^{-,+}$. The red curve is the lossy $G^{-,+}$. The x-axis represents time in seconds. The y-axis represents the amplitude. The focal point is 2000 m depth. The intrinsic loss was modelled as an amplitude damping (Model 1).

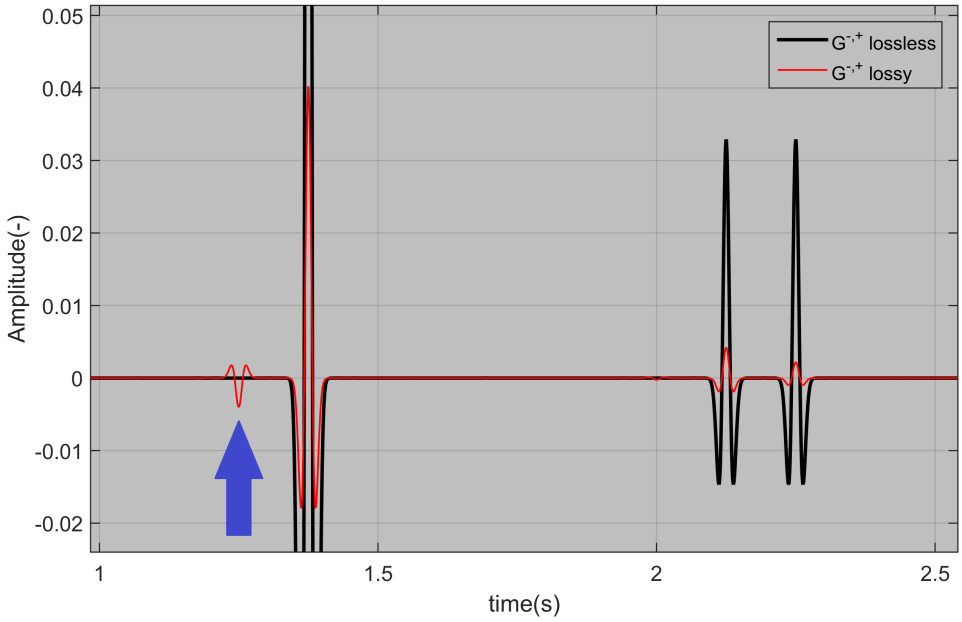

Figure 6-3: Upgoing Green's function $G^{-,+}$ zoomed in to 1-2.5 seconds. The black curve is the lossless $G^{-,+}$. The red curve is the lossy $G^{-,+}$. The artefact is shown by an arrow. The x-axis represents time in seconds. The y-axis represents the amplitude. Focal point is 2000 m depth. The intrinsic loss was modelled as an amplitude damping (Model 1) $\zeta_{damping} = 0.8$.

De Hoop's Model with Two Parameters

In this section, the method described in chapter 4-5 was used. It was assumed that the losses are incorporated through two parameters: the moduli and density of the rock. The medium properties are shown in table C-2 on page 95 (Model 2a). This model consist of five layers. Each layer has a different velocity and density. The attenuation parameter α_H is the same for all layers. Figure 6-4 shows the two reflection series. The first reflection series was calculated for lossless media (black curve). The second reflection series was calculated for lossy media. Note, that in this modelling, a simple exponent compensation factor won't completely compensate for attenuation. The compensation factor $\zeta_{compensation} = 0.4$ was applied to the lossy reflection series (see Figure 6-5). I found the value of $\zeta_{compensation}$ via solving the inverse problem (visually) — the best match between the lossless and compensated lossy reflection responses. The result is quite accurate but the compensated lossy reflection series doesn't completely coincides with the lossless reflection series. That is because the Q-factor is not the same for all frequencies; Therefore, it is impossible to compensate for the attenuation via a constant Q-factor. The compensation parameter $\zeta_{compensation} = 0.4$ corresponds to $Q_{temporal} \approx 235$. Also, the result is quite accurate because the attenuation is quite small. If attenuation is increased, the result is less accurate. But this phenomena will be further explored later.

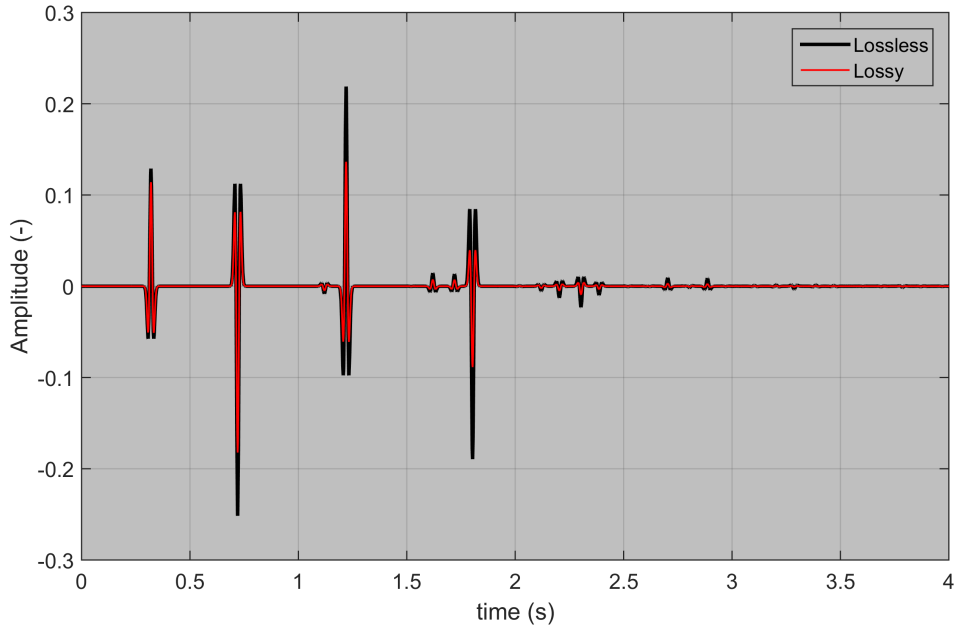

Figure 6-4: Lossless (black curve) and lossy (red curve) reflection series for Model 1. The x-axis represents time in seconds, the y-axis represents the amplitude. The intrinsic loss was modelled using De Hoop's model with two parameters (Model 2a).

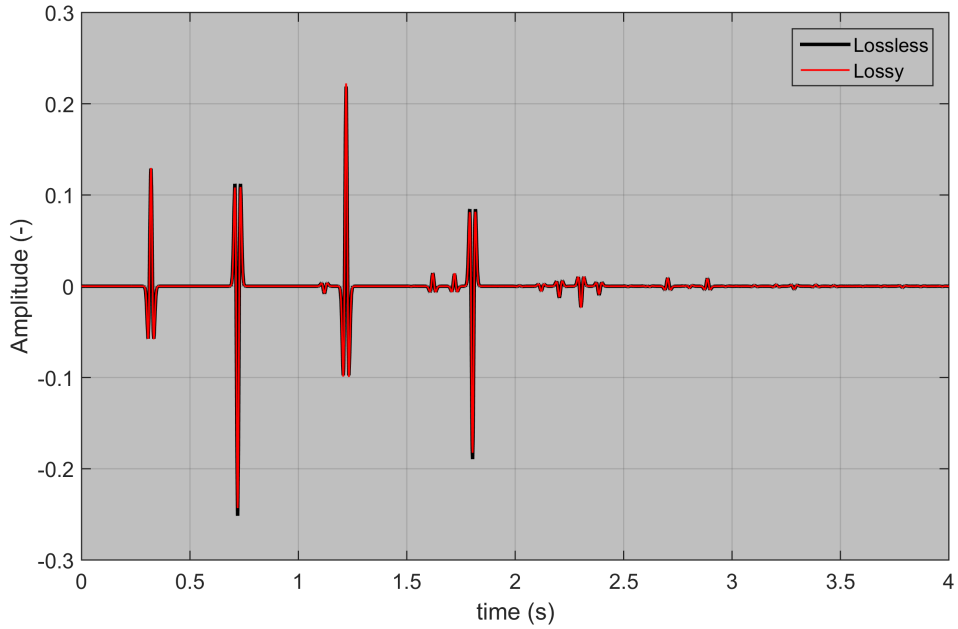

Figure 6-5: Lossless (black curve) and compensated lossy (red curve) reflection series for Model 2a. The x-axis represents time in seconds. The y-axis represents the amplitude. The intrinsic loss was modelled using De Hoop's model with two parameters (Model 2a). The compensation factor is $\zeta_{compensation} = 0.4$.

De Hoop's Model with One Parameter

This modelling is similar to the previous De Hoop's model with two parameters but, in this case, the losses were incorporated through the elastic modulus only. In the De Hoop's model with two parameters, the attenuation was incorporated via modulus and density while in the De Hoop's model with one parameter the attenuation was incorporated via modulus only. The lossy reflection response is different from Model 2a. Therefore, the compensation must be different as well. The medium properties are shown in table C-3 on page 95 (Model 2b). Model 2b is similar to the Model 2a but the attenuation α_H is different. Figure D-5 shows the lossless and the lossy reflection response for Model 2b. Figure D-6 illustrates the compensated lossy reflection series by parameter $\zeta_{compensation} = 0.5$. While the α_H is 200 percent larger in Model 2b compared to Model 2a, the compensation $Q_{temporal}$ is only 20 percent larger. Therefore, the attenuation mechanism plays an important role in the modelling.

6-2 Quantifying Attenuation using the Marchenko Equation

All artefacts in the Green's function (or in the focusing function or in the image) can be divided into two groups: [A] numerical artefacts and [B] artefacts caused by additional medium's assumptions.

While the solution of the Marchenko equation is exact, some small artefacts are present in the Green's functions — mainly because the single-sided inverse problem is extremely ill-posed and because of some numerical limitations. For example, we performed the discrete Fourier transform which is not absolutely perfect. These artefacts are very small and must be muted before applying Marchenko redatuming and imaging. Thorbecke et al. (2013) and Wapenaar et al. (2014b) further illustrated this when they applied the Marchenko equation to synthetic data where all the medium's assumptions have been fulfilled. These artefacts belong to the group [A], i.e. "numerical" artefacts.

On the other hand, if the medium doesn't fulfil all necessary assumptions, the solution of the Marchenko equation will produce some additional artefacts, different from the numerical ones. These additional artefacts contain some new information of the subsurface. These artefacts belong to the group [B]. There are several of the medium's properties which cause some artefacts in the Green's functions, focusing functions and image, such as: [1] anisotropy of the medium, [2] incorrectly scaled source signature, [3] incorrect velocity model, [4] incorrect compensation for transmission losses, [5] incorrect compensation for intrinsic losses (or, simply, lossy medium) etc. Therefore, by applying compensation for these properties, we will get a better seismic image and, what's even more attractive, we will obtain even more new information of the subsurface. For example, if our velocity model is incorrect and we observe some artefacts, we can change the velocity model by reducing the artefacts. As a result, a better image as well as a better velocity model will be obtained.

The artefacts behaviour in the second group depends on the input data. This idea uses a fundamental property that the solution of the Marchenko equation is exact. Therefore, the solution might be considered as a "skeleton". If our compensation for the medium's properties is incorrect, the solution will produce some artefacts from the second group. Also, these artefacts usually have a very specific behaviour: if the input data to the Marhcnko equation is over or under compensated, the resulting artefacts will have opposite behaviour. This phenomena is not new. In seismic interferometry Draganov et al. (2010) observed that artefacts change polarity if you under- or over- compensate for the intrinsic losses. Mildner et al. (2017) observed that artefacts change polarity if the source signature is under- or over-scaled. These artefacts have a common feature that they change polarity. But the energy of the artefacts, the number of the artefacts, their position on the time axis etc. strictly depend on the compensation parameters.

This thesis is focused on studying the intrinsic attenuation. The general idea of the proposing method to quantify the intrinsic attenuation is the following: [1] the artefacts must be recognized by applying different Q-compensation parameters to the reflection series, [2] by minimizing the artefacts, the true value of the medium's Q-factor can be found. In the case of the same attenuation for entire medium, the inverted Q-factor value is very accurate. In the case where different layers have different attenuation, the effective Q factor can be found or the time-dependent Q-factor can be found. A detailed approach as well as a number of examples will be further explained.

6-2-1 Behaviour of the Artefacts

Amplitude Damping Model

The main feature of Model 1 (the ideal model) is that, once we found the true attenuation of the medium and applied the compensation to the **lossy** reflection series, it coincided with the **lossless** reflection series. I used a focal point of 2000 meters (depth) to observe artefact behavior (i.e. the focal point is in the third layer). Several compensation parameters were applied to the lossy reflection series: $\zeta_{damping} = 0.2;\ 0.4;\ 0.6;\ 0.8;\ 0.9;\ 1.0$. Then, the upgoing Green's function $G^{-,+}$ was calculated for each compensated lossy reflection series. Figure E-1 illustrates the upgoing Green's function $G^{-,+}$ calculated using several compensated reflection series. Obviously, because the compensation parameters vary from 0.2 to 1.0, the resulting reflection series is under- and over- compensated for the attenuation. It can be seen by the amplitude changes in the primaries and multiples (Figure E-1). Two artefacts are present in $G^{-,+}$ on Figure E-1 at times 1.25 and 2 seconds. By studying the Figure E-1 it can be seen that the artefacts change their polarity. This feature further explored on Figure 6-6 where the $G^{-,+}$ zoomed in to 1.16-1.34 seconds. The values of compensation parameter $\zeta_{compensation} = 0.2;\ 0.4;\ 0.6$ cause the negative polarity artefact. The values of compensation parameter $\zeta_{compensation} = 0.9;\ 1.0$ cause the positive polarity artefact. The value of compensation parameter $\zeta_{compensation} = 0.8$ gives no artefact! It means that the compensation parameter coincides with the damping parameter. Therefore, true attenuation is found.

In order to derive an expression which is able to recognize artefacts, I first calculated several upgoing Green's functions $G_i^{-,+}$. Index i means that $G_i^{-,+}$ was calculated using the compensated lossy reflection response with different compensation parameter $\zeta^i_{compensation}$. In this example, $i = 1;\ 2;\ 3;\ 4;\ 5;\ 6$; and corresponds to $\zeta_{compensation} = 0.6;\ 0.7;\ 0.75;\ 0.8;\ 0.85;\ 0.9$. The artefacts change polarity, therefore, the artefacts can be found by calculating the function $\mathcal{T}(\mathbf{x}, t)$:

$$\mathcal{T}(\mathbf{x}, t) = \left[\left| \sum_i G_i^{-,+}(\mathbf{x}, t) \right| - \sum_i \left| G_i^{-,+}(\mathbf{x}, t) \right| \right] \cdot e^{bt} \tag{6-10}$$

The exponent e^{bt} was added to this expression to increase the energy of the artefacts at longer times. Parameter b is a free parameter and can be set to 1, or another value. It depends on whether we want to have all artefacts be equal amplitudes or not. It is suggested to choose the value of b in such a way that all artefacts have the same amplitudes. If it is not possible, use time-dependent normalization. Figure 6-7 illustrates the function $\mathcal{T}(\mathbf{x}, t)$ calculated for Model 1. Three artefacts are clearly visible at 1.25, 2 and 2.75 seconds. Figure E-2 shows Figure 6-7 zoomed in to 1-4.5 seconds and between 0 and $15 \cdot 10^{-3}$ amplitudes. Five artefacts can be seen at 1.25, 2; 2.75, 3.5 and 4.25 seconds. The time difference between the artefacts is 0.75 seconds. This is the double the travel time of the wave in the second layer. Indeed, 750 meters $\div$ 2000 m/s = 0.375 seconds $\times$ 2 = 0.75 seconds. Therefore, it can be concluded that these artefacts are caused by the second layer.

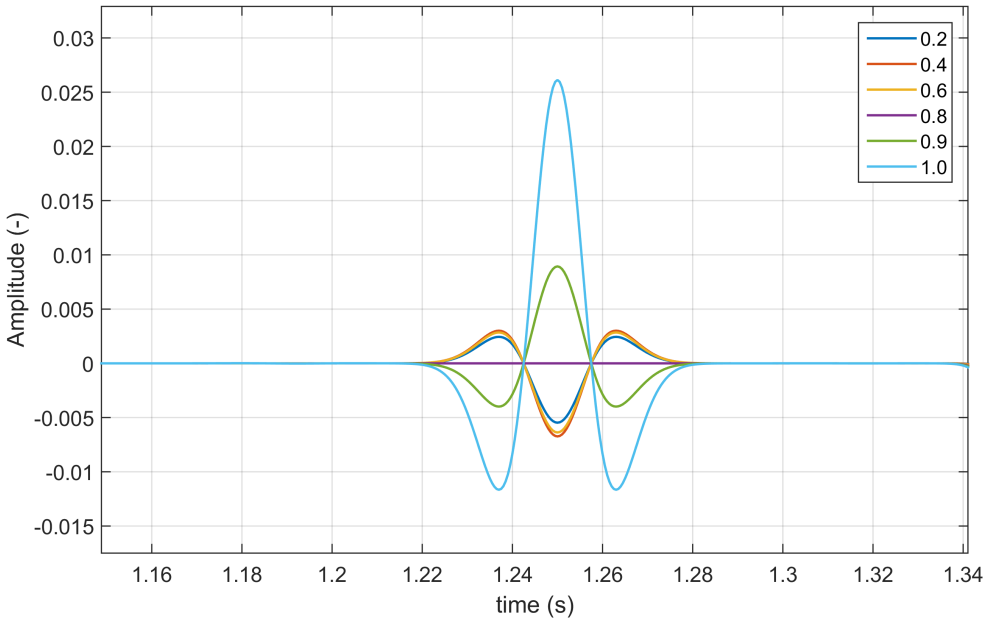

Figure 6-6: Upgoing Green's function $G^{-,+}$ zoomed in to 1.15-1.34 seconds. The focal point is 2000 m depth. Different colors correspond to different compensation parameters $\zeta_{compensation}$ = 0.2, 0.4, 0.6, 0.8, 0.9, 1.0. The intrinsic loss was modelled as an amplitude damping (Model 1). Compensation parameter $\zeta_{compensation}$ = 0.8 (purple curve) shows no artefact which corresponds to the true compensation.

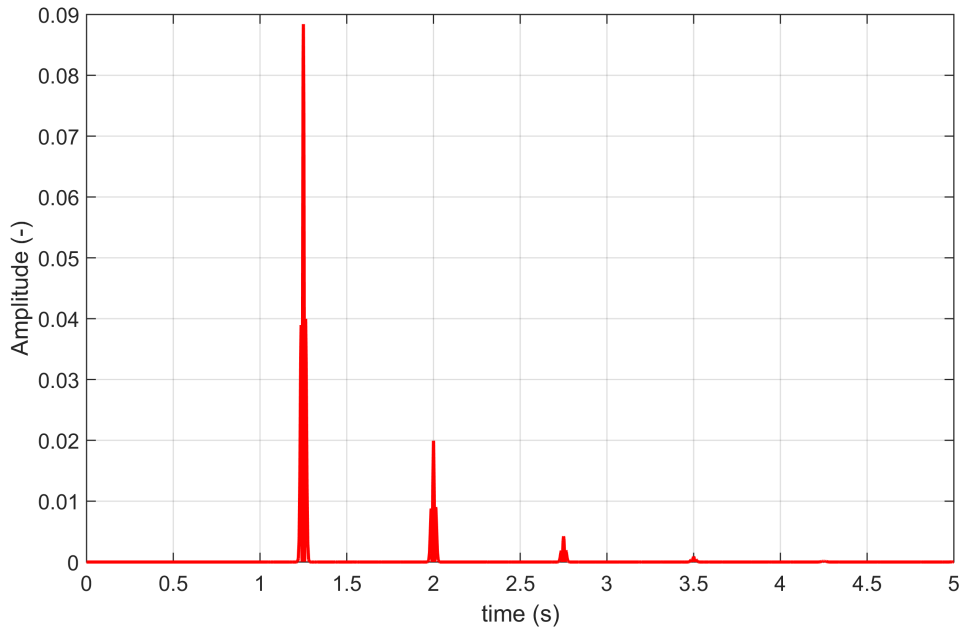

Figure 6-7: The function $\mathcal{T}(\mathbf{x}, t)$. Three artefacts are clearly visible at 1.25, 2, 2.75 seconds. The intrinsic loss was modelled as an amplitude damping (Model 1).

6-2-2 Analysis of Artefacts in the Frequency Domain

Artefact behavior in the frequency domain was examined, firstly, by defining the time intervals, t_l in $\mathcal{T}(\mathbf{x}, t)$, when the artefacts occur. Subscript l corresponds to a particular artefact. For example, there are five artefacts present in $\mathcal{T}(\mathbf{x}, t)$, therefore, there are five intervals in t_l. Next, I define the function $\mathcal{T}_G^i(\mathbf{x}, t_l)$:

$$\mathcal{T}_G^i(\mathbf{x}, t_l) = G_i^{-,+}(\mathbf{x}, t_l) \tag{6-11}$$

This function $\mathcal{T}_G^i(\mathbf{x}, t)$ is non zero only at time intervals where the artefacts are present. Superscript i corresponds to different compensation parameters applied to the lossy reflection series. Figure E-3 illustrates the function $\mathcal{T}_G^i(\mathbf{x}, t_l)$ calculated for different $\zeta_{compensation}$. The polarity of the events on Figure E-3 (a) and (b) is opposite to the polarity on Figure E-3 (c). Then, I transformed the function $\mathcal{T}_G^i(\mathbf{x}, t_l)$ into the frequency domain:

$$\widehat{\mathcal{T}}_G^i(\mathbf{x}, \omega) = FT\left[\mathcal{T}_G^i(\mathbf{x}, t_l)\right] \tag{6-12}$$

Figure 6-8 (2D plot) shows the function $\widehat{\mathcal{T}}_G^i(\mathbf{x}, \omega)$. Figure E-4 (3D plot) shows the function $\widehat{\mathcal{T}}_G^i(\mathbf{x}, \omega)$. The minimum of $\widehat{\mathcal{T}}_G^i(\mathbf{x}, \omega)$ occurs when the compensation parameter is $\zeta_{compensation} = 0.8$. This value of $\zeta_{compensation}$ is indeed the true $\zeta_{damping}$ which was applied to the wave field. Figure E-5 is the same as Figure E-4 but the compensation parameter $\zeta_{compensation}$ varies from 0.6 to 0.9. The minimum $\zeta_{compensation} = 0.8$ is, in fact, very strong.

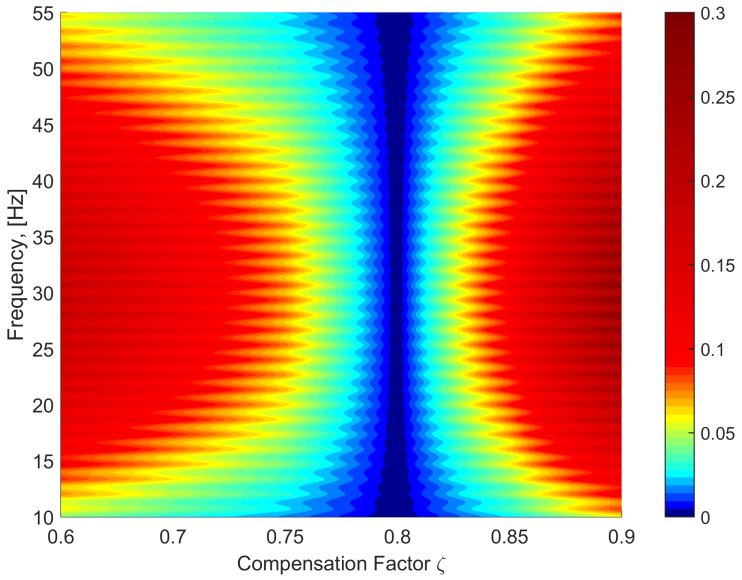

Figure 6-8: Function $\widehat{\mathcal{T}}_G^i(\mathbf{x}, \omega)$. This figure is similar to Figure E-5 but instead of a 3D plot this figure is a 2D plot. $\zeta_{compensation} = 0.6$; 0.7; 0.75; 0.8; 0.85; 0.9 and the frequency. The color denotes the amplitude. The true compensation parameter is $\zeta_{compensation} = 0.8$ which corresponds to the minimum of $\widehat{\mathcal{T}}_G^i(\mathbf{x}, \omega)$ (blue).

6-2-3 Analysis of Artefacts using the Wavelet Transform

The main difference between the continuous 1D wavelet transform and the Fourier transform, which is important in this study, is that the wavelet transform produces a time and frequency localization. In other words, we can perform a time-frequency analysis of a signal. Different wavelets are possible, therefore, about ten wavelets were applied, including: Haar wavelet, Meyer wavelet, Shannon wavelet, Gaussian wavelet, Complex Gaussian wavelet etc. Morlet wavelet showed the best capabilities to study the artefacts' behaviour for different $\zeta_{compensation}$. Theory of the continuous wavelet transform is beyond this study and can be found in Daubechies (1992); Mallat (2008) and Teolis (2012). The continuous wavelet transform of function $f(t)$ at any scale a and position b is (Mallat, 2008):

$$\boldsymbol{W}f(b,a) = \int_{-\infty}^{+\infty} f(t)\frac{1}{\sqrt{a}}\,\phi\left(\frac{t-b}{a}\right)dt \tag{6-13}$$

where ϕ is a wavelet, a is a scale parameter and b defines the shift. Therefore, a time-scale image (b,a) can be created. First, I applied the continuous 1D wavelet transform using the Morlet wavelet to the function $\mathcal{T}_G^i(\mathbf{x},t_l)$ with scales a varying from 20 to 80. The analysis of the wavelet transform was performed using a scaleogram — as shown in Figure E-4 — the wavelet transform of $\mathcal{T}_G^i(\mathbf{x},t_l)$. The x-axis represents time, the y-axis represents scale a and z-axis represents the coefficient value. Morlet wavelet is complex valued, therefore, I calculated the absolute value of the complex function. The coefficient values on Figure E-4 (a) and (b) are similar and correspond to strong artefacts. The coefficient values on Figure E-4 (c) are not as strong as on Figure E-4 (a) and (b) which means that the compensation parameter $\zeta_{compensation} = 0.75$ is closer to the true value. Finally, Figure E-4 (c) shows no artefacts which means that the compensation parameter $\zeta_{compensation} = 0.8$ is correct. This approach will be very important later for attenuation estimation of more complex models and for constructing an effective Q-factor compensation and a time-dependent Q-factor compensation. $\zeta_{compensation} = 0.8$ is the correct value, because the amplitude is zero (Figure 6-9).

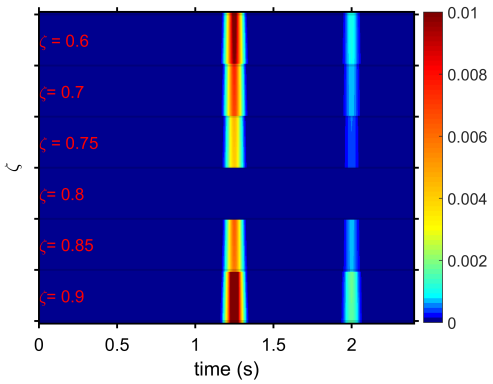

Figure 6-9: The continuous 1D wavelet transform of the function $\mathcal{T}_G^i(\mathbf{x},t_l)$ using the Morlet wavelet. The x-axis represents time in seconds. The y-axis represents scale a. The y-axis is divided into 6 horizontal bands. Each horizontal band corresponds to a different $\zeta_{compensation}$. Within each horizontal band, scales a = 70-80 are shown. The color represents the coefficient value.

De Hoop's Model with Two Parameters

Artefact behavior was examined by using De Hoop's lossy model with two parameters (Model 2a). The work flow is similar to the previous sub-section where the ideal model was analysed. I focused the wave field at 2000 meters (depth), i.e. the focal point is in the fourth layer. Therefore, there are multiples in the second and in the third layers which may cause some artefacts in the upgoing Green's function $G^{-,+}$. Several compensation parameters were applied to the lossy reflection series: $\zeta_{damping} = 0.1, 0.2, 0.3, 0.4, 0.5, 0.6$. Figure 6-10 illustrates the function $\mathcal{T}(\mathbf{x}, t)$ which consists of artefacts only in the upgoing Green's function $G^{-,+}$. These artefacts were calculated by using Eq. (6-10). Indeed, two layers cause many more artefacts compared to the previous ideal model. Then, I calculated the function $\mathcal{T}_G^i(\mathbf{x}, t_l)$. Next, the function $\widehat{\mathcal{T}}_G^i(\mathbf{x}, \omega)$ was calculated by using the Eq. (6-12). The next step was the continuous wavelet transform calculation of function $\mathcal{T}_G^i(\mathbf{x}, t_l)$.

Figure E-7 illustrates the function $\widehat{\mathcal{T}}(\mathbf{x}, t)$ calculated for different compensation parameters $\zeta_{compensation} = 0.1, 0.2, 0.3, 0.4, 0.5, 0.6$. Figure E-9 shows the function $\widehat{\mathcal{T}}(\mathbf{x}, t)$ as a 2D plot. Figure E-10 is the continuous 1D wavelet transform of the function $\mathcal{T}_G^i(\mathbf{x}, t_l)$ using the Morlet wavelet for different $\zeta_{compensation}$. The minimum of $\mathcal{T}(\mathbf{x}, t)$ corresponds to the $\zeta_{compensation} = 0.4$ but this minimum is not perfect. Therefore, the exact parameter $\zeta_{compensation}$ can be inverted by solving the non-linear inverse problem. It can be done in several ways. The first way is by minimizing the function $\mathcal{T}_G^i(\mathbf{x}, t_l)$:

$$\|\mathcal{T}_G^i(\mathbf{x}, t_l)\|_2 \to 0 \tag{6-14}$$

$\|\cdot\|_2$ denotes the L^2-norm. The second way is by minimizing the function $\widehat{\mathcal{T}}_G^i(\mathbf{x}, \omega)$ in the frequency domain:

$$\|\widehat{\mathcal{T}}_G^i(\mathbf{x}, \omega)\|_2 \to 0 \tag{6-15}$$

The third way is by minimizing the coefficient values of the wavelet transform $\boldsymbol{W}\left[\mathcal{T}_G^i(\mathbf{x}, t_l)\right]$:

$$\|\boldsymbol{W}\left[\mathcal{T}_G^i(\mathbf{x}, t_l)\right]\|_2 \to 0 \tag{6-16}$$

As a result of the first method, the value of $\zeta_{compensation} = 0.4352$ was obtained. Indeed, $\zeta_{compensation} = 0.4352$ provides much better results which can be seen in the frequency domain (Figure E-8 and Figure 6-11) and in the scaleogram (Figure E-11). The compensated lossy reflection series with $\zeta_{compensation} = 0.4352$ is shown in Figure E-12.

De Hoop's Model with One Parameter

The same inversion method was performed by using De Hoop's lossy model with one parameter (Model 2b). The results are similar to the Model 2a.

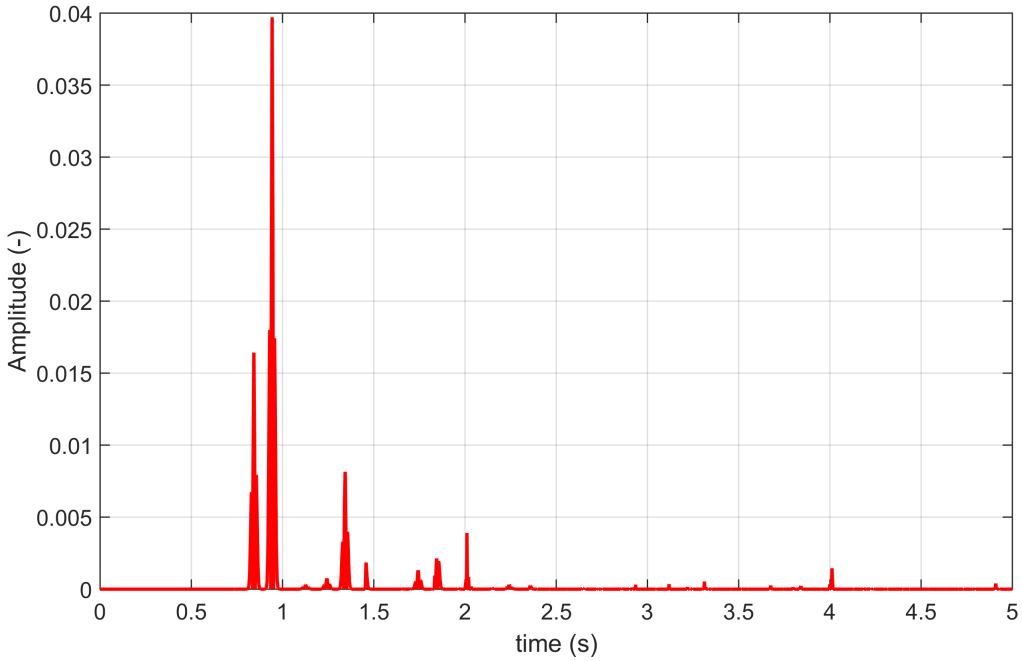

Figure 6-10: The function $\mathcal{T}(\mathbf{x}, t)$. Several artefacts are clearly visible. The intrinsic loss was modelled using De Hoop's Model with Two Parameters (Model 2a).

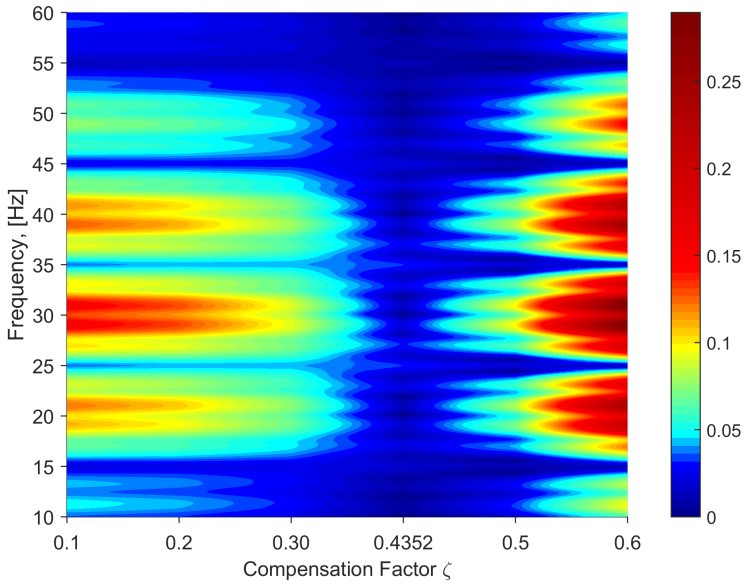

Figure 6-11: Function $\mathcal{T}_G^i(\mathbf{x}, t_l)$. This figure is similar to Figure E-8 but instead of a 3D plot this figure is a 2D plot. The x-axis represents the compensation parameter $\zeta_{compensation}$ = 0.1, 0.2, 0.3, 0.4352, 0.5, 0.6. The y-axis represents the frequency. The color denotes the amplitude. The true compensation parameter is $\zeta_{compensation} = 0.4352$, which corresponds to the minimum of $\widehat{\mathcal{T}}_G^i(\mathbf{x}, \omega)$ (blue). The intrinsic loss was modelled using De Hoop's Model with Two Parameters (Model 2a).

6-2-4 Artefact Removal Method to Quantify Attenuation

The general approach is as follows:

[1] Focus the wave field in the subsurface, using the Marchenko equation. Identify a set of Q-factors $\{Q_i\}$ to compensate for the attenuation in the interval between the acquisition surface and the focal point. This set of Q-values must be broad and include the extreme minimum and maximum values (for example, from 5 to 1000). Then, calculate $\zeta^i_{compensation}$ from $\{Q_i\}$. Next, calculate a set of compensated lossy reflection series R_i by applying $\zeta^i_{compensation}$ to the lossy reflection series.

[2] Calculate the function $\mathcal{T}(\mathbf{x},t)$ using Eq. (6-10). Identify the time intervals, t_l in $\mathcal{T}(\mathbf{x},t)$, where the artefacts occur. Calculate the function $\mathcal{T}^i_G(\mathbf{x},t_l)$ using Eq. (6-11) and choose the intervals where there is no overlap with other events.

[3] Transform the function $\mathcal{T}^i_G(\mathbf{x},t_l)$ into the frequency domain: $\widehat{\mathcal{T}}^i_G(\mathbf{x},\omega) = FT\left[\mathcal{T}^i_G(\mathbf{x},t_l)\right]$. Apply the continuous wavelet transform, using the Morlet wavelet to the function $\mathcal{T}^i_G(\mathbf{x},t_l)$ and create a scaleogram with several horizontal bands, which correspond to different $\zeta^i_{compensation}$.

[4] Analyze the artefacts' behavior in the frequency domain and in a scaleogram. If the minimum doesn't exist, repeat step [1] and choose another set of $\{Q_i\}$. The minimum may be absent if there is no effective Q-factor for a given interval between the acquisition surface and the focal point. In this case, another focal point must be chosen.

[5] Invert for the effective compensation parameter $\zeta_{compensation}$ which corresponds to the minimum in the functions: [a] $\mathcal{T}^i_G(\mathbf{x},t_l)$, [b] $\widehat{\mathcal{T}}^i_G(\mathbf{x},\omega)$, [c] $\boldsymbol{W}\left[\mathcal{T}^i_G(\mathbf{x},t_l)\right]$.

These steps, [1]-[5], will give you an effective temporal Q-factor for a given interval between the acquisition surface and the focal point, only the Marchenko equation is used in this method. This method works very well if an effective temporal Q-factor exists in that interval. The results are given in sections 6-3-1 - 6-3-3 for a constant Q-factor model and for De Hoop's Model with Two Parameters. The analysis of this method, when there are different layers and hence different attenuation, is shown in the next sections.

The general approach is to focus at several focal points in the medium and apply the method to invert for the attenuation. This will give you the quantitative information about the attenuation in the subsurface. You will find the intervals where the attenuation is quite similar between the layers and where the attenuation is very strong. Instead of minimizing the artefacts in the upgoing Green's function, it can be done by minimizing the artefacts in the redatumed reflection series. Moreover, this method is more stable if applied to the redatumed reflection series (mainly because there are more artefacts).

Nota Bene

In this modeling, it is assumed that surface-related (i.e. free-surface) multiples have been removed. Therefore, it might be reasonable to assume a zero or very low attenuation in the first layer. In this case, this method also would work with some modifications. First, the compensation for the losses must start not from zero time (like in this work) but from the time of the first reflection from the bottom of the first layer. Also, the behaviour of the artefacts will be slightly different; Therefore, this method can be applied to minimize the artefacts in the upgoing focusing function of the first kind and in the downgoing focusing function of the second kind. Furthermore, even more artefacts are present in the redatumed reflection series. In other words, I have tested this method by minimizing the artefacts in the the redatumed reflection series and in the f_1^- for a few models. The results are very similar to when I minimized the artefacts in the upgoing Green's function. The only difference is that the artefacts in f_1^- start to appear if the focal point is below the third layer (the first layer without free-surface multiples and the next two layers are with all kinds of multiples). Similarly, in the redatumed reflection series and in the f_1^-, the different artefacts are related to different layers; Therefore, the effective Q-factor can be found. Also, if the effective Q-factor compensation for a given interval doesn't exist, it can be recognized because not all the artefacts can be removed.

6-2-5 Constant-Q, Effective-Q and Time-Dependent-Q Compensation Factors

If all the layers have the same attenuation, a constant-Q factor can be found by using the Artefact Removal Method. If different layers have different attenuation but the difference in attenuation is small (i.e. 10-50 %), an effective Q-factor can be found. In this case, not all the artefacts can be removed but the minimum can at least be found. If there is a layer with a very high attenuation such that the effective Q-factor doesn't exist, it can be recognized by applying the Artefact Removal Method to the redatumed reflection series (it is shown in section 6-5). In this case, the artefacts can not be removed and they are strong for any applied compensation factors. This artefact model is explained in detail below.

Effective Q-factor

In order to test this method for the case where one layer has a strong attenuation, a more complex model was created. It has five layers, each with a different velocity and density. Each layer has a different velocity and density. This model is the same as Model 2a but the third layer has a different attenuation: $\alpha_H = 5.25$. The medium properties are shown in table C-4 on page 96 (Model 2c). Figure E-13 shows the two reflection series. The first reflection series was calculated for lossless media (black curve). The second reflection series was calculated for lossy media. The intrinsic loss was modelled using De Hoop's model with two parameters (Model 2c). I focused the wave field at different depth levels because we measured attenuation in the interval between the acquisition surface and the focusing depth. By doing this step-by-step approach we can see how the attenuation changes.

When the focusing depth is 1300 meters, the attenuation for the first two layers can be found by minimizing the artefacts. However, once the focus goes below the high attenuation

layer, not all the artefacts in the upgoing Green's function can be removed, by applying a compensation to the reflection series.

The following are some examples of when the focal point is 2000 meters. Figure E-14 illustrates the function $\widehat{\mathcal{T}}(\mathbf{x},t)$ calculated for different compensation parameters $\zeta_{compensation}$ = 0.1, 0.2, 0.3, 0.4, 0.45, 0.55. Figure 6-12 shows the function $\widehat{\mathcal{T}}(\mathbf{x},t)$ as a 2D plot. According to Figure E-13 and Figure 6-12 the range of $\zeta_{compensation}$ = 0.4- 0.45 gives the minimum in $\widehat{\mathcal{T}}(\mathbf{x},t)$. Therefore, we can't invert for the exact compensation parameter. This is caused by the third layer which has a stronger attenuation than the other layers. Figure E-15 is the continuous 1D wavelet transform of the function $\mathcal{T}_G^i(\mathbf{x},t_l)$ using the Morlet wavelet for different $\zeta_{compensation}$. The minimum of $\mathcal{T}(\mathbf{x},t)$ corresponds to the $\zeta_{compensation}$ = 0.42 but this minimum is not perfect. Artefacts are still present. Furthermore, in Figure E-15 the artefacts which correspond to $\zeta_{compensation}$ = 0.39 and $\zeta_{compensation}$ = 0.45 have the opposite behaviour. It means that the range of $\zeta_{compensation}$ = 0.375-0.39 (where the first artefact is closer to zero in Figure E-15) corresponds to the correct compensation for the losses in the first layer. While the value of $\zeta_{compensation}$ = 0.45 (where the second artefact is closer to zero in Figure E-15) corresponds to the correct compensation for the losses in the second layer. This means that if I: [1] apply the value of $\zeta_{compensation}$ = 0.45 to the lossy reflection series, then [2] the amplitude of reflection from the bottom of the second layer of this reflection series (compensated lossy) will coincide with the amplitude of the lossless reflection series. Unfortunately, the artefacts related to the layer with a strong attenuation cannot be recognized. This problem can be solved by applying this method to the redatumed reflection series (section 6-5). The artefacts are strong for any compensation factor which are shown in Figures E-15 and E-14. In general, it is difficult to determine which artefact corresponds to which layer because the model is unknown. Therefore, the parameter $\zeta_{compensation}$ can be inverted by minimizing the artefacts and the solution will give us only an effective temporal Q-factor of the medium between 0-2000 meters. But I can focus the wave field in the third layer, for example at a depth of 1200 meters to calculate the attenuation of the medium above that focal depth.

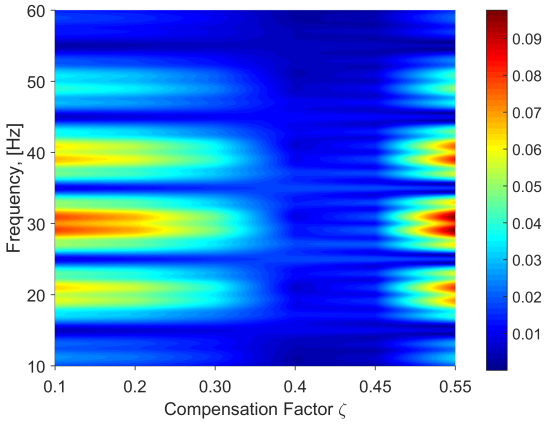

Figure 6-12: Function $\widehat{\mathcal{T}}_G^i(\mathbf{x},\omega)$ for Model 2c. The horizontal plane is the compensation parameter $\zeta_{compensation}$ = 0.1, 0.2, 0.3, 0.4, 0.45, 0.55 and the frequency. The vertical axis corresponds to the amplitude. The range of $\zeta_{compensation} = 0.4 - 0.45$ corresponds to to the minimum of $\widehat{\mathcal{T}}_G^i(\mathbf{x},\omega)$.

Time-Dependent-Q Compensation

Time-Dependent-Q compensation might be a very attractive tool to compensate for the losses in a very simple way — by applying the time-dependent compensation to the lossy reflection series. In order to test this, I used the Model 2c (table C-4 on page 96). (Nota Bene: The model seems to be quite simple, therefore, the time-dependent compensation might give a very nice result). First, I calculated the lossless and lossy reflection series for Model 2c. Then, I divided the whole lossy reflection series into 20 segments — each corresponding to one particular event, which all include a primary reflection and/or multiples (until it's not visible). After that, I found the compensation parameter for each segment. By applying this compensation parameter to the lossy reflection response (i.e. to one particular segment or a time interval) I got the lossless one. The accuracy of this time-dependent compensation is roughly 10^{-3} (i.e. the difference between the compensated lossy and lossless reflection series is less than $1 * 10^{-3}$ amplitudes at any time). Next, I focused the wave field at a depth of 2000 meters depth using the compensated lossy reflection series. The amplitudes of the up- and down- going Green's functions were calculated by using the compensated lossy reflection series. They are very similar to the up- and down- going Green's functions, which were calculated by using the lossless reflection response (the difference between the compensated lossy and lossless versions are less than 10^{-3}). But there are still artefacts present in the upgoing Green's function. Furthermore, the artefacts are present at different locations. The main problem is that the Marchenko equation is highly sensitive to time-dependent compensation. For example, if the compensated lossy reflection series coincides with the lossless reflection series everywhere except one event, the approach will break down. This event might correspond to the third order multiple, i.e. the difference between the compensated lossy and lossy reflection response is $5 * 10^{-2}$, which is a very small difference. It will, therefore, produce noticeable artefacts in the upgoing Green's function. So, the idea to invert for the time-dependent compensation factor breaks down because the criterion is not stable. Moreover, the inversion for the minimizing the artefacts is non-linear. Consequently, it is impossible to invert for all 20 compensation parameters, which all correspond to their own particular time interval. Additionally, the model of the subsurface is unknown. So, that makes it difficult to model all possible multiples within different layers and their subsequent interactions and apply a correct compensation parameter. Overlapping events have the same issue. In conclusion, the time-dependent approach is not going to work even for a quite simple model.

6-3 Marchenko Redatuming in Viscoelastic Media

As was shown in chapter 2, the Marchenko equation can be used to redatum the receivers and the sources to any depth level $\mathbb{D}_i$ in the subsurface. The main feature of Marchenko redatuming is that it takes into account all internal multiple reflections. It is a two step process and a detailed explanation can be found in Wapenaar et al. (2014b). The upgoing and downgoing Green's functions are related via Eq. (3-59):

$$G^{-,+}(\mathbf{x}_i, \mathbf{x}', t) = \int_{\partial\mathbb{D}_i} d\mathbf{x} \int_{-\infty}^{\infty} R^{\cup}(\mathbf{x}_i, \mathbf{x}, \tau) G^{+,+}(\mathbf{x}, \mathbf{x}', t-\tau) d\tau, \tag{6-17}$$

where $R(\mathbf{x}_i, \mathbf{x}, \tau)$ is the reflection response of the medium below depth level $\mathbb{D}_i$. This reflection response is defined in a medium which is identical to the actual medium below $\mathbb{D}_i$ and is reflection-free above this depth level. In the 1D case, equation (6-17) can be solved via deconvolution in the frequency domain (Vasconcelos, 2007):

$$R^{\cup} = \frac{G^{-,+}}{G^{+,+}} = \frac{G^{-,+}\, G^{+,+*}}{|G^{+,+}|^2 + E} \tag{6-18}$$

where E is a parameter that accounts for stabilization and $R^{\cup}$ is the redatumed reflection response. I found that the value of $E = 10^{-4}$ provides quite an accurate result for a given wave field. Several models were used to test the Marchenko redatuming. In 1D, the general approach is the following: [1] Focus in the subsurface and calculate the upgoing and downgoing Green's functions using the Marchenko equation; [2] calculate the redatumed reflection response $R^{\cup}$ by using Eq. (6-18).

Several figures are shown below. In each figure you will find three reflection responses: black, green, dashed red. The black curves show the 1D lossless reflection responses at the surface. The green curves show the redatumed reflection response which was calculated via (6-18) using the $G^{-,+}$ and $G^{+,+}$ for lossless medium. Dashed red curve shows the redatumed reflection response which was calculated via (6-18) using the $G^{\pm,+}$ for lossy or compensated lossy medium.

6-3-1 Marchenko Redatuming for the Amplitude Damping Model

This is a perfect model. The main feature is that once we found the attenuation of the subsurface, the compensated lossy reflection series coincides with the lossless one. Its medium properties are shown in table C-1 on page 95 (Model 1). Figure 6-13 shows the reflection response at the surface (black curve) and two redatumed reflection responses that were shifted to the location of the focal point (green and dashed red curves, respectively). The green curve is the redatumed response for the medium without attenuation. The dashed red curve is the redatumed response for the medium with attenuation. The dashed red curve shows very low amplitudes and artefacts. The artefacts are shown on Figure 6-14 which is the same as Figure 6-13 but zoomed in to 2-4.5 seconds and -0.02-0.04 amplitudes. But once the attenuation of the medium is found via the Green's Function Artefact Removal Method, the lossy reflection series can be compensated for the losses. Figure 6-15 shows the redatumed

reflection response which was calculated via Eq. (6-18) using $G^{\pm,+}$ for compensated lossy medium. No artefacts are present on the red curve.

6-3-2 Marchenko Redatuming for De Hoop's Model Two Parameters

De Hoop's Model is explained in chapter 3. Because the models with one or two parameters are similar, only the De Hoop's Model with two parameters was considered. The medium properties are shown in table C-2 on page 95 (Model 2a). In this model, the losses were incorporated through two parameters: the moduli and density of the rock. As it was mentioned before, a simple exponent compensation factor won't completely compensate for attenuation. Therefore, some artefacts might be present in the redatumed reflection response. Figure F-1 shows three reflection series (the same as the previous model). The dashed red curve shows very low amplitudes. Figure F-2 is the same as Figure F-1 but zoomed in to 1.5-3.2 seconds and -0.04-0.06 amplitudes. The artefacts are shown by blue arrows on Figure F-2. Figure F-3 shows the redatumed reflection response which was calculated via Eq. (6-18) using $G^{\pm,+}$ for compensated lossy medium. The compensation was found via Artefact Removal Method. Because the compensation is not perfect, some artefacts are present but their amplitudes are very small (lower than $8 \cdot 10^{-4}$).

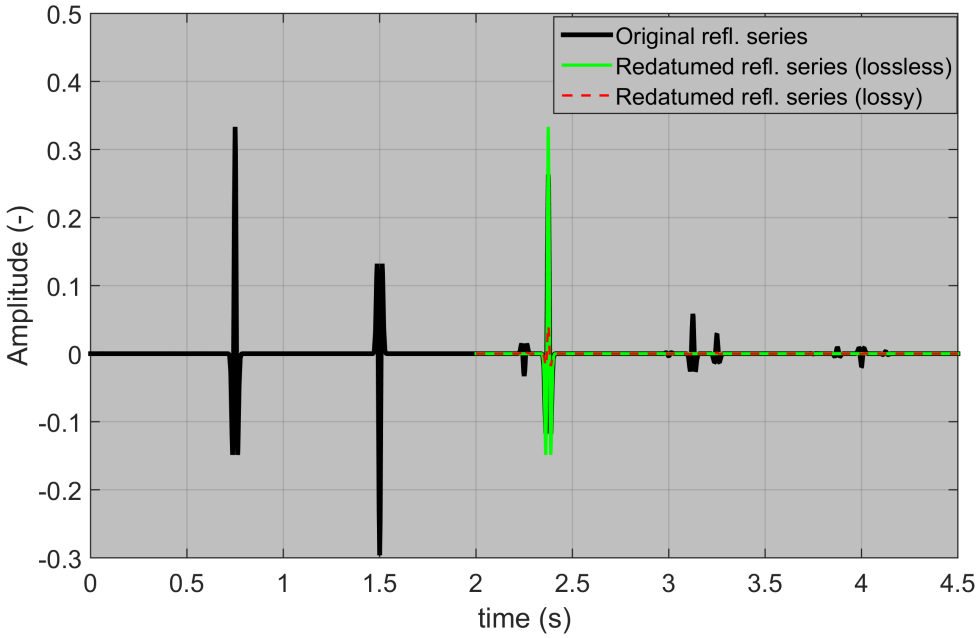

Figure 6-13: Reflection response (black), redatumed reflection response using $G^{\pm,+}$ for lossless medium (green) and the redatumed reflection response using $G^{\pm,+}$ for lossy medium. Losses were incorporated as Amplitude Damping (Model 1). The black curve coincides with the green curve at time ≈2.4 sec.

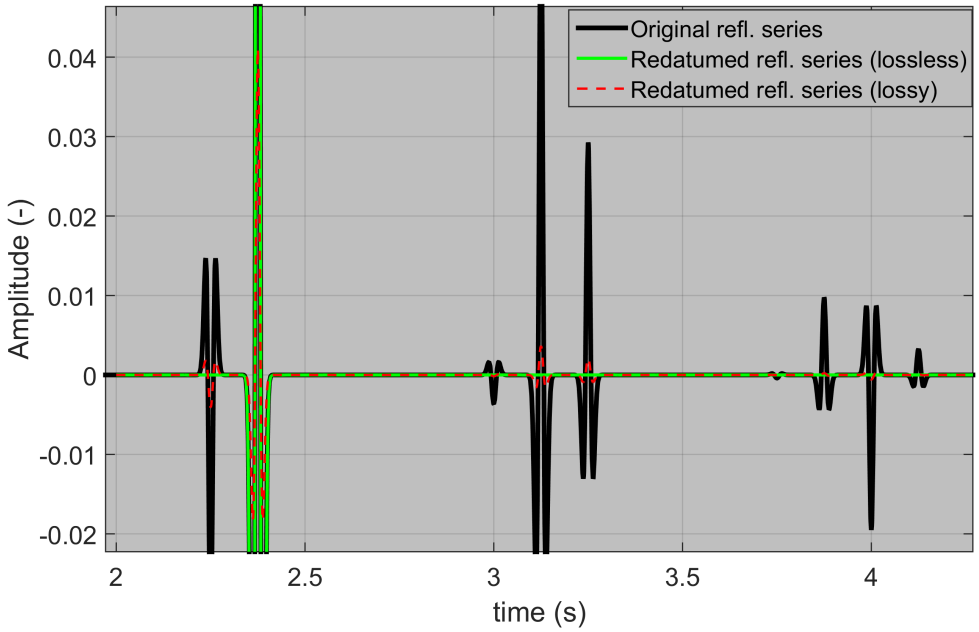

Figure 6-14: This is the same figure as Figure 6-14 but zoomed in to 2-4.5 seconds and -0.02-0.04 amplitudes. Losses were incorporated as the Amplitude Damping (Model 1). The black curve coincides with the green curve at time ≈2.4 sec.

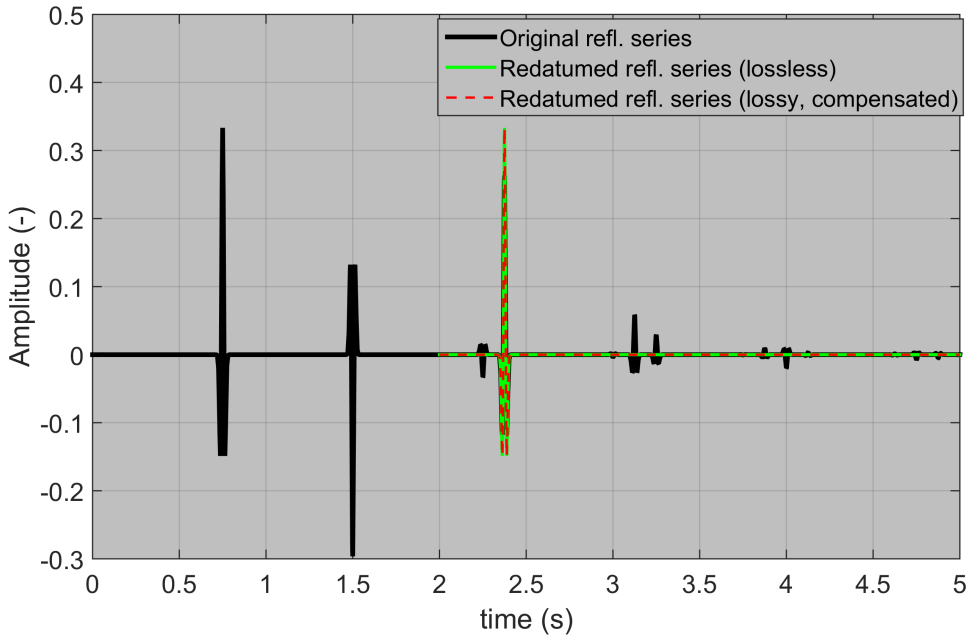

Figure 6-15: Black and green curves are the same as in Figure 6-13. The dashed red curve is the redatumed reflection response which was calculated using $G^{\pm,+}$ for compensated lossy medium. The black curve coincides with the green curve at time ≈2.4 sec.

6-4 Conclusion

The Artefact Removal Method works very well for the medium where the losses can be compensated via an effective temporal Q-factor. It means that this approach works for the medium where all layers have similar attenuation or the difference in attenuation between layers is (approximately) less than 10-50%. If there is a layer/layers with very strong attenuation, the effective temporal Q-factor can be found for an interval between the acquisition surface and the layer/layers with very strong attenuation. The time-dependent compensation factor doesn't seem to work even for a simple medium. In general, it cannot be found because of too many unknown parameters for compensation are needed. In fact, there are all kind of multiples between several layers for which the correct compensation can be found only through modeling. Marchenko redatuming for lossy medium works very well for the medium where the losses can be compensated via an effective temporal Q-factor.

Chapter 7

Seismic Upscaling

In this chapter, the theory and practical results of seismic upscaling method will be shown, which include: [7-1] the connection between the different types of Lippmann-Schwinger equations, [7-2] Rock Physics Modeling. Section [7-1] provides the mathematical background of this work. The main idea is that the wave propagation and scattering at macro- and micro-scales are governed by similar equations. Therefore, upscaling can be done because seismic imaging and rock physics are linked through viscoelasticity of the medium. In section [7-2], the final, the most complex model (Model 3a-b) is illustrated. This model is governed by three components — rock physics, viscoelasticity and imaging. The first component is the calculation of the viscoelastic modulus of a reservoir layer using the methods described in Chapters 4 and 5. Then the viscoelastic modulus was used to construct the image and test the Q-estimation method. As a result, the rock properties' changes in the reservoir layer might be seen on the image. While this is done in 1D, not all the benefits can be shown. But this idea could be extended to 2D and 3D media where all the advantages are visible. Also, more complex rock's models could be very beneficial to test different imaging technologies. For example, this model could have a strong attenuation and velocity dispersion which is common for reservoirs.

7-1 Connections Between the Different Types of Lippmann-Schwinger Equations

This section is mainly inspired by the papers de Hoop and de Hoop (2000); Wapenaar (2007); Wapenaar and Douma (2012) and Broggini and Snieder (2012). In the first three papers, the Unified Wave Equation was explored. It makes it possible to unify several partial differential equations (namely the acoustic wave equation, elastodynamic wave equation, Schrödinger equation, electromagnetic wave equation and piezoelectric wave equation) into one general equation with different coefficients. In the fourth paper, Broggini and Snieder (2012) explored the connection of different scattering integral equations.

It can be shown that the Lippmann-Schwinger equations, which describes wave field scattering at macro- and micro- scales, are very similar. These mathematical observations might give some insight into new ideas regarding micro- and macro- scale wave propagation. Let us suppose that function Ψ of a given physical system is:

$$L\Psi = f \tag{7-1}$$

This is a more generalized form of Eq. (2-1). L is a linear differential operator acting on distributions over a Sobolev space $\Omega \subset \mathcal{W}^0$. Function Ψ can have any form. It might be the Hamiltonian of a given physical system H (Landau and Lifshitz, 1958; Rodberg and Thaler, 1967), a wave field u (Colton and Kress, 2012), etc. Operator L also can have any form as discussed in Chapter 2 — a Sturm-Liouville operator, the wave operator, etc. In terms of quantum scattering problems, the solution of the (7-1) is governed by the Lippmann-Schwinger equation (Landau and Lifshitz, 1958; Rodberg and Thaler, 1967):

$$\Psi = \Psi^{b.c.} + \mathcal{V}^{Sc} \tag{7-2}$$

$\Psi^{b.c.}$ is the unperturbed Ψ, $\mathcal{V}^{Sc}$ is a perturbation of Ψ. Eq. (7-2) can be written as:

$$\Psi(\xi) = \Psi^{b.c.}(\xi) + \int_{\Omega} G(\xi, \xi')V'\Psi(\xi')d\xi' \tag{7-3}$$

$G(\xi, \xi')$ is the fundamental solution for operator L, $V'\Psi(\xi')$ is the perturbation, $(\xi, \xi') \in \Omega$. In terms of quantum scattering theory, the general form of the Lippmann-Schwinger equation can be written in a particular form for a specific function Ψ — [1] the Hamiltonian H (corresponding equations can be found in Landau and Lifshitz (1958) and in Colton and Kress (2012)), [2] the wave field u and [3] the stress or strain field ϵ or σ, respectively. For the wave field u equation (7-3) is the same as Eq. (3-24) (Colton and Kress, 2012; Broggini and Snieder, 2012):

$$u(\xi) = u^{b.c.}(\xi) + \int_{\Omega} G(\xi, \xi')L'u(\xi')d\xi' \tag{7-4}$$

where u is the total wave field, $u^{b.c.}$ is the incident wave field which denotes the boundary conditions, L' is the perturbation and G is the propagator. For the strain field ϵ, equation (7-3) is the same as Eq. (5-10) (Zeller and Dederichs, 1973; Gubernatis and Krumhansl, 1975):

$$\boldsymbol{\epsilon}(\xi) = \boldsymbol{\epsilon}^{b.c.}(\xi) + \int \boldsymbol{\mathcal{G}}^{(\mathbf{0})}(\xi, \xi')\mathbf{C}'(\xi')\boldsymbol{\epsilon}(\xi')d\xi' \tag{7-5}$$

$\boldsymbol{\epsilon}$ is the total strain field. $\boldsymbol{\epsilon}^{b.c.}$ denotes the boundary conditions for the displacements at infinity. $\mathbf{C}'$ is the medium's perturbations. $\boldsymbol{\mathcal{G}}^{(\mathbf{0})}$ is the propagator.

In other words, Eq. (7-4) describes the **wave field** scattering in an inhomogeneous medium while Eq. (7-5) describes the **strain field** scattering. By using equation Eq. (7-5), we can

obtain the inhomogeneous medium's averaged properties (by applying several additional assumptions, which are beyond the scope of this chapter). Then, by solving the Christoffel equation we obtain the phase and group velocities. Thus, equation Eq. (7-4) can be called the 'macro-scale' Lippmann-Schwinger equation and equation Eq. (7-5) can be called the 'micro-scale' Lippmann-Schwinger equation. The original theory of the Lippmann-Schwinger equation was developed in quantum scattering theory.

When either the macro- or micro- scales of the Lippmann-Schwinger equations are used in scientific works, they are usually linked to the quantum mechanics version of this equation, albeit separately. However, we can link these two versions of the Lippmann-Schwinger equations through up-scaling. Micro-scale wave propagation can be considered as a stress or strain propagation in the micro-inhomogeneous medium because at this scale, the wave field is no longer a wave and there is no time derivative. On the other hand, macro-scale wave propagation is governed by the averaged medium's properties over the representative elementary volume. Thus, by using the Christoffel equation the up-scaling, which is the key, can be done; And therefore, we can link seismic imaging and rock physics using viscoelasticity. As a result, the Lippmann-Schwinger equation and scattering at 'micro-scale' is the next, natural step, following the paper by Broggini and Snieder (2012), the 'Connection of Scattering Principles: a Visual and Mathematical Tour.'

7-2 Rock Physics Modeling

Reservoirs can cause some problems due to high attenuation; Therefore, I created a five-layered model with two variants: [1] without a reservoir (Model 3a), and [2] with a reservoir as the third layer (Model 3b). Each layer has a different velocity, density and attenuation. Moreover, the thickness of the third layer is 200 meters for both variants. In Model 3a (reservoir-less), the third layer is a carbonate rock with some clay content. The properties are: Vp=4.0 (km/s), Vs=2.2 (km/s) and ρ=2.69 (g/cm^3). The medium properties for Model 3a are shown in the table C-5 on page 96. In Model 3b (with a reservoir) the third layer represents a reservoir with 20% porosity. The reservoir's properties (Vp, Vs, ρ, Q-factor) can be modelled using different rock physics models. The medium properties for this second variant with a reservoir are shown in the table C-6 on page 96 (Model 3b).

7-2-1 Generalized Dvorkin-Mavko Attenuation Model

Dvorkin and Mavko (2006) proposed a method to calculate the P- and S- wave quality factor of a reservoir rock. I've extended the idea of this method to calculate a rock's properties, using the T-matrix approach (Figure 7-1). (The method to simulate the properties of the porous rocks is given in detail in chapter 5, pages 36-37). I assumed that the reservoir is a shale with a clay matrix, and that the porosity is 20%. Also, some parts are shaly sands. The reservoir is filled with water and gas. It's important to note that some small volumes in the reservoir are fully water-saturated while some volumes may contain gas. Attenuation is linked to the changes in the elastic modulus versus frequency. Instead of using a specific mechanism for the attenuation, the Q-factor of the reservoir rock was modelled by using a linear viscoelastic

solid (Dvorkin and Mavko, 2006). In this model, only the low frequency modulus of the rock (i.e. the low frequency limit) and a hight frequency modulus (i.e. the high frequency limit) are needed. I assumed that at low frequencies the induced pore pressures are equilibrated throughout the pore space (i.e., there is sufficient time for the pore fluid to flow and eliminate wave-induced pore-pressure gradients) (Mavko et al., 2009). This is called the 'relaxed' or 'quasi-static' limit for P-wave phase velocities. Therefore, I calculated the 'dry-frame' elastic modulus of the rock using the T-matrix approach. The term 'dry-frame' means that the pore fluid has zero bulk modulus. In this case, the pore compression during wave propagation does not induce changes in pore pressure. As a result I got the elastic properties of the 'dry-frame'. The pores were modelled as spheroids with an aspect ratio equal to 1 (i.e. spheres). I also assumed that some parts have quite strong connectivity, therefore, the dry rock has a low bulk modulus. The effective bulk moduli of the dry rock were calculated by using the T-matrix method. The dry bulk modulus of the reservoir rock is K_{dry}= 5.9 GPa. As the second step, I filled the pore space with fluid by using the Biot-Gassmann theory. At low frequencies, the effective bulk modulus K_F of the liquid and gas parts is the harmonic average of water K_{water} and gas K_{gas} bulk moduli. I calculated the bulk modulus and density for gas at reservoir conditions (high pore pressure) using the Batzle-Wang formulas (Batzle and Wang, 1992). I assumed that the pore pressure is P_p=300 bar. The gas has the properties: K_{gas} = 0.133 GPa and ρ_{gas} = 0.336 (g/cm^3). Water has the properties: K_{water} = 3.0133 GPa and ρ_{water} = 1.055 (g/cm^3). As a result, the saturated reservoir has the properties: Vp = 2.49 (km/s) and ρ = 2.00 (g/cm^3).

At high frequencies, I assumed that pores are not sensitive with respect to fluid flow, i.e. there is no time for flow-induced equilibration of pore pressures (Mavko et al., 2009). Firstly, I applied the high frequency Biot-Gassmann theory to calculate the modulus of the rock at high frequencies it produced a modulus that was too low and closer to the saturated modulus (closer to the low frequency modulus). Then, I calculated the high frequency modulus of the rock using the T-matrix approach and I assumed a very low connectivity in the pore space closer to the upper Hashin-Shtrikman bounds). Also, my goal was to produce a high velocity in order to create high attenuation in the reservoir. As a result, the saturated reservoir at high frequencies has the velocity Vp = 2.7 (km/s). The medium properties are shown in the table C-6 on page 96 (Model 3b).

Figure 7-2 shows the velocity dispersion curve in the frequency domain for the constructed rock's model. In this work, we are mostly interested in Q behavior, therefore, the low frequency velocity was used in the modeling. The low frequency velocity is an appropriate choice for seismic frequencies. Figure 7-3 illustrates the nearly constant Q-factor model in the frequency domain. Each curve in Figure 7-3 is a Zener model with a different critical frequency f_c. The critical frequency f_c is the frequency at which the inverse quality factor has a maximum value. That is an additional property of the porous rock. Because I am using De Hoop's model with two parameters and this is a synthetic model, I used the attenuation α_H in Model 3b which gives the same attenuation as the constructed rock's model (Figure 7-2 and Figure 7-3). Moreover, for verification of the constructed rock's model with experimantal data and other methods, I used the books Barton (2007), Schön (2011), Mavko et al. (2009) and Dvorkin et al. (2014). Therefore, the properties of the constructed reservoir are typical of the available experimental data.

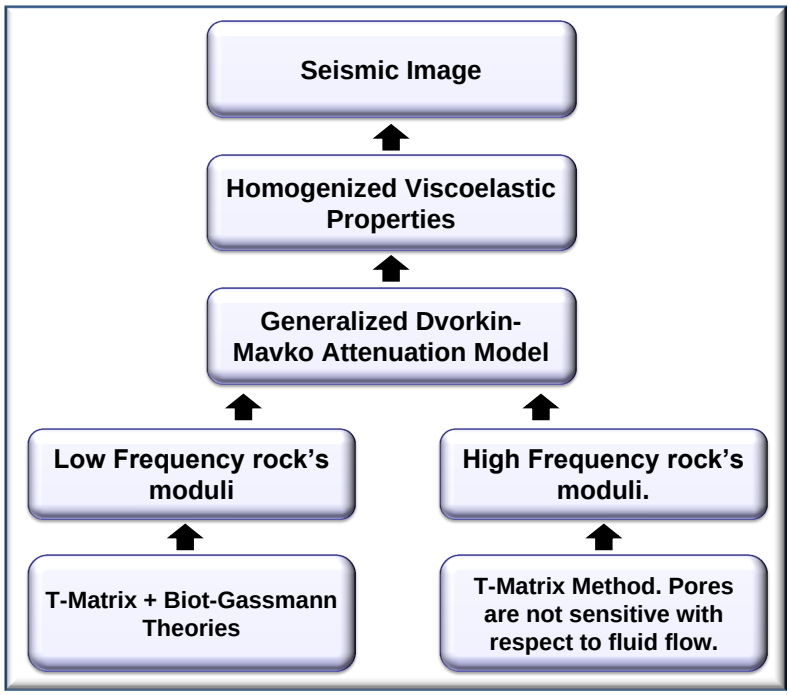

Figure 7-1: The schematic overview of the proposed upscaling method. Seismic imaging and rock physics are linked through viscoelasticity of the medium. The upscaling approach starts with defining the rock's microstructure and properties of the components. Then, by applying the scheme, the homogenized viscoelastic properties can be obtained.

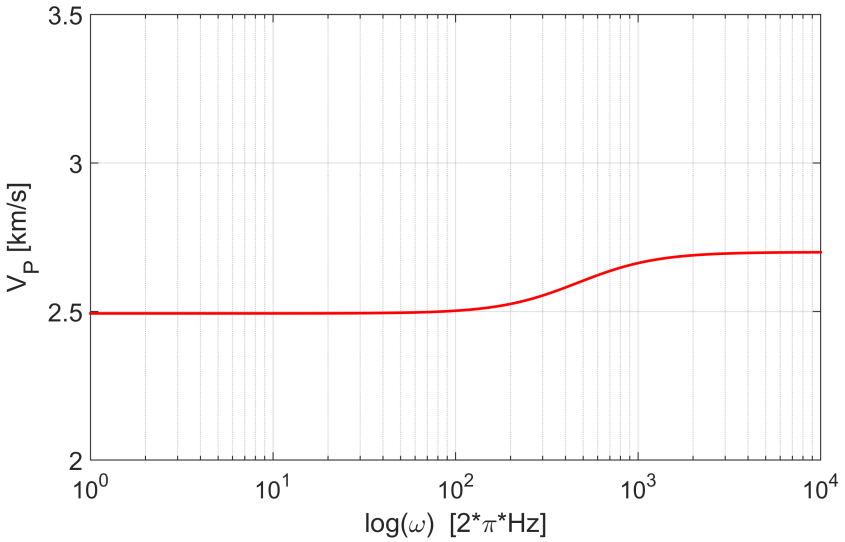

Figure 7-2: Schematic of the velocity dispersion in the frequency domain.

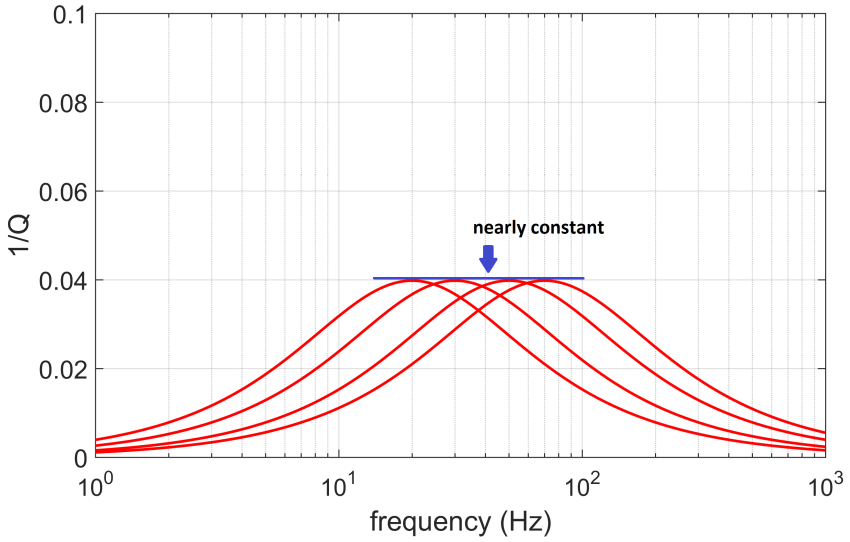

Figure 7-3: Schematic of the nearly constant Q-factor model in the frequency domain.

7-2-2 Effective Q-factor Model and Artefact Model

Figure 7-4 shows the two reflection series. The first reflection series was calculated for lossless media (black curve). The second reflection series was calculated for lossy media. The intrinsic loss was modelled using De Hoop's model with two parameters (Model 3a). Figure 7-5 shows the two reflection series for Model 3b. The reflections below the third strong reflector are very low. This is because the attenuation in the third layer (reservoir) is very strong.

The correct compensation parameter for Model 3a can be inverted by using the Artefact Removal Method. The results are shown in Figures G-1, G-2 and G-3. The focal point is at a depth of 2000 meters. But in this inversion, instead of using the upgoing Green's function, the focusing function f_1^- was used. The approach is absolutely the same. Instead of the function $\widehat{\mathcal{T}}_G^i(\mathbf{x},\omega)$ (calculated using the upgoing Green's function) I used the function $\widehat{\mathcal{T}}_{f1}^i(\mathbf{x},\omega)$ (calculated using the focusing function f_1^-) etc. (Nota bene: that the attenuation in Model 3a is slightly different for different layers). The inverted compensation $\zeta_{compensation} = 0.4$ is the correct value. It corresponds to effective Q-factor. By applying $\zeta_{compensation} = 0.4$ to the lossy reflection series, I got the lossless one (with a low percentage of errors) (Figure 7-6).

In Model 3b, the third layer represents a reservoir with very high attenuation. Therefore, it might cause some problems. Figures G-1, G-2 and G-3 were recreated for Model 3b. They are not shown because they are absolutely identical, i.e. there is no difference between Model 3a and Model 3b. Then, all the steps were repeated for $\zeta_{compensation} = 0.35$, 0.36, 0.37, 0.38, 0.39 and 0.41 (i.e. closer to the minimum). Moreover, the second artefact was normalized by multiplying the corresponding time interval in the f_1^- by 100. That was done to make the amplitudes of all artefacts equal to each other (because it is unknown which artefact corresponds to which layer). Figure G-4 shows the function $\widehat{\mathcal{T}}_{f1}^i(\mathbf{x},\omega)$, which was calculated using the focusing function f_1^- instead of $G^{-,+}$. It is clear that the minimum of $\widehat{\mathcal{T}}_{f1}^i(\mathbf{x},\omega)$ corresponds to $\zeta_{compensation} = 0.37$. But this minimum is not perfect, mainly because the second artefact was overcompensated, because the impact of this artefact on in the inverse

problem solution was overestimated. It can be further examined in Figure G-5. While the first artefact in Figure G-5 is almost zero for $\zeta_{compensation} = 0.37$, the second artefact is non zero for any $\zeta_{compensation}$. The work flow was repeated for Model 3a, and the same result was obtained. It means that the artefacts caused by the third layer are very small and cannot be seen in the figures. Therefore, the Artefact Removal Method gives the same compensation parameter for Model 3a and for Model 3b. But, this problem can be solved if we apply the Artefact Removal Method to the redatumed reflection series.

Figure 7-8 shows the redatumed reflection responses which were shifted down and zoomed in to show the artefacts (Model 3a). The black curve corresponds to the redatumed reflection response calculated for lossless medium. This is a perfect redatumed reflection response, no artefacts are present. The red, blue and brown curves correspond to the redatumed reflection responses, calculated for compensated lossy medium with $\zeta_{compensation} = 0.1$, 0.4, 0.5, respectively. The blue curve is the closest to the correct one because the artefacts are small. Figure 7-9 is the same as Figure 7-8 but calculated for Model 3b. The artefacts are clearly visible. The blue curve shows small artefacts for all events except the last one. This artefact is shown by an arrow in Figure 7-9. Because of this artefact, we can conclude that there is a layer with a very strong attenuation; Therefore, an effective temporal Q-factor for Model 3b doesn't exist. But it exists for Model 3a because the blue curve gives small amplitudes for all artefacts.

7-3 Conclusion

In this thesis, the macro-scale homogenized viscoelastic properties were calculated by using the T-matrix Approach and the Generalized Dvorkin-Mavko Attenuation Model. All theoretical results are supported by synthetic 1D modeling. The theoretical part of thesis and a general work flow can be used for a very complex medium. The Artefact Removal Method was tested on Models 3a-3b. It works very well where the difference in attenuation between layers is (approximately) less than 10-50% (as illustrated in Model 3a). If there is a layer with very strong attenuation, the effective temporal Q-factor can be found for an interval between the acquisition surface and the layer/layers with very strong attenuation (as seen in Model 3b).

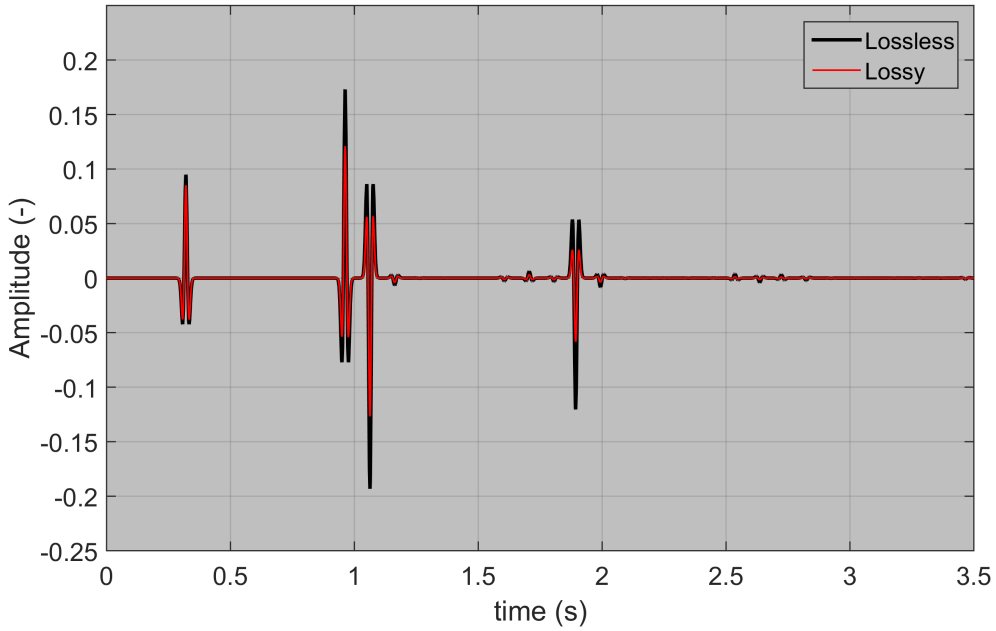

Figure 7-4: Lossless (black curve) and lossy (red curve) reflection series for Model 3a. The x-axis represents time in seconds. The y-axis represents the amplitude. The intrinsic loss was modelled using De Hoop's model with two parameters (Model 3a).

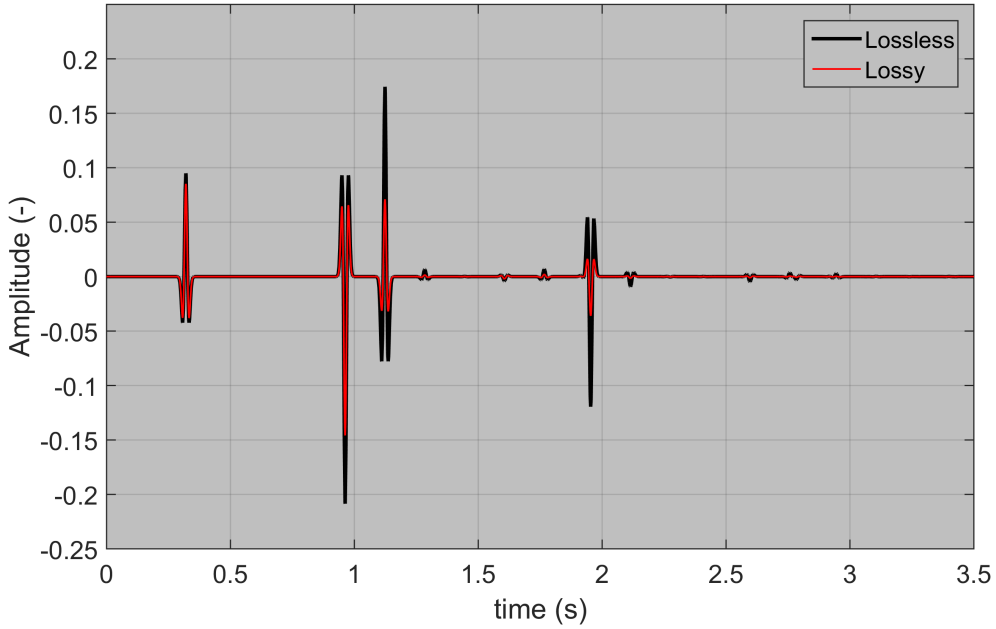

Figure 7-5: Lossless (black curve) and lossy (red curve) reflection series for Model 3b. The x-axis represents time in seconds. The y-axis represents the amplitude. The intrinsic loss was modelled using De Hoop's model with two parameters. The third layer represents a reservoir with 20% porosity.

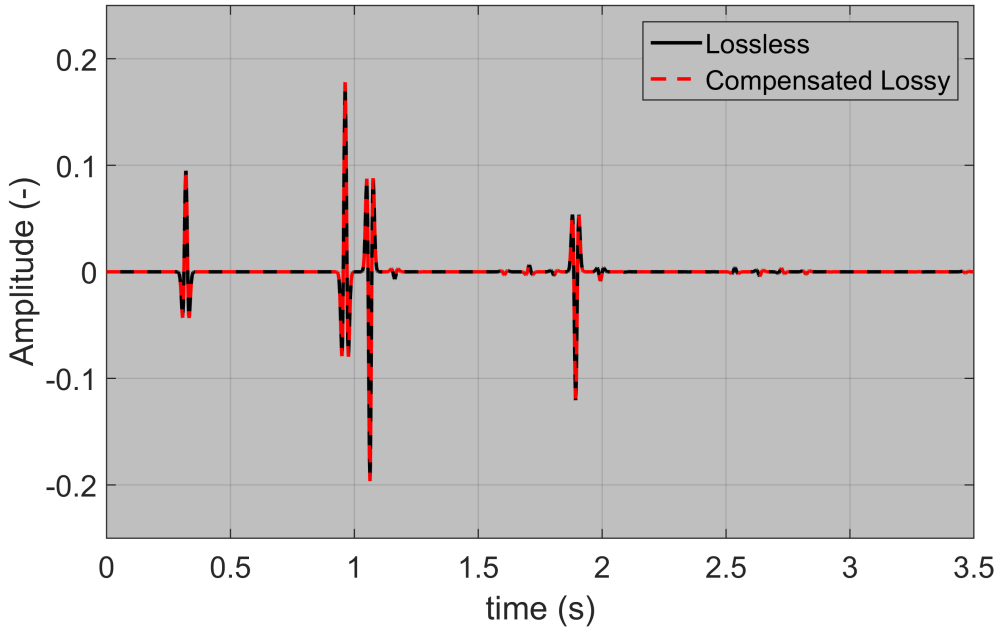

Figure 7-6: Lossless (black curve) and compensated lossy (dashed red curve) reflection series for Model 3a. The x-axis represents time in seconds. The y-axis represents the amplitude. The compensation parameter applied to the lossy reflection series is $\zeta_{compensation} = 0.4$

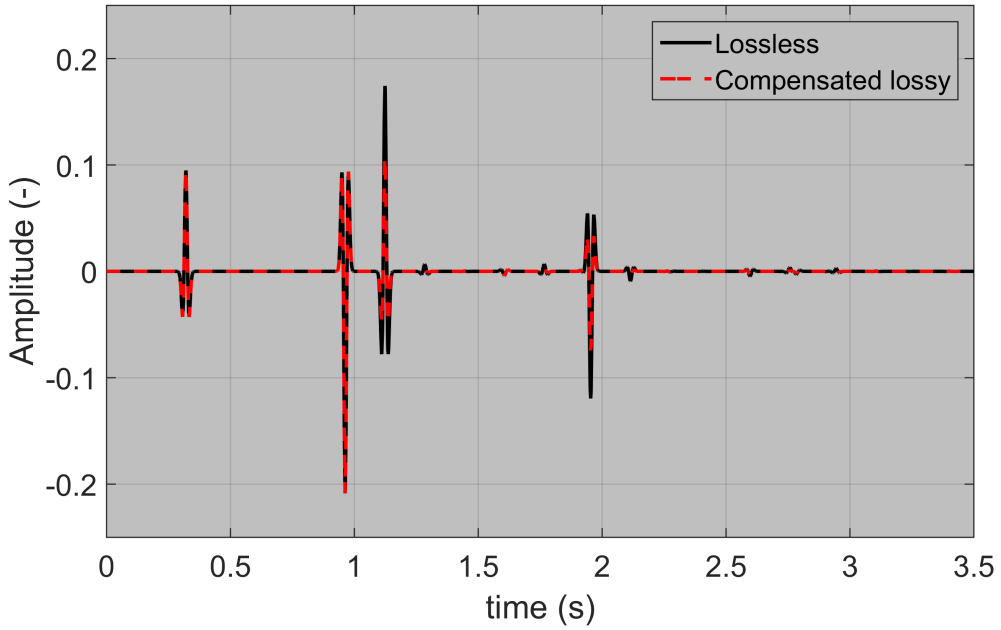

Figure 7-7: Lossless (black curve) and compensated lossy (dashed red curve) reflection series for Model 3b. The x-axis represents time in seconds. The y-axis represents the amplitude. The compensation parameter applied to the lossy reflection series is $\zeta_{compensation} = 0.37$. This compensation is valid only for the first two layers.

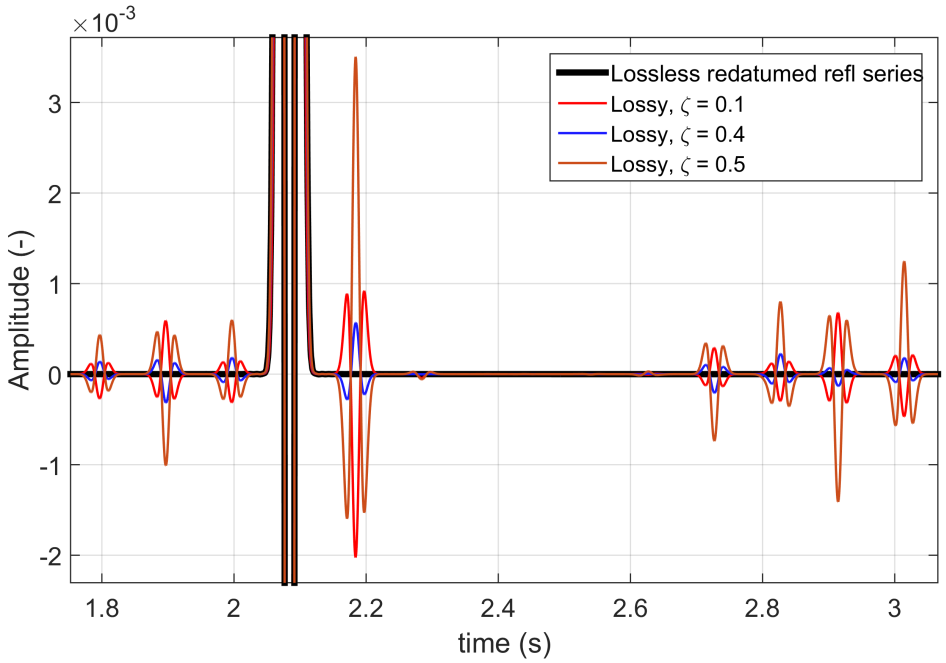

Figure 7-8: Redatumed reflection response for lossless medium (black) and the redatumed reflection response for compensated lossy medium (Model 3a). The figure is zoomed in to 1.5-2.9 seconds and $-2 * 10^{-3}$-$3.5 * 10^{-3}$ amplitudes to show the artefacts.

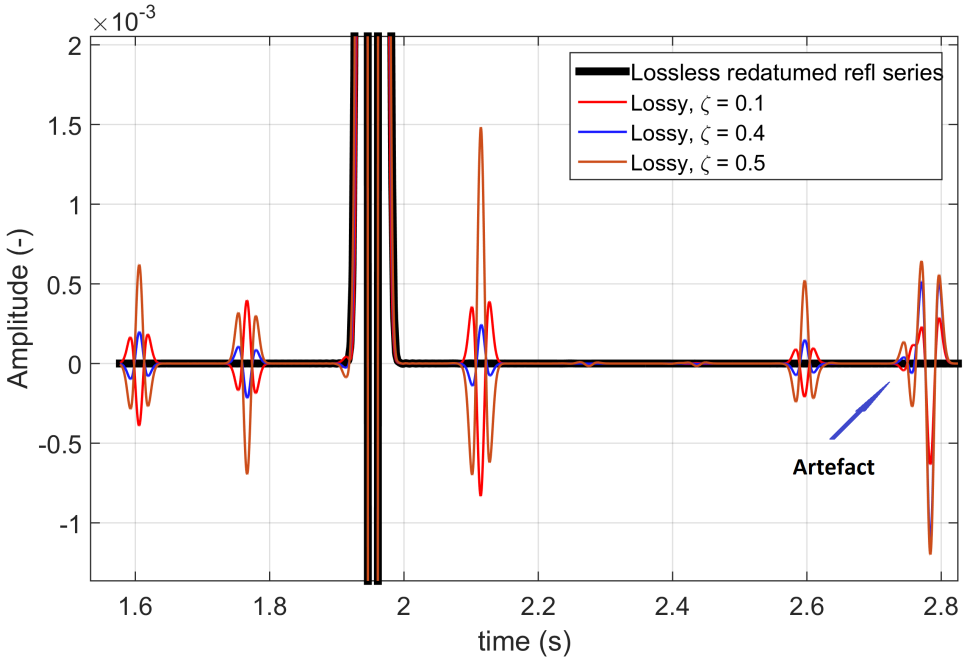

Figure 7-9: Redatumed reflection response for lossless medium (black) and the redatumed reflection response for compensated lossy medium (Model 3b). The figure is zoomed in to 1.5-2.9 seconds and $-1 * 10^{-3}$-$2 * 10^{-3}$ amplitudes to show the artefacts. The desired artefact is shown by an arrow.

Chapter 8

General Conclusions and Future Research

8-1 General Conclusions

The connection between the different types of Lippmann-Schwinger equations was shown. The macro- and micro- scale Lippmann-Schwinger equations describe the wave field and the strain field scattering in an inhomogeneous medium, respectively. These two versions of the Lippmann-Schwinger equations are connected through up-scaling. This approach is explained in section (6-1) (theory) and in section (6-5) (synthetic simulation). The forward problem is the following (from micro-scale to macro-scale): [A] By using the micro-scale Lippmann-Schwinger equation and some additional rock physics models the effective viscoelastic moduli of the rock can be calculated. In this thesis, it was done by using the T-matrix Approach and the Generalized Dvorkin-Mavko Attenuation Model. [B] The calculated rock's properties were implemented into the layered model of the subsurface. The forward modeling showed that the micro-scale properties of a heterogeneous porous medium are represented as homogenized viscoelastic properties of the medium at macro-scale. Thus, the uspcaling scheme can be constructed. On the other hand, the downscaling problem (from homogenized viscoelastic properties to the heterogeneous porous medium's properties), in general, cannot be resolved because the uncertainties are too numerous and too substantial.

The Artefact Removal Method was proposed to quantify attenuation in the subsurface. This method is based on the fact that the solution of the Marchenko equation is exact (Nota Bene: Evanescent waves are excluded); However, there are artefacts present in the solution if some assumptions of the medium are not fulfilled. Artefacts in the solution are caused by: [A] numerical limitations (these artefacts are very small) and [B] additional medium's assumptions. Properties which can cause some artefacts in the solution are: [i] the anisotropy of the medium, [ii] an incorrectly scaled source signature, [iii] an incorrect velocity model, [iv] an incorrect compensation for transmission losses, [v] an incorrect compensation for intrinsic losses (or, simply, lossy medium) etc. In this thesis, the medium assumptions [i]-[iv] were

fulfilled. Therefore, the artefacts are present because the medium is lossy. These artefacts have a very specific behaviour: if the input data to the Marchenko equation is over- or under- compensated, the resulting artefacts will have an opposite polarity. Thus, they can be recognized. The artefacts are present in the upgoing Green's function, upgoing focusing function of the first kind, the redatumed reflection series, etc. Thus, by applying different compensation parameters to the lossy reflection series, the artefacts can be removed and, hence, the correct compensation for the losses can be found. The method works very well for the medium where the losses can be compensated via an effective temporal Q-factor. This is shown by Models 1, 2a, 2b, 3a. If there is a layer/layers with a very strong attenuation, the effective temporal Q-factor can be found for an interval between the acquisition surface and the layer/layers with very strong attenuation. This is shown in Model 2c. The layer with a very high attenuation can be found but this requires additional modeling (Model 3b).

The time-dependent compensation Q-factor doesn't seem to work even for a simple medium. The idea was to invert the time-dependent compensation Q-factor by minimizing the artefacts in the upgoing Green's function, upgoing focusing function and in the redatumed reflection series. In general, the time-dependent compensation Q-factor can be found but too many unknown parameters for such compensation are needed. For example, for a simple five layer model, at least 20 different compensation parameters are needed. This inverse problem is unstable and very expensive. It might work only if additional modeling is applied. But it is difficult to model all possible multiples within different layers and their subsequent interactions and invert to the correct time-dependent compensation Q-factor.

Marchenko redatuming for lossy medium works very well when the losses can be compensated via an effective temporal Q-factor. If there is a layer/layers with a very strong attenuation, the redatumed reflection series will contain some undesired artefacts. Therefore, further research is required.

8-2 Future Research

It is my belief that the lossless Marchenko scheme can be modified in such a way that the losses are incorporated.

Moreover, it has been suggested to jointly study the artefacts caused by assumptions [i]-[v], as outlined above. It is the belief of this author that in each case these artefacts have very specific behaviour and can be recognized. But, admittedly, for a very complex subsurface medium, the artefact behaviour might be very complicated.

It has been suggested to modify the focusing algorithm provided by Wapenaar et al. (2013) in such a way that the free-surface multiples are incorporated. This can be done by using the modification provided by Singh et al. (2015). Therefore, the Artefact Removal Method can be improved by focusing just below each layer (one-by-one, starting with the first layer) and thus, removing the topmost layer, one-by-one. Dr. Slob (Delft University of Technology) shared the original idea of this approach. Without the Singh et al. (2015) modification, the Artefact Removal Method works well when the attenuation can be approximated with an effective Q-factor — layers can be removed using seismic interferometry.

Regarding the upscaling problem, it can be done using more sophisticated methods. For example, different types of fluid flow can be taken into account. A more complicated rock's microstructure can be implemented as well.

Bibliography

Agranovich, Z. S. and Marchenko, V. A. (1964). *The inverse problem of scattering theory*. Gordon and Breach.

Aki, K. and Richards, P. G. (2002). *Quantitative seismology*.

Alkhimenkov, Y. (2015). Practical applications of the t-matrix approach to fractured porous rocks. In *SPE Annual Technical Conference and Exhibition*. Society of Petroleum Engineers.

Alkhimenkov, Y. and Bayuk, I. (2017). Unified effective medium theory for cracked porous rocks-theory and case study. In *79th EAGE Conference and Exhibition 2017*.

Alkhimenkov, Y. A. (2017). The t-matrix approach for the mathematical modeling of the effective elastic properties of hydrocarbon reservoirs. *Izvestiya, Physics of the Solid Earth*, 53(3):477–487.

Ambarzumian, V. (1929). Über eine frage der eigenwerttheorie. *Zeitschrift für Physik A Hadrons and Nuclei*, 53(9):690–695.

Amundsen, L. (2001). Elimination of free-surface related multiples without need of the source wavelet. *Geophysics*, 66(1):327–341.

Amundsen, L. and Robertsson, J. O. (2014). Wave equation processing using finite-difference propagators, part 1: Wavefield dissection and imaging of marine multicomponent seismic data. *Geophysics*.

Anderson, D. L. (1989). *Theory of the Earth*. Blackwell scientific publications.

Arora, K., Cazenave, A., Engdahl, E. R., Kind, R., Manglik, A., Roy, S., Sain, K., and Uyeda, S. (2011). *Encyclopedia of solid earth Geophysics*. Springer Science & Business Media.

Avseth, P., Mukerji, T., and Mavko, G. (2010). *Quantitative seismic interpretation: Applying rock physics tools to reduce interpretation risk*. Cambridge university press.

Barton, N. (2007). *Rock quality, seismic velocity, attenuation and anisotropy*. CRC press.

Batzle, M. and Wang, Z. (1992). Seismic properties of pore fluids. *Geophysics*, 57(11):1396–1408.

Bayuk, I. O., Ammerman, M., and Chesnokov, E. M. (2007). Elastic moduli of anisotropic clay. *Geophysics*, 72(5):D107–D117.

Biot, M. A. (1956a). Theory of propagation of elastic waves in a fluid-saturated porous solid. i. low-frequency range. *The Journal of the acoustical Society of america*, 28(2):168–178.

Biot, M. A. (1956b). Theory of propagation of elastic waves in a fluid-saturated porous solid. ii. higher frequency range. *the Journal of the Acoustical Society of America*, 28(2):179–191.

Biot, M. A. (1962). Mechanics of deformation and acoustic propagation in porous media. *Journal of applied physics*, 33(4):1482–1498.

Borg, G. (1952). Uniqueness theorems in the spectral theory of y+(λ- q (x)) y= 0. In *Proc. 11th Scandinavian Congress of Mathematicians, Johan Grundt Tanums Forlag, Oslo*, pages 276–287.

Brackenhoff, J. (2016). Rescaling of incorrect source strength using marchenko redatuming.

Broggini, F. and Snieder, R. (2012). Connection of scattering principles: A visual and mathematical tour. *European Journal of Physics*, 33(3):593.

Broggini, F., Snieder, R., and Wapenaar, K. (2014). Data-driven wavefield focusing and imaging with multidimensional deconvolution: Numerical examples for reflection data with internal multiples. *Geophysics*, 79(3):WA107–WA115.

Burridge, R. (1980). The gelfand-levitan, the marchenko, and the gopinath-sondhi integral equations of inverse scattering theory, regarded in the context of inverse impulse-response problems. *Wave motion*, 2(4):305–323.

Carcione, J. (2014). *Wave Fields in Real Media: Wave Propagation in Anisotropic, Anelastic, Porous and Electromagnetic Media: Third Edition*. cited By 19.

Carcione, J. M., Helle, H. B., and Pham, N. H. (2003). White's model for wave propagation in partially saturated rocks: Comparison with poroelastic numerical experiments. *Geophysics*, 68(4):1389–1398.

Carcione, J. M. and Picotti, S. (2006). P-wave seismic attenuation by slow-wave diffusion: Effects of inhomogeneous rock properties. *Geophysics*, 71(3):O1–O8.

Christensen, R. M. (1982). Theory of viscoelasticity [m].

Colton, D. and Kress, R. (2012). *Inverse acoustic and electromagnetic scattering theory*, volume 93. Springer Science & Business Media.

da Costa Filho, C. A., Ravasi, M., Curtis, A., and Meles, G. A. (2014). Elastodynamic green's function retrieval through single-sided marchenko inverse scattering. *Physical Review E*, 90(6):063201.

Daubechies, I. (1992). *Ten lectures on wavelets*. SIAM.

de Hoop, A. T. (2001). Handbook of radiation and scattering of waves: Acoustic waves in fluids, elastic waves in solids, electromagnetic waves.

de Hoop, Maarten, V. and de Hoop, Adrianus, T. (2000). Wave–field reciprocity and optimization in remote sensing. In *Proceedings of the Royal Society of London A: Mathematical, Physical and Engineering Sciences*, volume 456, pages 641–682. The Royal Society.

Draganov, D., Ghose, R., Ruigrok, E., Thorbecke, J., and Wapenaar, K. (2010). Seismic interferometry, intrinsic losses and q-estimation. *Geophysical Prospecting*, 58(3):361–373.

Dvorkin, J., Gutierrez, M. A., and Grana, D. (2014). *Seismic reflections of rock properties*. Cambridge University Press.

Dvorkin, J. P. and Mavko, G. (2006). Modeling attenuation in reservoir and nonreservoir rock. *The Leading Edge*, 25(2):194–197.

Egorov, Y. V. and Shubin, M. A. (1988). Linear partial differential equations. foundations of the classical theory. *Itogi Nauki i Tekhniki. Seriya" Sovremennye Problemy Matematiki. Fundamental'nye Napravleniya"*, 30:5–255.

Eshelby, J. D. (1957). The determination of the elastic field of an ellipsoidal inclusion, and related problems. In *Proceedings of the Royal Society of London A: Mathematical, Physical and Engineering Sciences*, volume 241, pages 376–396. The Royal Society.

Faddeyev, L. D. and Seckler, B. (1963). The inverse problem in the quantum theory of scattering. *Journal of Mathematical Physics*, 4(1):72–104.

Fokkema, J. T. and Ziolkowski, A. (1987). The critical reflection theorem. *Geophysics*, 52(7):965–972.

Folland, G. B. (1999). Real analysis: Modern techniques and their applications, john willey and sons. *Inc., New York*.

Gelfand, I. M. and Levitan, B. M. (1951). *On the determination of a differential equation from its spectral function*, volume 15. American Mathematical Society Tansl. Ser. 2 1, 253 (1955).

Gubernatis, J. E. and Krumhansl, J. A. (1975). Macroscopic engineering properties of polycrystalline materials: Elastic properties. *Journal of Applied Physics*, 46(5):1875–1883.

Gurevich, B. and Lopatnikov, S. (1995). Velocity and attenuation of elastic waves in finely layered porous rocks. *Geophysical Journal International*, 121(3):933–947.

Hashin, Z. (1970). Complex moduli of viscoelastic compositesi. general theory and application to particulate composites. *International Journal of Solids and Structures*, 6(5):539–552.

Jakobsen, M. (2004). The interacting inclusion model of wave-induced fluid flow. *Geophysical Journal International*, 158(3):1168–1176.

Jakobsen, M. and Chapman, M. (2009). Unified theory of global flow and squirt flow in cracked porous media. *Geophysics*, 74(2):WA65–WA76.

Jakobsen, M., Hudson, J. A., and Johansen, T. A. (2003). T-matrix approach to shale acoustics. *Geophysical Journal International*, 154(2):533–558.

Jakobsen, M. and Johansen, T. A. (2005). The effects of drained and undrained loading on visco-elastic waves in rock-like composites. *International Journal of Solids and Structures*, 42(5):1597–1611.

Kjartansson, E. (1979). Constant q-wave propagation and attenuation. *Journal of Geophysical Research: Solid Earth*, 84(B9):4737–4748.

Kramers, H. A. (1927). *La diffusion de la lumiere par les atomes*.

Kudarova, A. (2016). Effective models for seismic wave propagation in porous media.

Lamb Jr, G. L. (1980). Elements of soliton theory. *New York, Wiley-Interscience, 1980. 300 p.*

Landau, L. D. and Lifshitz, E. (1958). *Quantum mechanics: non-relativistic theory*. Pergamon Press.

Landau, L. D. and Lifshitz, E. (1986). Theory of elasticity, vol. 7. *Course of Theoretical Physics*, 3:109.

Landau, L. D. and Lifshitz, E. M. (1969). *Statistical Physics: V. 5: Course of Theoretical Physics*. Pergamon press.

Levitan, B. M. (1987). *Inverse Sturm-Liouville problems*. Utrecht, the Netherlands: VNU Science Press.

Levitan, B. M. and Sargsian, I. S. (1975). *Introduction to spectral theory: selfadjoint ordinary differential operators: Selfadjoint Ordinary Differential Operators*, volume 39. American Mathematical Soc.

Li, Y. (2014). Wave equation migration velocity analysis for vti models with geological and rock physics constraints.

Mallat, S. (2008). *A wavelet tour of signal processing: the sparse way*. Academic press.

Marchenko, V. A. (1952). Some questions of the theory of one-dimensional linear differential operators of the second order. i. *Trudy Moskovskogo Matematicheskogo Obshchestva*, 1:327–420.

Marchenko, V. A. (1955). On reconstruction of the potential energy from phases of the scattered waves. In *Dokl. Akad. Nauk SSSR*, volume 104, pages 695–698.

Marchenko, V. A. (2011). *Sturm-Liouville operators and applications*, volume 373. American Mathematical Soc.

Mavko, G., Mukerji, T., and Dvorkin, J. (2009). *The rock physics handbook: Tools for seismic analysis of porous media*. Cambridge university press.

Mildner, C., Broggini, F., de Vos, K., and Robertsson, J. (2017). Source wavelet amplitude spectrum estimation using marchenko focusing functions. In *79th EAGE Conference and Exhibition 2017*.

Müller, T. M., Gurevich, B., and Lebedev, M. (2010). Seismic wave attenuation and dispersion resulting from wave-induced flow in porous rocksa review. *Geophysics*, 75(5):75A147–75A164.

Mura, T. (1982). Micromechanics of defects in solids.

O'connell, R. and Budiansky, B. (1978). Measures of dissipation in viscoelastic media. *Geophysical Research Letters*, 5(1):5–8.

ODonnell, M., Jaynes, E., and Miller, J. (1981). Kramers–kronig relationship between ultrasonic attenuation and phase velocity. *The Journal of the Acoustical Society of America*, 69(3):696–701.

Qi, Q., Müller, T. M., and Rubino, J. G. (2014). Seismic attenuation: effects of interfacial impedance on wave-induced pressure diffusion. *Geophysical Journal International*, 199(3):1677–1681.

Reed, M. and Simon, B. (1980). *Methods of modern mathematical physics. vol. 1. Functional analysis*. Academic New York.

Rodberg, L. S. and Thaler, R. M. (1967). Introduction to the quantum theory of scattering.

Rose, J. H. (2001). 'single-sided' focusing of the time-dependent schrödinger equation. *Physical Review A*, 65(1):012707.

Rose, J. H. (2002). 'single-sided' autofocusing of sound in layered materials. *Inverse problems*, 18(6):1923.

Rubino, J. and Holliger, K. (2013). Research note: Seismic attenuation due to wave-induced fluid flow at microscopic and mesoscopic scales. *Geophysical Prospecting*, 61(4):882–889.

Schön, J. (2011). *Physical properties of rocks: A workbook*, volume 8. Elsevier.

Shapiro, S. A. and Müller, T. M. (1999). Seismic signatures of permeability in heterogeneous porous media. *Geophysics*, 64(1):99–103.

Shen, Y. (2016). *Wave-equation Migration Q Analysis*. PhD thesis, Stanford University.

Singh, S., Snieder, R., Behura, J., van der Neut, J., Wapenaar, K., and Slob, E. (2015). Marchenko imaging: Imaging with primaries, internal multiples, and free-surface multiples. *Geophysics*.

Teolis, A. (2012). *Computational signal processing with wavelets*. Springer Science & Business Media.

Thorbecke, J., Neut, J. v. d., and Wapenaar, K. (2013). Green's function retrieval with marchenko equations: A sensitivity analysis. In *SEG Technical Program Expanded Abstracts 2013*, pages 3888–3893. Society of Exploration Geophysicists.

Torquato, S. (2002). Random heterogeneous materials: microstructure and macroscopic properties.

Ursin, B. and Toverud, T. (2002). Comparison of seismic dispersion and attenuation models. *Studia geophysica et geodaetica*, 46(2):293–320.

van der Neut, J., Vasconcelos, I., and Wapenaar, K. (2015). On green's function retrieval by iterative substitution of the coupled marchenko equations. *Geophysical Journal International*, 203(2):792–813.

Vasconcelos, I. (2007). *Interferometry in perturbed media*, volume 68.

Verschuur, D. and Berkhout, A. (1997). Estimation of multiple scattering by iterative inversion, part ii: Practical aspects and examples. *Geophysics*, 62(5):1596–1611.

Vladimirov, V. S., Jeffrey, A., and Schroeck, F. E. (1971). Equations of mathematical physics. *American Journal of Physics*, 39(12):1548–1548.

Wapenaar, C. and Grimbergen, J. (1996). Reciprocity theorems for one-way wavefields. *Geophysical Journal International*, 127(1):169–177.

Wapenaar, K. (1998). Reciprocity properties of one-way propagators. *Geophysics*, 63(5):1795–1798.

Wapenaar, K. (2007). General representations for wavefield modeling and inversion in geophysics. *Geophysics*, 72(5):SM5–SM17.

Wapenaar, K., Broggini, F., Slob, E., and Snieder, R. (2013). Three-dimensional single-sided marchenko inverse scattering, data-driven focusing, greens function retrieval, and their mutual relations. *Physical Review Letters*, 110(8):084301.

Wapenaar, K. and Douma, H. (2012). A unified optical theorem for scalar and vectorial wave fields. *The Journal of the Acoustical Society of America*, 131(5):3611–3626.

Wapenaar, K. and Fokkema, J. (2006). Greens function representations for seismic interferometry. *Geophysics*, 71(4):SI33–SI46.

Wapenaar, K., Thorbecke, J., van der Neut, J., Broggini, F., Slob, E., and Snieder, R. (2014a). Green's function retrieval from reflection data, in absence of a receiver at the virtual source position. *The Journal of the Acoustical Society of America*, 135(5):2847–2861.

Wapenaar, K., Thorbecke, J., Van Der Neut, J., Broggini, F., Slob, E., and Snieder, R. (2014b). Marchenko imaging. *Geophysics*, 79(3):WA39–WA57.

White, J. E., Mihailova, N., and Lyakhovitsky, F. (1975). Low-frequency seismic waves in fluid-saturated layered rocks. *The Journal of the Acoustical Society of America*, 57(S1):S30–S30.

Willis, J. R. (1981). Variational and related methods for the overall properties of composites. *Advances in applied mechanics*, 21:1–78.

Zeller, R. and Dederichs, P. (1973). Elastic constants of polycrystals. *Physica status solidi (b)*, 55(2):831–842.

Zhu, T. and Harris, J. M. (2014). Modeling acoustic wave propagation in heterogeneous attenuating media using decoupled fractional laplacians. *Geophysics*, 79(3):T105–T116.

Zhubayev, A. (2014). Soil properties from seismic intrinsic dispersion.

Appendices

Appendix A

Operator, Tensor and Index Notations

Through this work Operators, Tensor and Index Notations are heavily referenced. They are briefly explained below in the Hook's law example for a lossless medium. Using the operator notation, the stress-strain relationship can be written as:

$$\boldsymbol{\sigma} = \mathbf{C}\boldsymbol{\epsilon} \tag{A-1}$$

At the same time, the stress-strain relationship can be written using the index or Einstein notation:

$$\sigma_{ij} = C_{ijkl}\epsilon_{kl} \tag{A-2}$$

Operator and index notations are widely used in geophysical literature. On the other hand, it can be written using the tensor notation:

$$\boldsymbol{\sigma} = \mathbf{C} : \boldsymbol{\epsilon}, \tag{A-3}$$

where : is the double dot product. The tensor notation is popular in micromechanics, mechanics of composites etc. The dyadic basis is defined as $a_i \otimes a_j$. Thus, by definition the stress and strain tensors are:

$$\boldsymbol{\sigma} = \sigma_{ij}\ a_i \otimes a_j \tag{A-4}$$

$$\boldsymbol{\epsilon} = \epsilon_{kl}\ a_k \otimes a_l \tag{A-5}$$

Similarly, the stiffness tensor is:

$$\mathbf{C} = C_{ijkl}\ a_i \otimes a_j \otimes a_k \otimes a_l \tag{A-6}$$

Therefore, the stress-strain relationship can be written as:

$$\begin{gathered}\boldsymbol{\sigma} = \mathbf{C} : \boldsymbol{\epsilon} = \\ = (C_{ijkl}\ a_i \otimes a_j \otimes a_k \otimes a_l) : (\epsilon_{pm}\ a_p \otimes a_m) = \\ = C_{ijkl}\epsilon_{pm}\ a_i \otimes a_j\ \delta_{kp}\ \delta_{lm} = \\ = C_{ijkl}\epsilon_{kl}\ a_i \otimes a_j\end{gathered} \tag{A-7}$$

Appendix B

MATLAB Codes for the T-matrix Method

Below, are some codes which were written to calculate the homogenized viscoelastic properties of rocks (equations (5-18)-(5-23)). Tensors $\widehat{\widehat{\boldsymbol{\mathcal{G}}}}^{(r)}$ and $\widehat{\widehat{\boldsymbol{\mathcal{G}}}}^{(rs)}$ (chapter 5) can be calculated by using Eq. (5-21) or Eq. (5-22) (these codes are not shown here for brevity's sake). Analytical formulas can be found in Torquato (2002) and Jakobsen and Johansen (2005). Formulas for numerical calculation can be found in Mura (1982) and Bayuk et al. (2007). Some codes for other routine operations are not shown for brevity's sake. They can be found in any book on tensor algebra. Zener model can be found in Mavko et al. (2009) and Carcione (2014).

B-1 The T-matrix

```
function [ Ceff_T, pm, Porosity_m ] = ...
    T_matrix_math(vpm,vsm,rhm,vpi,vsi,rhi, alpha ,fi, alpha_rs, F)

% [ Ceff_T, pm, Porosity_m ] = ...
%   T_matrix_math(vpm,vsm,rhm,vpi,vsi,rhi, alfa ,fi, alfa_rs)
% Calculate the effective stiffness tensor using the T-matrix method
%
%
% Inputs:
%   vpm:  P-wave velocity of the rock's matrix
%   vsm:  S-wave velocity of the rock's matrix
%   rhm:  Density
%   vpi:  P-wave velocity of the inclusions in the rock
%   vsi:  S-wave velocity of the inclusions in the rock
%   rhi:  Density of the inclusions
%   alpha: the aspect ratio of the inclusions
%   fi:   porosity (fraction)
%   alpha_rs: the aspect ratio of the inclusions of the two-point
%   correlation function (which takes into account
%   the spatial distribution
%   of the inclusions). This is the second term in the Dyson series.
%   (see Jakobsen et al. (2003) and Alkhimenkov (2017))
%   F - is the connectivity of inclusions (from 0 to 1)
%
%
% Outputs:
%   Ceff_T:    The effective stiffness tensor of the composite material
%   (6*6 matrix, Voigt notation)
%   pm:        Density of the composite material
%   Porosity_m: Porosity of the composite material
```

```
%Written by Y. Alkhimenkov, TU Delft, 2017.


%%
Porosity_m=fi*100;
F=0.5;
pm = (1.0-fi)*rhm + fi*rhi ;
%% Calculating Lame constants of the matrix

Mum=rhm*(vsm.^2);
Lam=rhm*(vpm.^2) - 2*Mum;
Km=Lam+2*Mum/3;

% creating 6*6 matrix
C_matr(1,1) = Lam+2*Mum;
C_matr(1,2) = Lam;
C_matr(1,3) = Lam;
C_matr(2,2) = Lam+2*Mum;
C_matr(2,3) = Lam;
C_matr(3,3) = Lam+2*Mum;
C_matr(4,4) = Mum;
C_matr(5,5) = Mum;
C_matr(6,6) = Mum;
      for i=1:6
         for j=i:6
       C_matr(j,i) = C_matr(i,j);
         end
      end
C_matr1=C_matr;

%% Calculating Lame constants of the inclusions

Mui=rhi*vsi.^2;
Lai=rhi*vpi.^2 - 2*Mui;
Ki=Lai+2*Mui/3;

% Creating 6*6 matrix
C_incl(1,1) = Lai+2*Mui;
C_incl(1,2) = Lai;
C_incl(1,3) = Lai;
C_incl(2,2) = Lai+2*Mui;
C_incl(2,3) = Lai;
C_incl(3,3) = Lai+2*Mui;
C_incl(4,4) = Mui;
C_incl(5,5) = Mui;
C_incl(6,6) = Mui;
      for i=1:3
         for j=i:3
       C_incl(j,i) = C_incl(i,j);
         end
      end

%%
format long
%%
% Comparison body with F
 C_compar1=(1-F)*C_matr+F*C_incl; %

% Calculating Lame constants of the comparison body
Muc=C_compar1(4,4);
Lac=C_compar1(1,2);
nu_c=Lac/(2*(Lac+Muc)) ;


%% Another comparison body:
%
% K_Voigt=(1-fi).*Km+fi*Ki;            % Voigt bound
% K_Reuss=1./((1-fi)./Km+fi./Ki);      % Reuss bound
% Mu_Voigt=(1-fi).*Mum+fi*Mui;         % Voigt bound
% Mu_Reuss=1./((1-fi)./Mum+fi./Mui);   % Reuss bound
%
% Lac_2MucP(1,1) = fi.*(K_Reuss+4./3*Mu_Reuss)+(1-fi).*...
%(K_Voigt+4./3*Mu_Voigt);
% MucP(4,4) = fi.*Mu_Reuss+(1-fi).*Mu_Voigt;
%
% % creating 6*6 matrix
% C_compar1(1,1) = Lac_2MucP(1,1);
% C_compar1(1,2) = Lac_2MucP(1,1)-2*MucP(4,4);
% C_compar1(1,3) = Lac_2MucP(1,1)-2*MucP(4,4);
% C_compar1(2,2) = Lac_2MucP(1,1);
% C_compar1(2,3) = Lac_2MucP(1,1)-2*MucP(4,4);
% C_compar1(3,3) = Lac_2MucP(1,1);
% C_compar1(4,4) = MucP(4,4);
% C_compar1(5,5) = MucP(4,4);
% C_compar1(6,6) = MucP(4,4);
%       for i=1:3
%          for j=i:3
%        C_compar1(j,i) = C_compar1(i,j);
%          end
%       end
```

```
% Muc=C_compar1(4,4);
% Lac=C_compar1(1,2);
% nu_c=Lac/(2*(Lac+Muc)) ;
%% Calculating the Eshely tensor (external function)
% Can be easily written, see Mura (1982).
%
Eshelby2  = Eshelby_math_my(alpha,  nu_c );
C_compar1_ob=Sijkl_cmn(inv(C_compar1));
Eshelby2_4=cijkl_cmn(Eshelby2);

% Calculating the singular component of the Green's tensor
% second derivative over the inclusion volume
% Can be easily written, see Mura (1982).
Gr4=-double_dot_product(Eshelby2_4,C_compar1_ob);
Gr2=Smn_cijkl(Gr4);
%% Some external functions:
% These functions can be easily written, see any book on Tensor Algebra
% They are not shown in the Appendix.

%[ C ] = Smn_cijkl( CC ) % the 4th rank compliance tensor  (3*3*3*3)
% to the Voigt matrix   (6*6)

%[ CC ] = Sijkl_cmn( C ) % the Voigt matrix   (6*6) to
% the 4th rank compliance tensor  (3*3*3*3)

%[ C ] = cmn_cijkl( CC ) % the 4th rank stiffness tensor  (3*3*3*3)
% to the Voigt matrix   (6*6)

%[ CC ] = cijkl_cmn( C ) % the Voigt matrix   (6*6) to
% the 4th rank stiffness tensor (3*3*3*3)


%% External function: double_dot_product
%[ W ] = double_dot_product( C1, C2 ) % double dot product,
%4th order tensors

%% kronecker delta
KrDel = [ 1 0 0 ; ...
          0 1 0 ; ...
          0 0 1 ] ;
%% the 4th rank Identity tensor
I4=zeros(3,3,3,3);
for j=1:1:3
    for k=1:1:3
        for l=1:1:3
            for m=1:1:3
                I4(j,k,l,m)=0.5*(KrDel(j,l)*KrDel(k,m)+KrDel(j,m)...
                    *KrDel(k,l))+I4(j,k,l,m);
            end
        end
    end
end
%% Some routine operations:

Gr4i=Sijkl_cmn(Gr2);
dCr2i=C_incl-C_compar1;
dCr4i=cijkl_cmn(dCr2i);

trr1i=double_dot_product(dCr4i,Gr4i);
ttr2i=I4-trr1i;
ttr2_obi=cijkl_cmn(inv(Smn_cijkl(ttr2i)));
ttr3i=double_dot_product(ttr2_obi,dCr4i);

Gr4m=Sijkl_cmn(Gr2);
dCr2m=C_matr-C_compar1; %
dCr4m=cijkl_cmn(dCr2m);

trr1m=double_dot_product(dCr4m,Gr4m);
ttr2m=I4-trr1m;
ttr2_obm=cijkl_cmn(inv(Smn_cijkl(ttr2m)));
ttr3m=double_dot_product(ttr2_obm,dCr4m);

%%
% Calculating the singular component of the Green's tensor
% second derivative over the inclusion volume using the
% aspect ratio of the two-point correlation function

Eshelby2  = Eshelby_math_my( alpha_rs,  nu_c );
C_matr4_ob=Sijkl_cmn(inv(C_compar1));
Eshelby2_4_rs=cijkl_cmn(Eshelby2);
Gr4_rs=-double_dot_product(Eshelby2_4_rs,C_matr4_ob);
Gr2_rs=Smn_cijkl(Gr4_rs);
Gr4_rs=Sijkl_cmn(Gr2_rs);
Gr4___RS=Smn_cijkl(Gr4_rs);

%% Again some routine operations:

X1i=double_dot_product(Gr4_rs,ttr3i); %           11
X2i=double_dot_product(ttr3i,X1i);
```

```
X12i=double_dot_product(Gr4_rs,ttr3m);%             12
X1212=double_dot_product(ttr3i,X12i);

X1m21=double_dot_product(Gr4_rs,ttr3i);%           21
X2121=double_dot_product(ttr3m,X1m21);

X1m=double_dot_product(Gr4_rs,ttr3m);%           22
X2m=double_dot_product(ttr3m,X1m);

X1=fi*(X2i*fi);
X12=fi*(X1212*(1-fi));
X21=(1-fi)*X2121*fi;
X4=(1-fi)*(X2m*(1-fi));
X=-(fi*(X2i*fi)+fi*(X1212*(1-fi))+(1-fi)*X2121*fi + (1-fi)*(X2m*(1-fi)));

T1=fi*ttr3i+(1-fi)*ttr3m;
T1_ob=Sijkl_cmn(inv(cmn_cijkl(T1)));
C1i=double_dot_product(T1_ob,X);
C2i=I4-C1i;
C3i_ob=cijkl_cmn(inv(Smn_cijkl(C2i)));

C4i=double_dot_product(T1,C3i_ob);

Ceff_T12=cijkl_cmn(C_compar1)+C4i;
Ceff_T=cmn_cijkl(Ceff_T12)  ;  % the effective stiffness tensor

disp('The T-matrix');
```

B-2 The Double Dot Product

```
function [ W ] = double_dot_product( C1, C2 )
%function [ W ] = double_dot_product( C1, C2 )
%double dot product, 4th order tensors
% Inputs:
% C1, C2: two 4th rank tensors  1(3*3*3*3),  2(3*3*3*3)
%
% Outputs:
% W: double dot product, the 4th rank tensors W(3*3*3*3)

W = zeros(3,3,3,3);

 for i=1:3
     for j=1:3
          for m=1:3
              for n=1:3
                  for k=1:3
                         for l=1:3
                         W(i,j,m,n)=C1(i,j,k,l)*C2(k,l,m,n)+W(i,j,m,n);
                         end
                    end
              end
          end
    end
 end

end
```

Appendix C

Models: Tables 1-3

$z_{top}(m)$	$z_{bottom}(m)$	$V_p(km/s)$	$\rho(kg/m^3)$	$\zeta_{damping}$	$Q_{temporal}$
0	750	2000	1000	0.8	≈ 117.8
750	1500	2000	2000	0.8	≈ 117.8
1500	2375	2000	1000	0.8	≈ 117.8
2375	3000	2000	2000	0.8	≈ 117.8

Table C-1: A simple constant-Q model (Model 1).

$z_{top}(m)$	$z_{bottom}(m)$	$V_p(km/s)$	$\rho(kg/m^3)$	α_H
0	400	2500	2500	$1.5 \cdot 10^{-3}$
400	1000	3000	2700	$1.5 \cdot 10^{-3}$
1000	1500	2000	2400	$1.5 \cdot 10^{-3}$
1500	2375	3000	2600	$1.5 \cdot 10^{-3}$
2375	3000	2000	2500	$1.5 \cdot 10^{-3}$

Table C-2: De Hoop's model with two parameters (Model 2a).

$z_{top}(m)$	$z_{bottom}(m)$	$V_p(km/s)$	$\rho(kg/m^3)$	α_H
0	400	2500	2500	$3 \cdot 10^{-3}$
400	1000	3000	2700	$3 \cdot 10^{-3}$
1000	1500	2000	2400	$3 \cdot 10^{-3}$
1500	2375	3000	2600	$3 \cdot 10^{-3}$
2375	3000	2000	2500	$3 \cdot 10^{-3}$

Table C-3: De Hoop's model with one parameter (Model 2b).

$z_{top}(m)$	$z_{bottom}(m)$	$V_p(km/s)$	$\rho(kg/m^3)$	α_H
0	400	2500	2500	$1.5 \cdot 10^{-3}$
400	1000	3000	2700	$1.5 \cdot 10^{-3}$
1000	1500	2000	2400	$5.25 \cdot 10^{-3}$
1500	2375	3000	2600	$1.5 \cdot 10^{-3}$
2375	3000	2000	2500	$1.5 \cdot 10^{-3}$

Table C-4: De Hoop's model with two parameters (Model 2c).

$z_{top}(m)$	$z_{bottom}(m)$	$V_p(km/s)$	$\rho(kg/m^3)$	α_H
0	400	2500	2500	$1.5 \cdot 10^{-3}$
400	1000	2800	2700	$1.5 \cdot 10^{-3}$
1300	1500	4000	2690	$1.2 \cdot 10^{-3}$
1500	2375	2650	2700	$1.8 \cdot 10^{-3}$
2600	3000	2200	2500	$1.65 \cdot 10^{-3}$

Table C-5: De Hoop's model with two parameters (Model 3a). The third layer is a carbonate rock with some clay content.

$z_{top}(m)$	$z_{bottom}(m)$	$V_p(km/s)$	$\rho(kg/m^3)$	α_H
0	400	2500	2500	$1.5 \cdot 10^{-3}$
400	1000	2800	2700	$1.5 \cdot 10^{-3}$
1300	1500	2490	2000	$15 \cdot 10^{-3}$
1500	2375	2650	2700	$1.8 \cdot 10^{-3}$
2600	3000	2200	2500	$1.65 \cdot 10^{-3}$

Table C-6: De Hoop's model with two parameters (Model 3b). The third layer represents a reservoir with 20% porosity.

Appendix D

Section 6-1: Figures D-1 - D-6

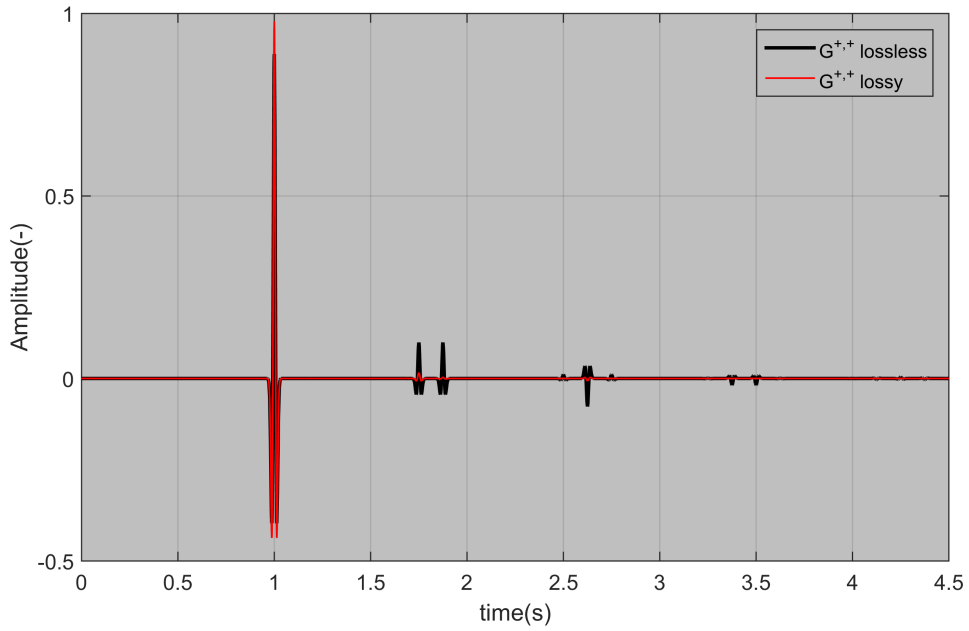

Figure D-1: Downgoing Green's function $G^{+,+}$. Black curve is the lossless $G^{+,+}$, red curve is the lossy $G^{+,+}$. The x-axis represents time in seconds, the y-axis represents the amplitude. The focal point is 2000 m depth. The intrinsic loss was modelled as an amplitude damping (Model 1) $\zeta_{damping} = 0.8$.

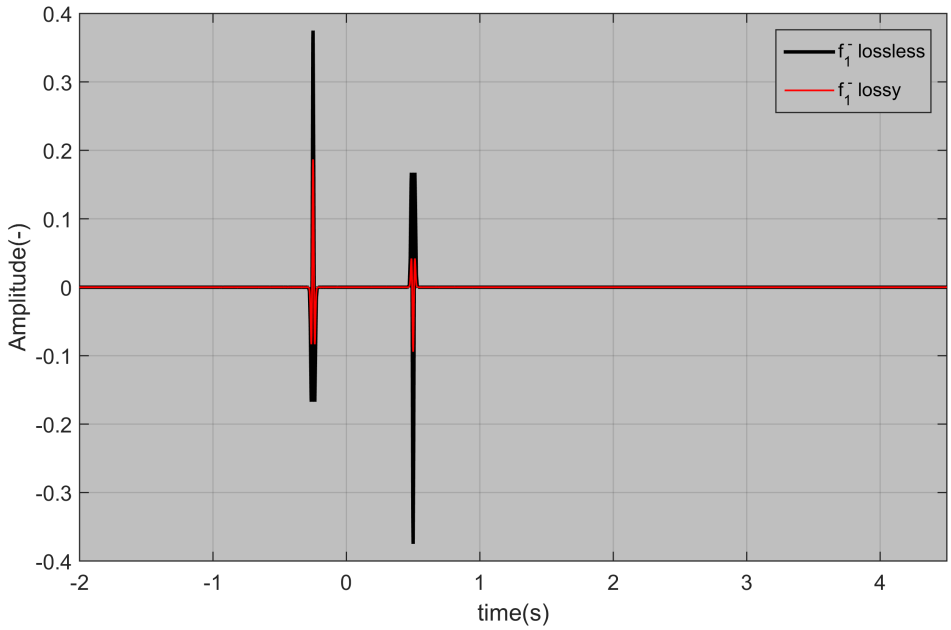

Figure D-2: Upgoing focusing function f_1^-. The black curve is the lossless f_1^- The red curve is the lossy f_1^-. The x-axis represents time in seconds, the y-axis represents the amplitude. The focal point is 2000 m depth. The intrinsic loss was modelled as an amplitude damping (Model 1) $\zeta_{damping} = 0.8$.

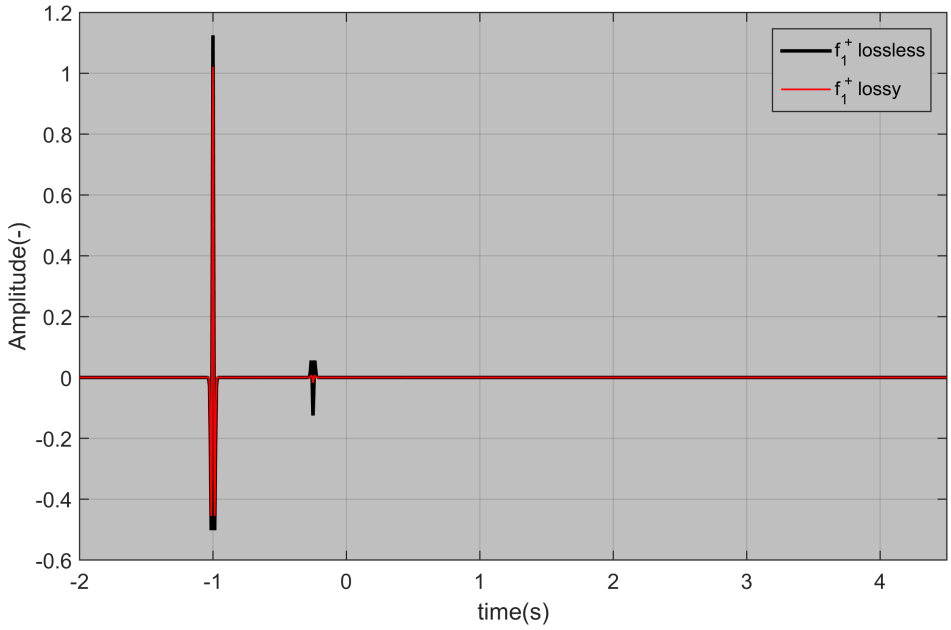

Figure D-3: Downgoing focusing function f_1^+. The black curve is the lossless f_1^+. The red curve is the lossy f_1^+. The x-axis represents time in seconds. The y-axis represents the amplitude. The focal point is 2000 m depth. The intrinsic loss was modelled as an amplitude damping (Model 1) $\zeta_{damping} = 0.8$.

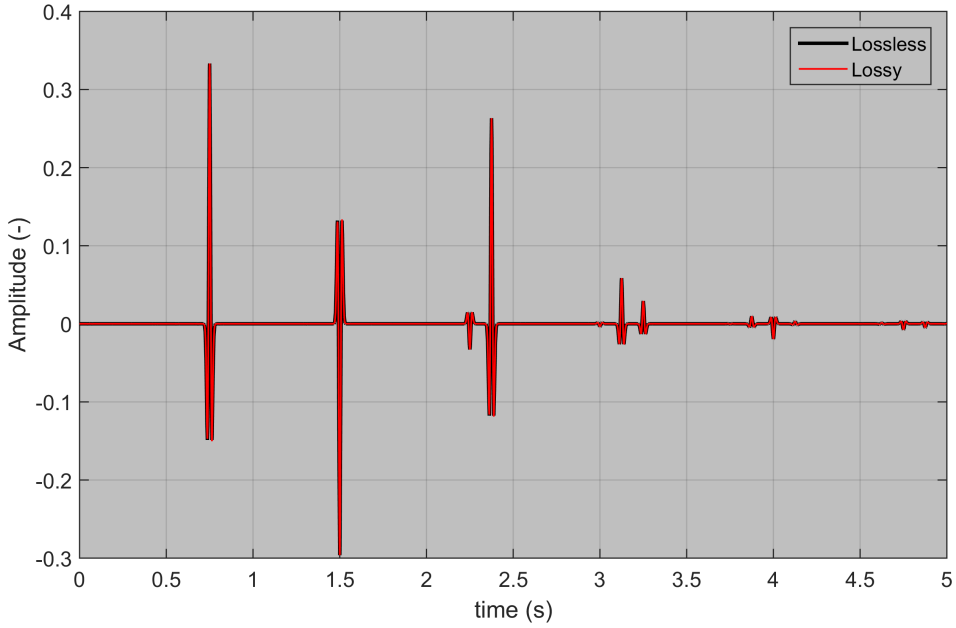

Figure D-4: Lossless (black curve) and compensated lossy (red curve) reflection series for Model 1. The x-axis represents time in seconds. The y-axis represents the amplitude. The intrinsic loss was modelled as an amplitude damping (Model 1). $\zeta_{damping} = 0.8$. The compensation factor is $\zeta_{compensation} = 0.8$

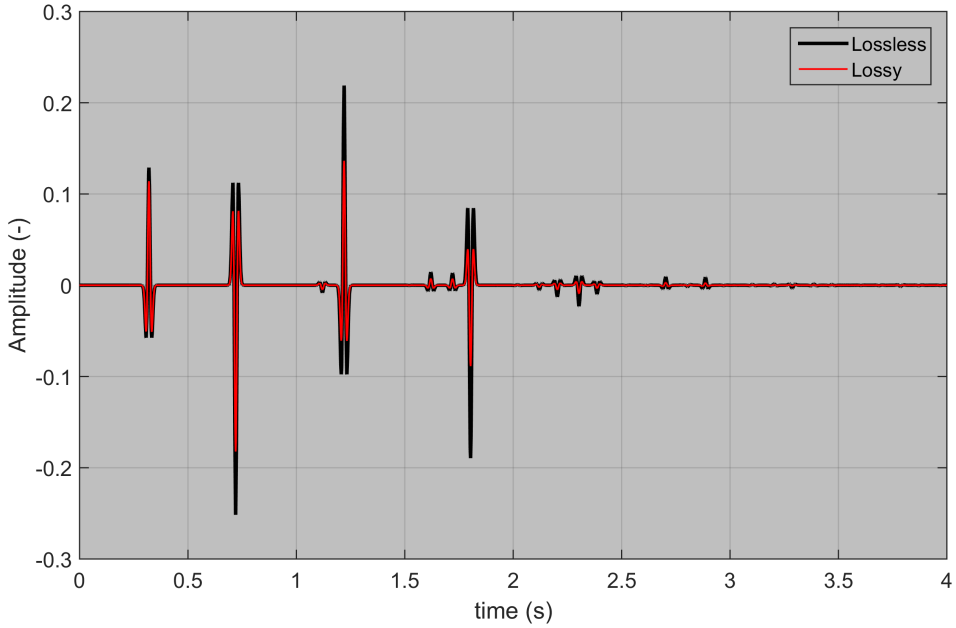

Figure D-5: Lossless (black curve) and lossy (red curve) reflection series for Model 1. The x-axis represents time in seconds, the y-axis represents the amplitude. The intrinsic loss was modelled using De Hoop's model with two parameters (Model 2b).

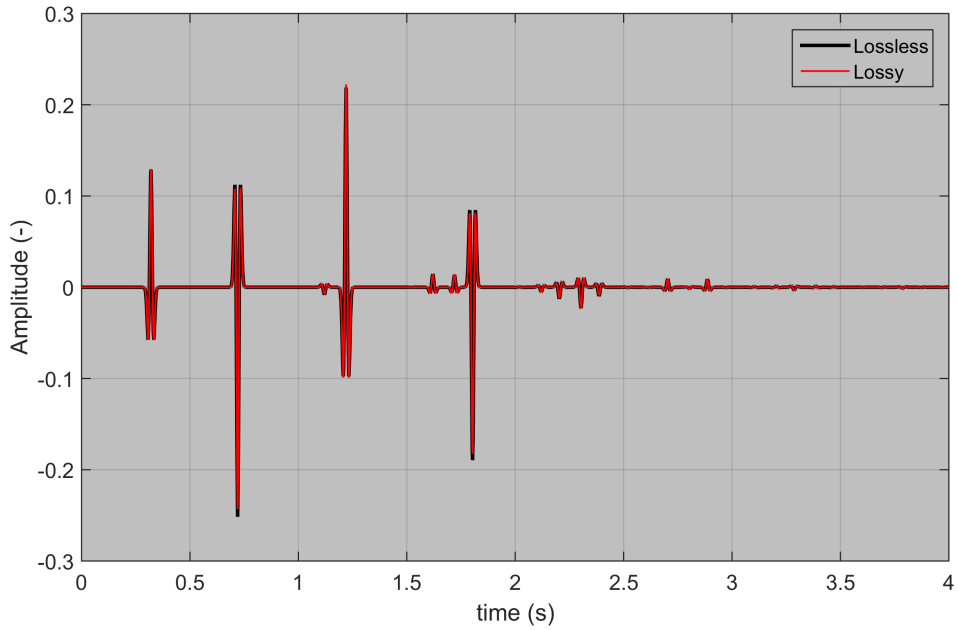

Figure D-6: Lossless (black curve) and compensated lossy (red curve) reflection series for Model 2b. The x-axis represents time in seconds. The y-axis represents the amplitude. The intrinsic loss was modelled using De Hoop's model with two parameters (Model 2b). The compensation factor is $\zeta_{compensation} = 0.5$.

Appendix E

Section 6-2: Figures E-1 - E-15

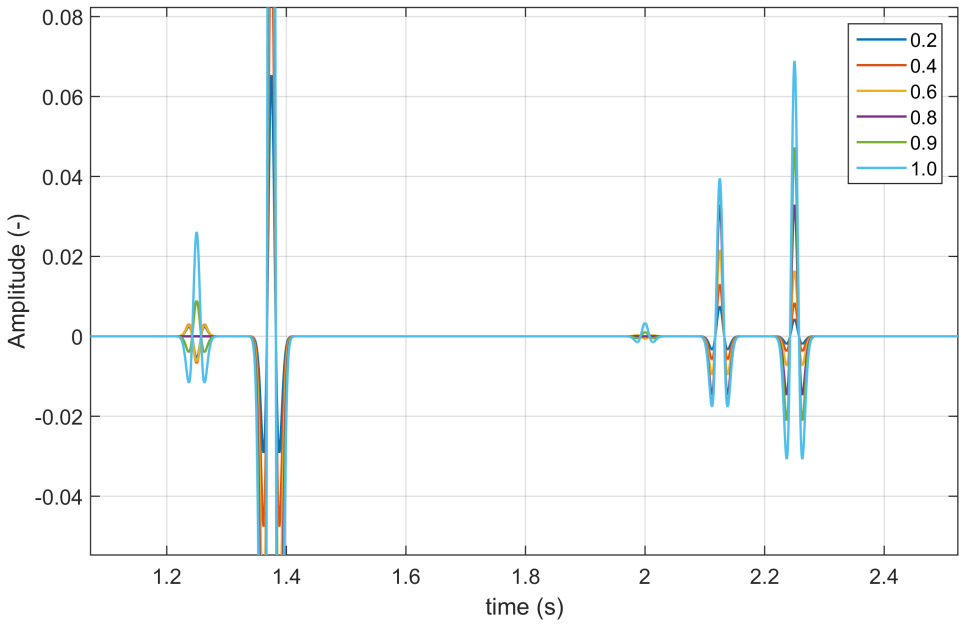

Figure E-1: Upgoing Green's function $G^{-,+}$. The focal point is 2000 m depth. Different colors correspond to different compensation parameters $\zeta_{compensation}$ = 0.2, 0.4, 0.6, 0.8, 0.9, 1.0. The intrinsic loss was modelled as an amplitude damping (Model 1).

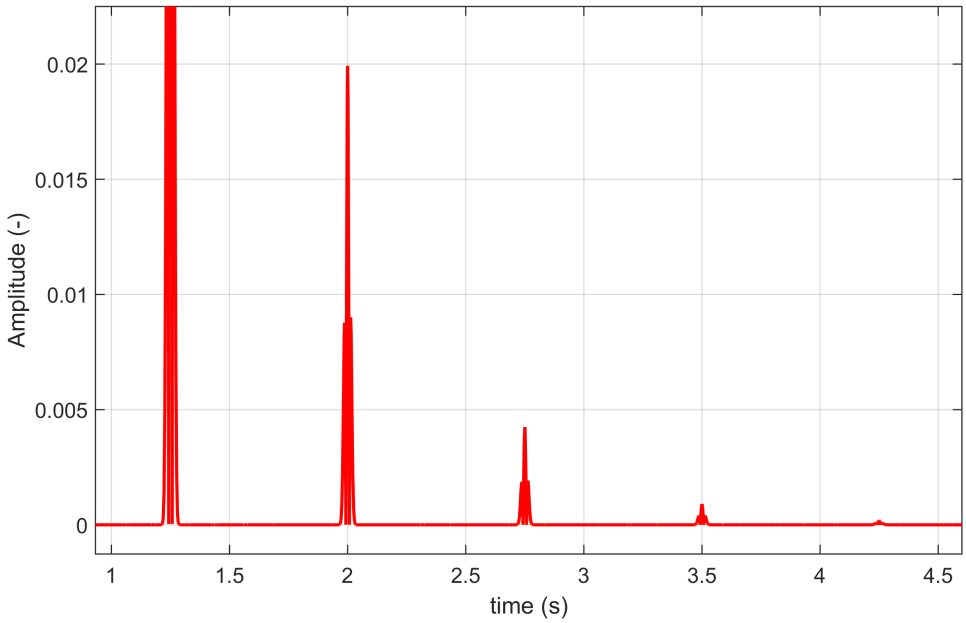

Figure E-2: The function $\mathcal{T}(\mathbf{x}, t)$. This figure is the zoomed version of Figure 6-7. Five artefacts can be seen at 1.25, 2, 2.75, 3.5, 4.25 seconds. The intrinsic loss was modelled as an amplitude damping (Model 1).

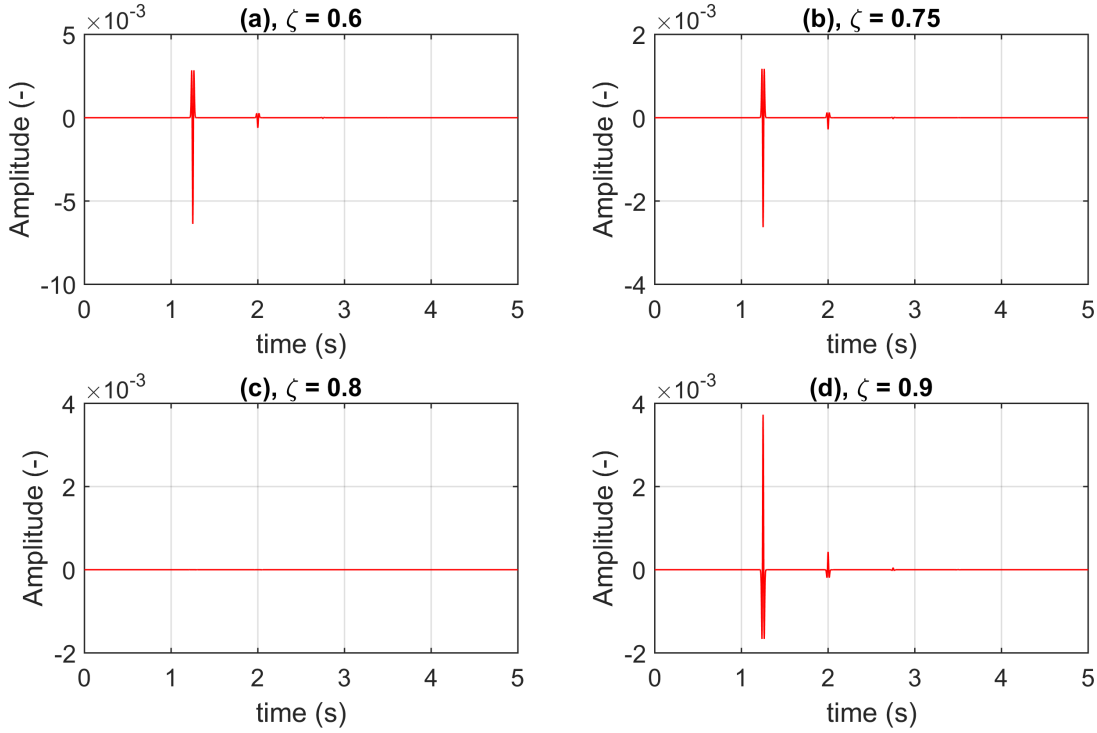

Figure E-3: Function $\mathcal{T}_G^i(\mathbf{x}, t_l)$ which is equal to the upgoing Green's function $G^{-,+}$ at time intervals where artefacts are present. $G^{-,+}$ was calculated using different compensation parameters applied to the lossy reflection series: (a) - $\zeta_{compensation} = 0.6$; (b) - $\zeta_{compensation} = 0.75$; (c) - $\zeta_{compensation} = 0.8$, this is the correct value, therefore, no artefacts are present; (d) - $\zeta_{compensation} = 0.9$. The x-axis represents time in seconds. The y-axis represents the amplitude.

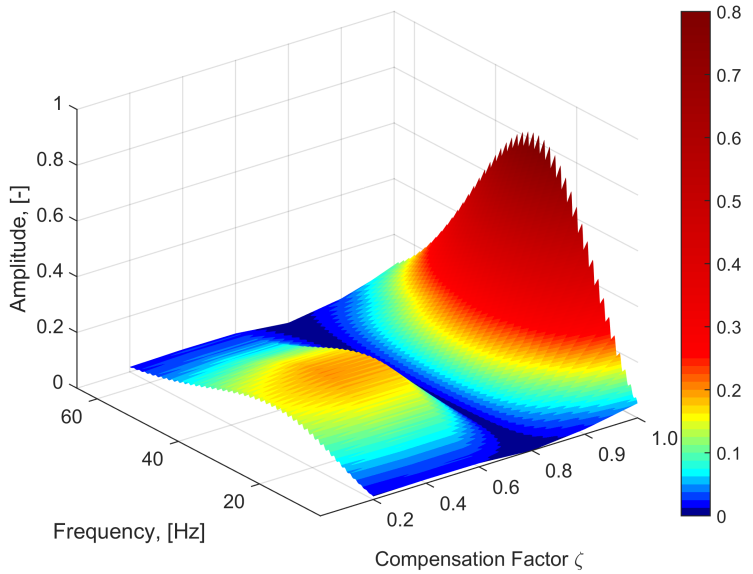

Figure E-4: Function $\widehat{\mathcal{T}}_G^i(\mathbf{x}, \omega)$. The horizontal plane is the compensation parameter $\zeta_{compensation}$ = 0.2, 0.4, 0.6, 0.8, 0.9, 1.0 and the frequency. The vertical axis corresponds to the amplitude. The true compensation parameter is $\zeta_{compensation} = 0.8$ corresponds to the minimum of $\widehat{\mathcal{T}}_G^i(\mathbf{x}, \omega)$ which is shown in blue.

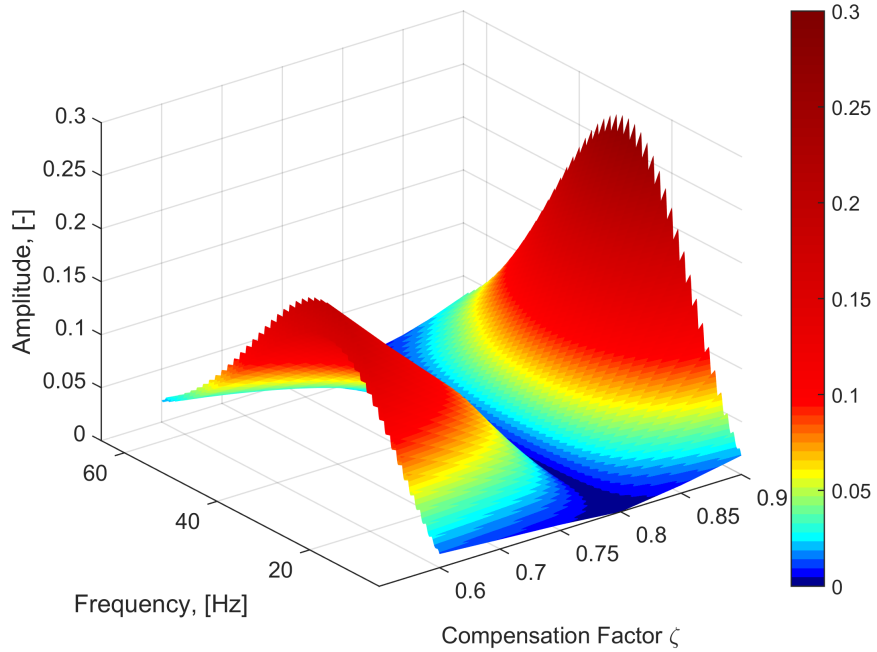

Figure E-5: Function $\widehat{\mathcal{T}}_G^i(\mathbf{x}, \omega)$. The horizontal plane is the compensation parameter $\zeta_{compensation}$ = 0.6, 0.7, 0.75, 0.8, 0.85, 0.9 and the frequency. The vertical axis corresponds to the amplitude. The true compensation parameter is $\zeta_{compensation} = 0.8$ corresponds to the minimum of $\widehat{\mathcal{T}}_G^i(\mathbf{x}, \omega)$.

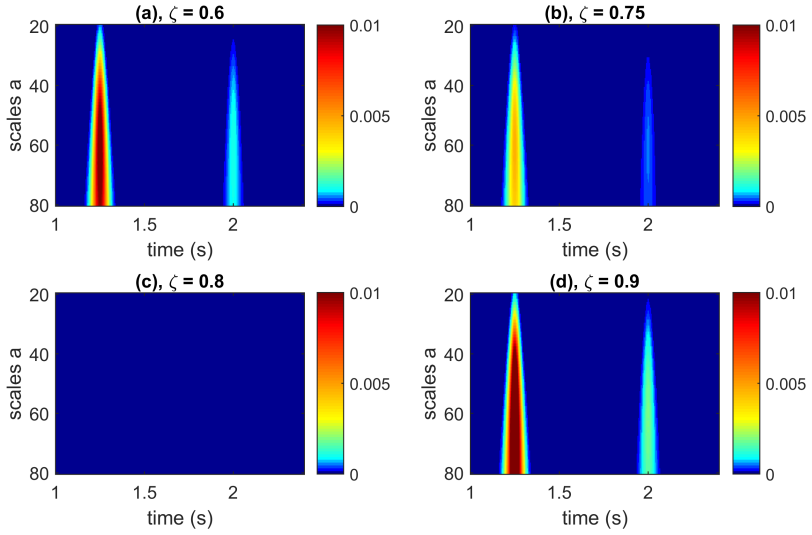

Figure E-6: The continuous 1D wavelet transform of the function $\mathcal{T}_G^i(\mathbf{x}, t_l)$ using the Morlet wavelet with scales 20-80. The x-axis represents time in seconds. The y-axis represents scale a. The color represents the coefficient value. (a) $\zeta_{compensation} = 0.6$; (b) $\zeta_{compensation} = 0.75$; (c) $\zeta_{compensation} = 0.8$, this is the correct value, therefore, nothing is visible; (d) $\zeta_{compensation} = 0.9$.

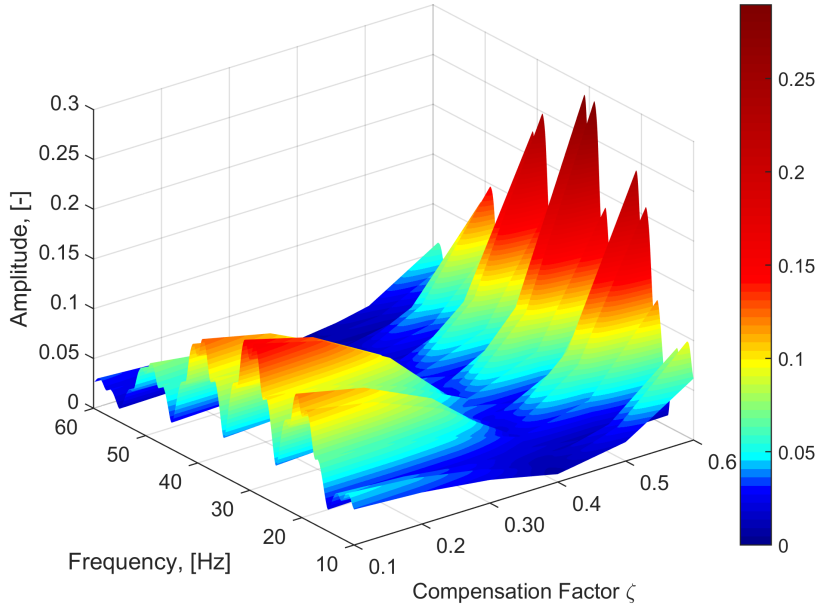

Figure E-7: Function $\widehat{\mathcal{T}}_G^i(\mathbf{x},\omega)$. The x-axis represents the compensation parameter $\zeta_{compensation}$ = 0.1, 0.2, 0.3, 0.4, 0.5, 0.6. The y-axis represents the frequency. The vertical axis corresponds to the amplitude. The true compensation parameter is around $\zeta_{compensation} = 0.4$, which corresponds to the minimum of $\widehat{\mathcal{T}}_G^i(\mathbf{x},\omega)$. The intrinsic loss was modelled using De Hoop's Model with Two Parameters (Model 2a).

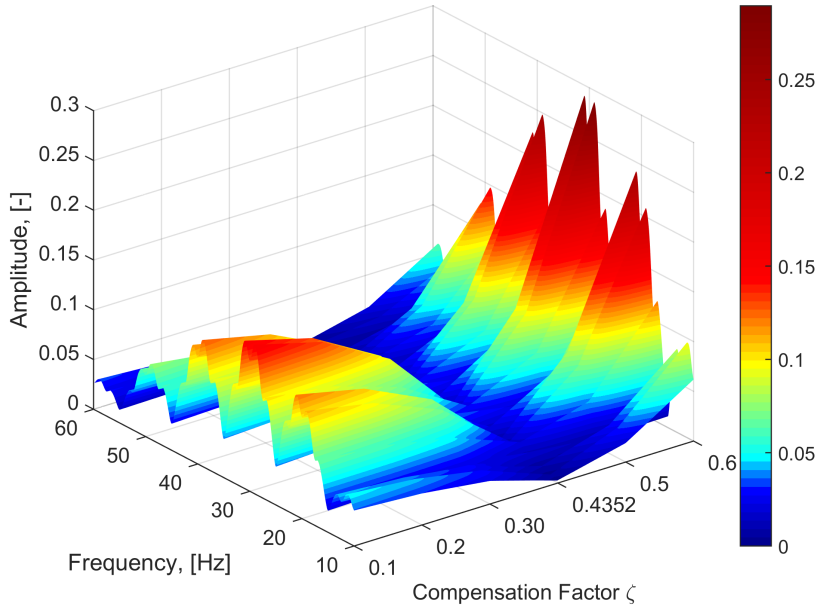

Figure E-8: Function $\widehat{\mathcal{T}}_G^i(\mathbf{x},\omega)$. The x-axis represents the compensation parameter $\zeta_{compensation}$ = 0.1, 0.2, 0.3, 0.4352, 0.5, 0.6. The y-axis represents the frequency. The vertical axis corresponds to the amplitude. The true compensation parameter is $\zeta_{compensation} = 0.8$, which corresponds to the minimum of $\widehat{\mathcal{T}}_G^i(\mathbf{x},\omega)$. The intrinsic loss was modelled using De Hoop's Model with Two Parameters (Model 2a).

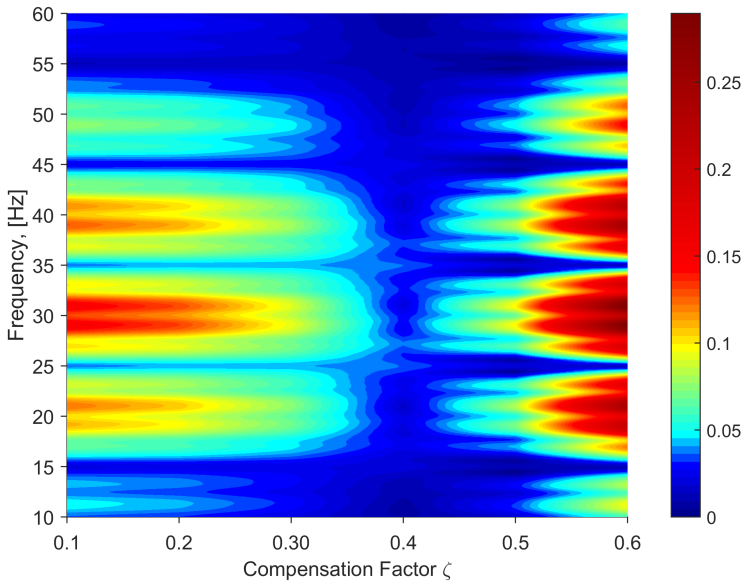

Figure E-9: Function $\mathcal{T}_G^i(\mathbf{x}, t_l)$. This figure is similar to Figure E-7 but instead of a 3D plot this figure is a 2D plot. The x-axis represents the compensation parameter $\zeta_{compensation}$ = 0.1, 0.2, 0.3, 0.4, 0.5, 0.6. The y-axis represents the frequency. The color denotes the amplitude. The true compensation parameter is around $\zeta_{compensation} = 0.4$, which corresponds to the minimum of $\widehat{\mathcal{T}}_G^i(\mathbf{x}, \omega)$ (blue). The intrinsic loss was modelled using De Hoop's Model with Two Parameters (Model 2a).

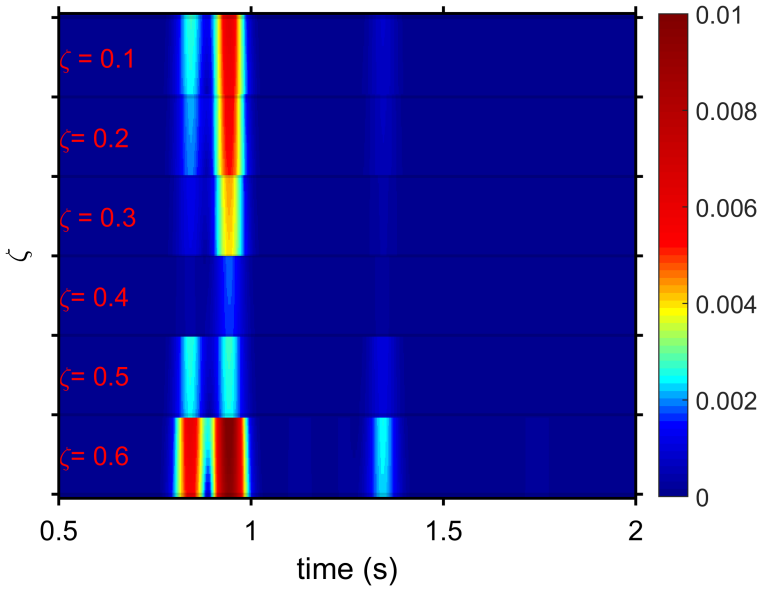

Figure E-10: The continuous 1D wavelet transform of the function $\mathcal{T}_G^i(\mathbf{x}, t_l)$ using the Morlet wavelet. The x-axis represents time in seconds. The y-axis is divided into 6 horizontal bands. Each horizontal band corresponds to a different $\zeta_{compensation}$. Within each horizontal band, scales a = 70-80 are shown. The color represents the coefficient value. The intrinsic loss was modelled using De Hoop's Model with Two Parameters (Model 2a).

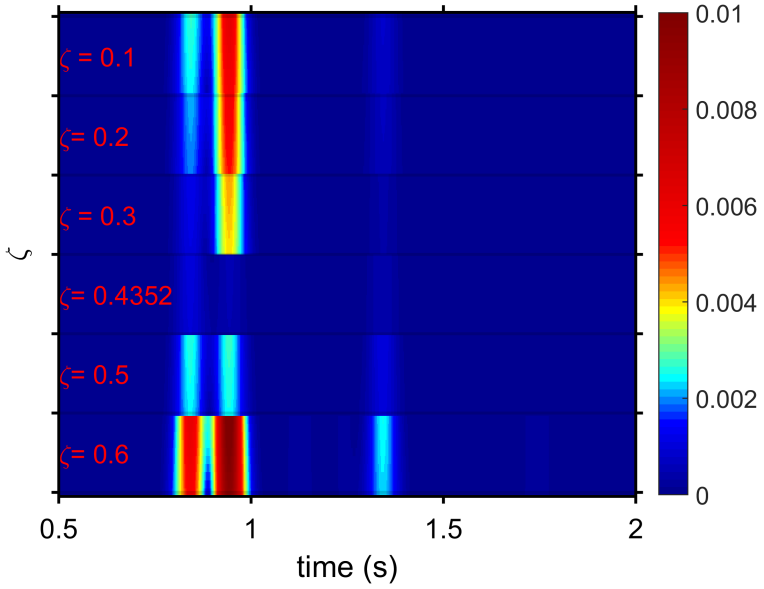

Figure E-11: The continuous 1D wavelet transform of the function $\mathcal{T}_G^i(\mathbf{x}, t_l)$ using the Morlet wavelet. The x-axis represents time in seconds. The y-axis is divided into 6 horizontal bands. Each horizontal band corresponds to a different $\zeta_{compensation}$. Within each horizontal band, scales a = 70-80 are shown. The color represents the coefficient value. $\zeta_{compensation} = 0.4352$ is the correct value, because the amplitude is closer to zero. The intrinsic loss was modelled using De Hoop's Model with Two Parameters (Model 2a).

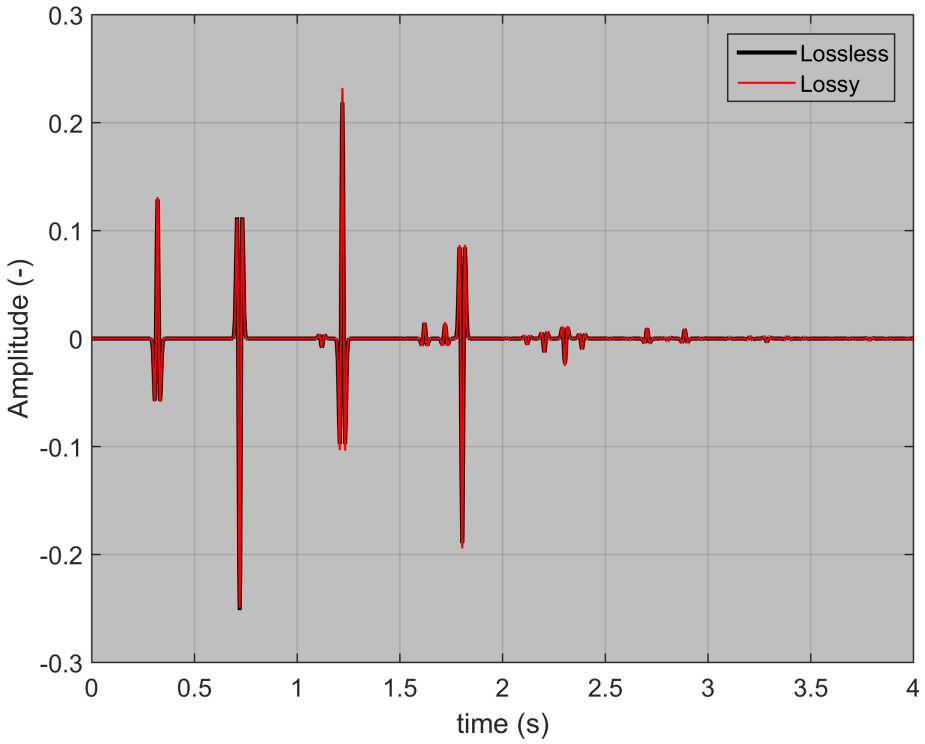

Figure E-12: Lossless (black curve) and compensated lossy (red curve) reflection series for Model 2a. The x-axis represents time in seconds. The y-axis represents the amplitude. The compensation factor is $\zeta_{compensation} = 0.4352$. The intrinsic loss was modelled using De Hoop's Model with Two Parameters (Model 2a).

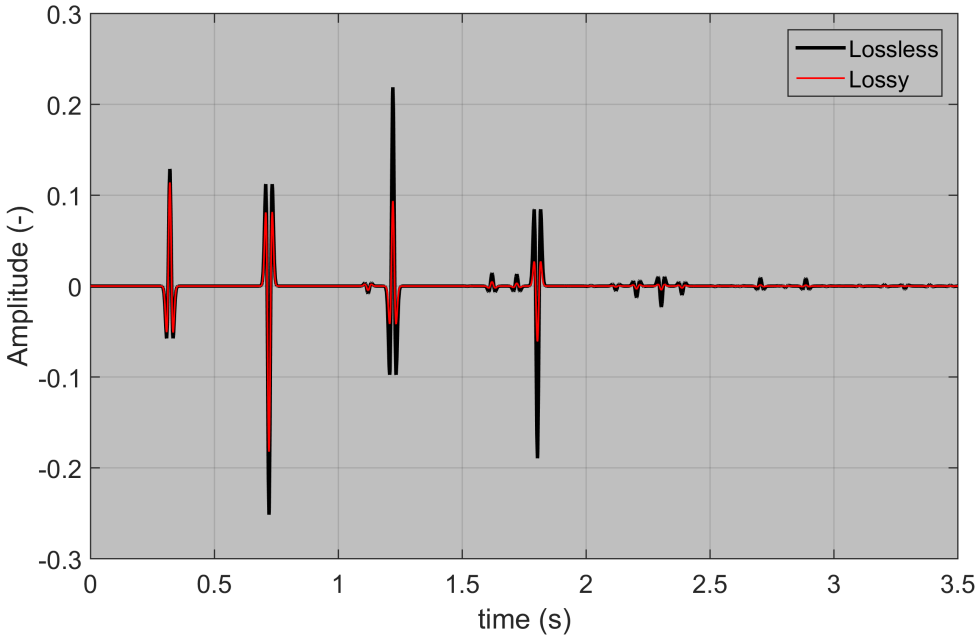

Figure E-13: Lossless (black curve) and lossy (red curve) reflection series for Model 2c. The x-axis represents time in seconds. The y-axis represents the amplitude. The intrinsic loss was modelled using De Hoop's model with two parameters.

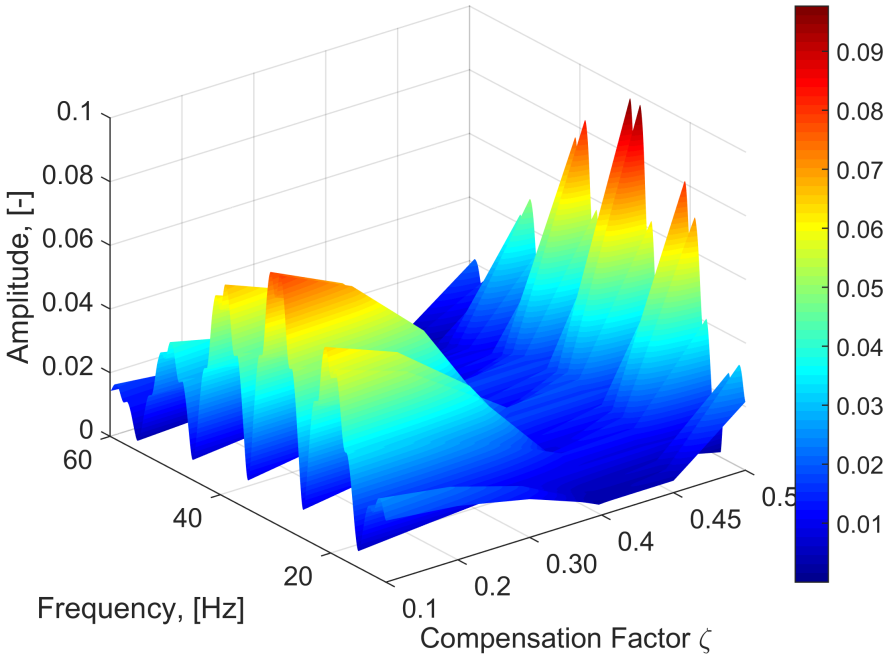

Figure E-14: Function $\widehat{\mathcal{T}}_G^i(\mathbf{x},\omega)$ for Model 2c. The horizontal plane is the compensation parameter $\zeta_{compensation} = 0.1, 0.2, 0.3, 0.4, 0.45, 0.5$ and the frequency. The vertical axis corresponds to the amplitude. The range of $\zeta_{compensation} = 0.4 - 0.45$ corresponds to to the minimum of $\widehat{\mathcal{T}}_G^i(\mathbf{x},\omega)$.

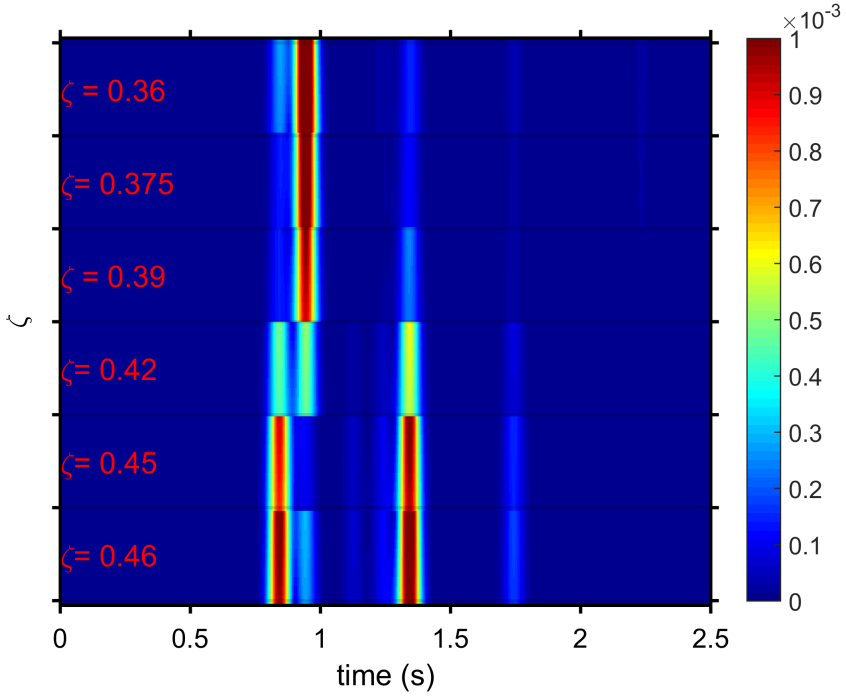

Figure E-15: The continuous 1D wavelet transform of the function $\mathcal{T}_G^i(\mathbf{x}, t_l)$ using the Morlet wavelet (Model 2c). The x-axis represents time in seconds. The y-axis represents scale a. The y-axis is divided into 6 horizontal bands. Each horizontal band corresponds to a different $\zeta_{compensation}$. Within each horizontal band, scales $a =$ 70-80 are shown. The color represents the coefficient value.

Appendix F

Section 6-3: Figures F-1 - F-3

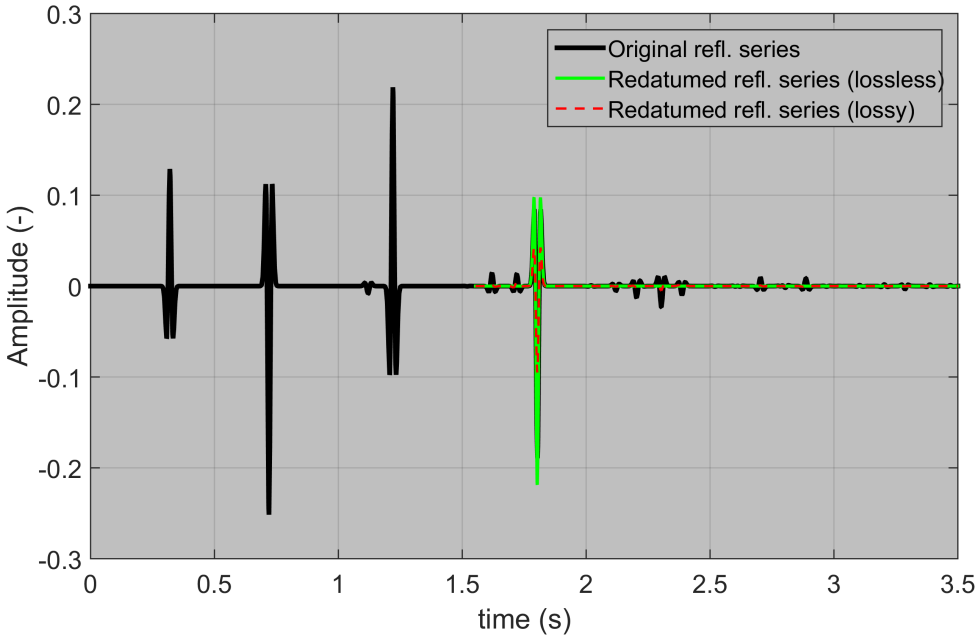

Figure F-1: Reflection response (black), redatumed reflection response using $G^{\pm,+}$ for lossless medium (green) and the redatumed reflection response using $G^{\pm,+}$ for lossy medium. The intrinsic loss was modelled using De Hoop's Model with Two Parameters (Model 2a). The black curve coincides with the green curve at time ≈1.8 sec.

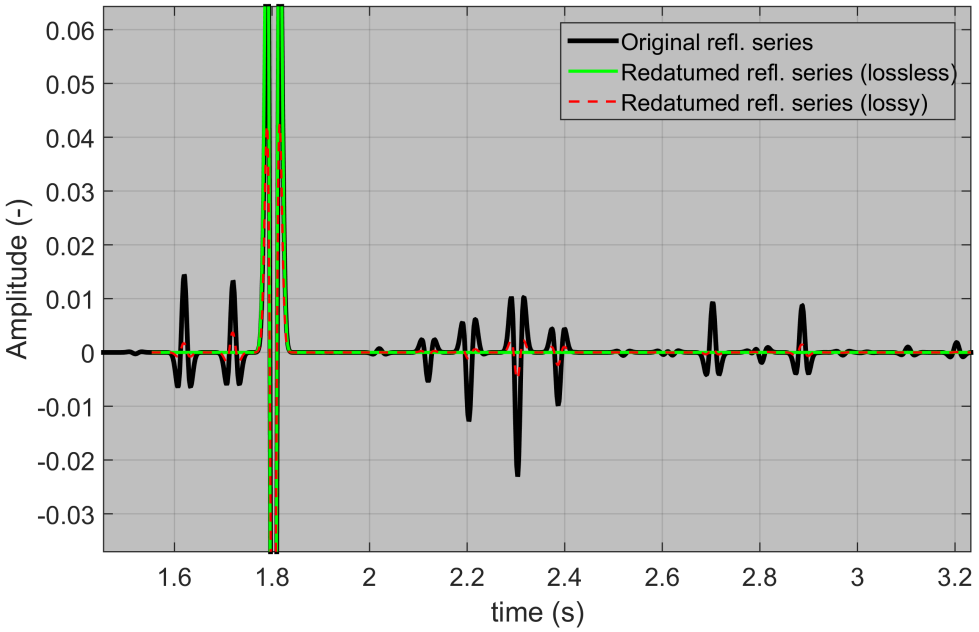

Figure F-2: That is the same figure as Figure 6-14 but zoomed in to 2-4.5 seconds and -0.02-0.04 amplitudes. The intrinsic loss was modelled using De Hoop's Model with Two Parameters (Model 2a). The black curve coincides with the green curve at time ≈1.8 sec.

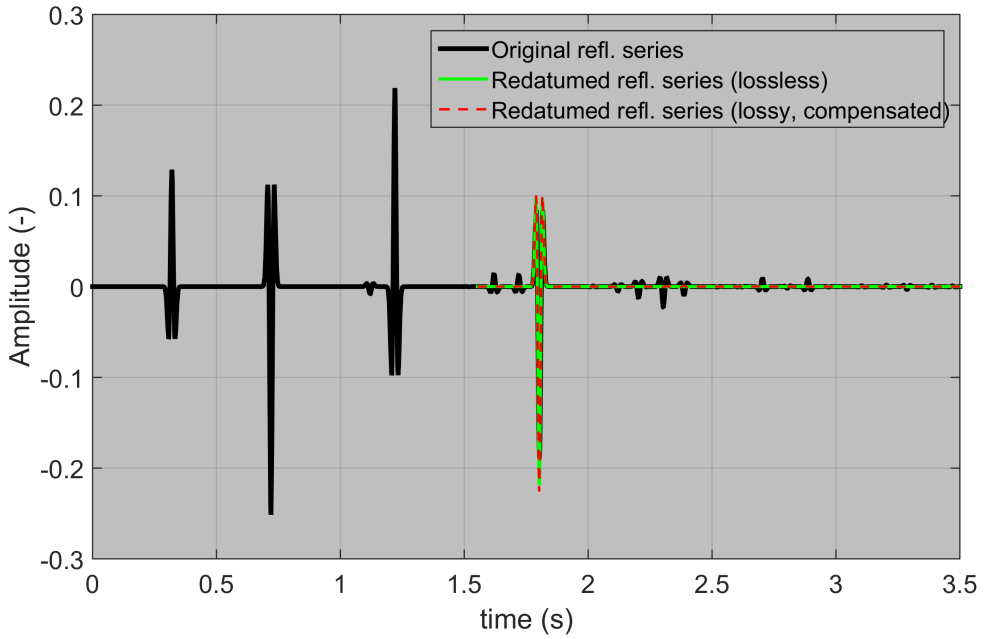

Figure F-3: Black and green curves are the same as in Figure 6-13. The dashed red curve is the redatumed reflection response which was calculated using $G^{\pm,+}$ for compensated lossy medium. The intrinsic loss was modelled using De Hoop's Model with Two Parameters (Model 2a). The black curve coincides with the green curve at time ≈1.8 sec.

Appendix G

Section 7-2: Figures G-1 - G-5

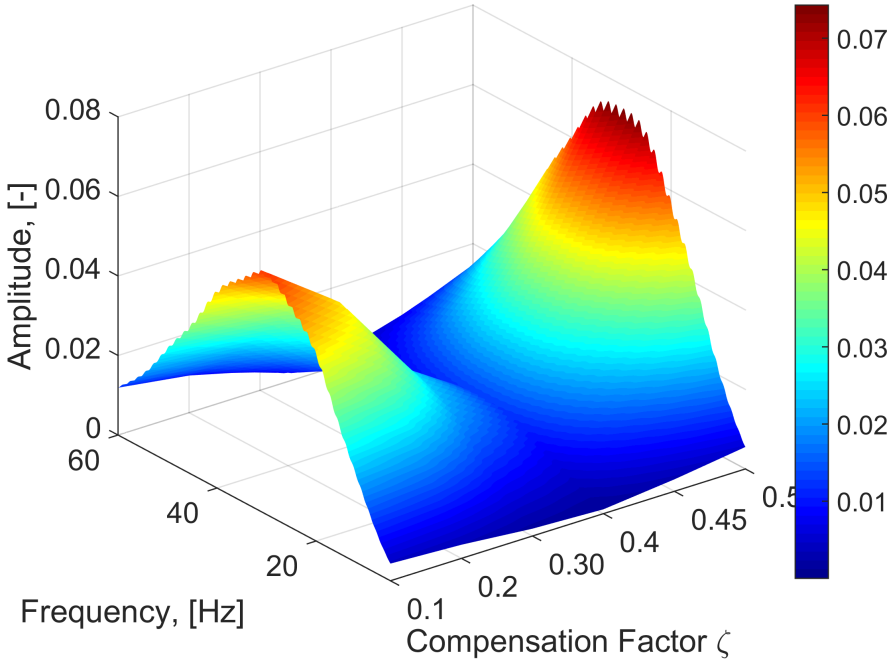

Figure G-1: Function $\widehat{\mathcal{T}}^i_{f1}(\mathbf{x}, \omega)$ for Model 3a. The horizontal plane is the compensation parameter $\zeta_{compensation} = 0.1, 0.2, 0.3, 0.4, 0.45, 0.5$ and the frequency. The vertical axis corresponds to the amplitude. The compensation parameter is $\zeta_{compensation} = 0.4$ corresponds to the minimum of $\widehat{\mathcal{T}}^i_{f1}(\mathbf{x}, \omega)$.

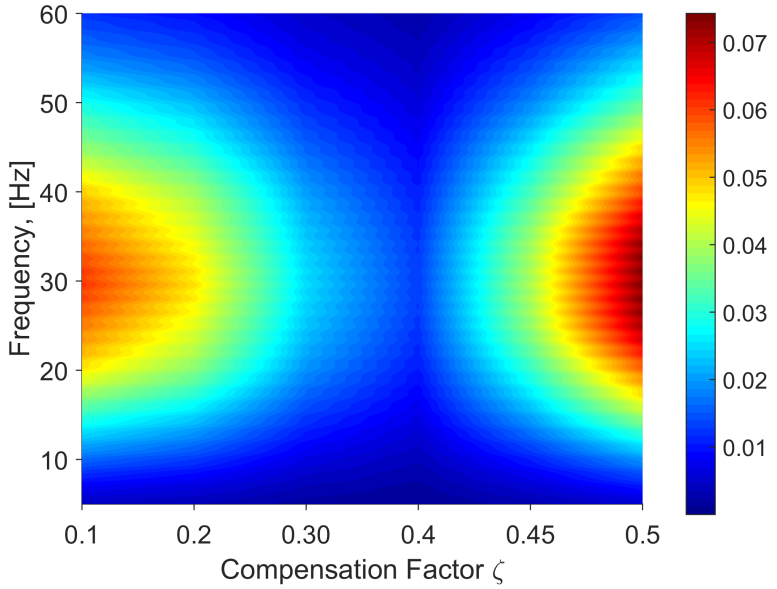

Figure G-2: This figure is similar to Figure G-1 but instead of a 3D plot this figure is a 2D plot. The x-axis represents the compensation parameter $\zeta_{compensation}$ = 0.1, 0.2, 0.3, 0.4, 0.45, 0.5. The y-axis represents the frequency. The color denotes the amplitude. The correct compensation parameter is $\zeta_{compensation} = 0.4$, which corresponds to the minimum of $\widehat{\mathcal{T}}^i_{f1}(\mathbf{x}, \omega)$ (no artefacts).

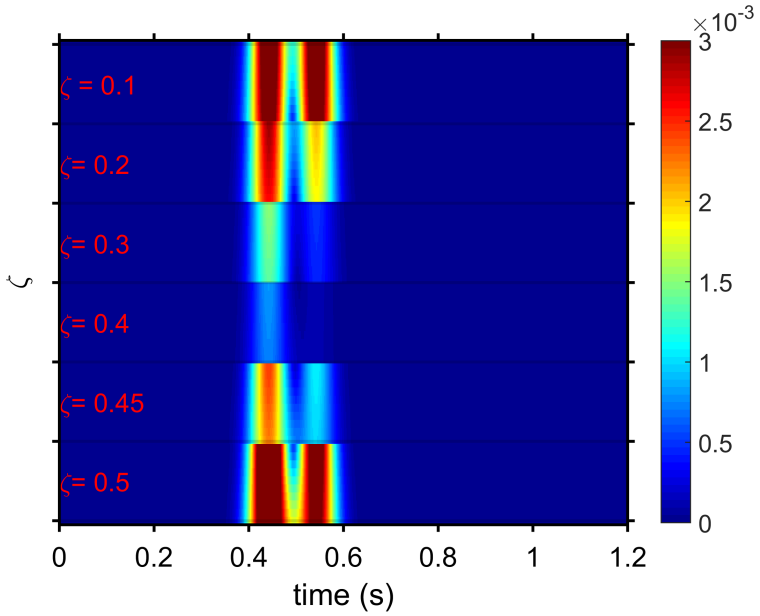

Figure G-3: The continuous 1D wavelet transform of the function $\mathcal{T}^i_{f1}(\mathbf{x}, t_l)$ using the Morlet wavelet (Model 3a). The x-axis represents time in seconds. The y-axis represents scale a. The y-axis is divided into 6 horizontal bands. Each horizontal band corresponds to a different $\zeta_{compensation}$. Within each horizontal band, scales a = 70-80 are shown. The color represents the coefficient value.

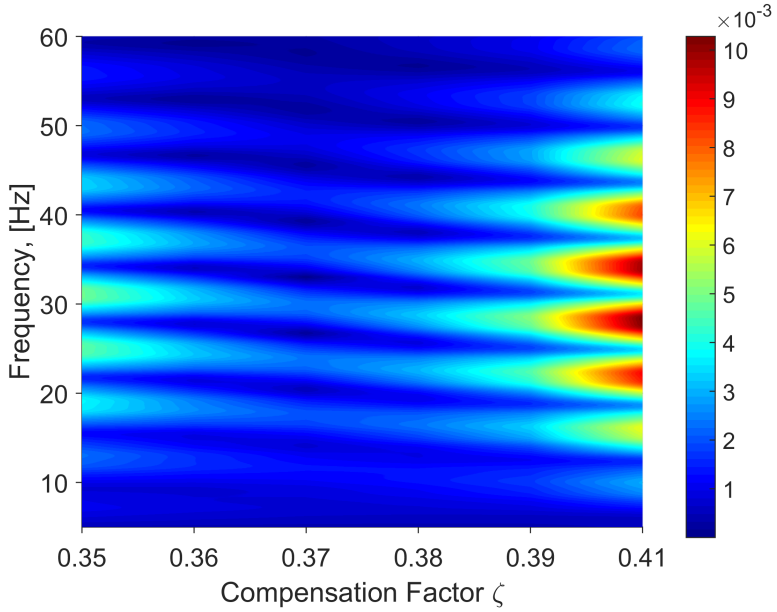

Figure G-4: Function $\widehat{\mathcal{T}}^i_{f1}(\mathbf{x},\omega)$ for Model 3b. The x-axis represents the compensation parameter $\zeta_{compensation} = 0.35,\ 0.36,\ 0.37,\ 0.38,\ 0.39,\ 0.41$. The y-axis represents the frequency. The color denotes the amplitude. The compensation parameter is $\zeta_{compensation} = 0.4$ corresponds to the minimum of $\widehat{\mathcal{T}}^i_{f1}(\mathbf{x},\omega)$. Note Bene: the minimum is not perfect.

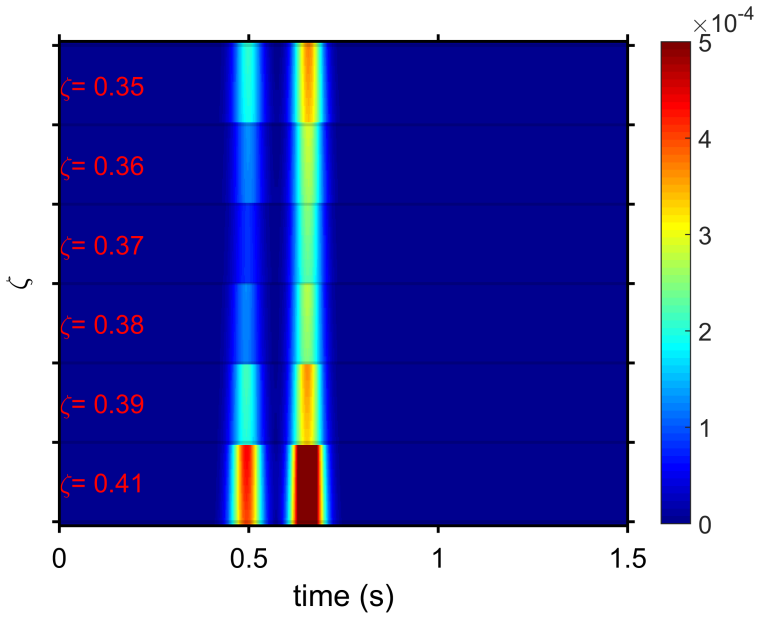

Figure G-5: The continuous 1D wavelet transform of the function $\mathcal{T}^i_{f1}(\mathbf{x},t_l)$ using the Morlet wavelet (Model 3a). The x-axis represents time in seconds. The y-axis represents scale a. The y-axis is divided into 6 horizontal bands. Each horizontal band corresponds to a different $\zeta_{compensation}$. Within each horizontal band, scales $a =$ 70-80 are shown. The color represents the coefficient value. Note Bene: the second artefact is still present for any compensation parameter.